Fundamental Study of Transport Phenomena by Electrochemical Method(Dissertation_全文)

AUTHOR(S):

Ueda, Hiromasa

FUNDAMENTAL STUDY

OF

TRANSPORT PHENOMENA BY ELECTROCHEMICAL METHOD

HIROMASA UEDA

November 1970

FUNDAMENTAL STUDY

OF

TRANSPORT PHENOMENA BY ELECTROCHEMICAL METHOD

HIROMASA UEDA

November 1970

CONTENTS

PART I TRANSPORT PHENOMENA IN THE ENTRANCE REGION OF A CIRCULAR TUBE

CHAPTER 1 INTRODUCTION 1

1- 1 Previous work 4

1-1-1 Momentum transfer 4

1-1-2 Heat and mass transfer 7

1- 2 Purpose and outline 8

1- 3 Outline of the electrochemical method 10

CHAPTER 2 MOMENTUM TRANSFER IN THE BOUNDARY LAYER 13

2- 1 Time-smoothed velocity distribution 13

2-1-1 Purpose 13

2-1-2 Experimental apparatus and procedure 15

a) Water tunnel 15

b) Test section 17

c) Velocity measuring probe 19

2-1-3 Preliminary measurements 20

2-1-4 Time-smoothed velocity profile 20

2-1-5 Effect of pressure gradient on the time-smoothed velocity distribution 29

2-1-6 Velocity-defect layer 34

2-1-7 Concluding remarks 38

2- 2 Fluctuating velocity 42

2-2-1 Purpose 42

2-2-2 Method in the measurement of the fluctuating velocity 43

2-2-3 Experimental apparatus and procedure 48

2-2-4 Distribution of turbulence intensity 50

2-2-5 Power spectrum density of u' 52

2-2-6 Concluding remarks 55

Appendix 2-1 Electrochemical kinetics 56

Appendix 2-2 Principle in the measurement of the fluctuating velocity 60

Appendix 2-3 Response of the probe output signal to fluctuations in the stream velocity 65

CHAPTER 3 DEVELOPMENT OF THE BOUNDARY LAYER

3- 1 Purpose 81

3- 2 Theoretical prediction: method I (with one-parameter velocity profile) 82

3-2-1 One-parameter velocity profile 82

3-2-2 Basic equations 85

3- 3 Theoretical prediction: method II
(with two-parameter velocity profile) 87

3-3-1 Two-parameter velocity profile 87

3-3-2 Entrainment function 88

3-3-3 Basic equations 89

3- 4 Boundary layer thickness 93

3- 5 Skin friction 101

3-5-1 Principle, method and equipment in the measurement of the skin friction 102

3-5-2 Preliminary experiment 107

3-5-3 Distribution of the local skin friction factor 109

3-6 Concluding remarks 113

CHAPTER 4 MASS TRANSFER 116

4- 1 Purpose 116

4- 2 Theoretical prediction 118

4-2-1 Differential equation 118

4-2-2 Solution 123

4- 3 Experimental apparatus and procedure 129

4- 4 Experimental results and discussion 134

4-4-1 Local mass transfer coefficient 134

4-4-2 Space-averaged mass transfer coefficient 140

4-4-3 Comparison with previous work 145

4-5 Concluding remarks 147

Appendix 4-1 Numerical calculation 148

Appendix 4-2 Validity of equation (4-25) 151

PART II TRANSPORT PHENOMENA AROUND A CIRCULAR CYLINDER IN CROSS FLOW

CHAPTER 5 EFFECT OF FREE-STREAM TURBULENCE ON MASS TRANSFER FROM A CIRCULAR CYLINDER IN CROSS FLOW

5- 1 Introduction 154

5-1-1 Previous work 155

5-1-2 Purpose and outline 157

5- 2 Experimental apparatus and procedure 159

5- 3 Space-averaged mass transfer coefficient 162

5- 4 Local mass transfer coefficient 166

5-4-1 Local mass transfer coefficient for zero

turbulence intensity 166

5-4-2 Distributions of static pressure, $U_G(x)/U_\infty$ and local skin friction factor 170

5-4-3 Distribution of local mass transfer coefficient for zero turbulence intensity 177

5-4-4 Measured distribution of local mass transfer coefficient 179

5- 5 Location of the separation point 184

5- 6 Concluding remarks 186

CHAPTER 6 CONCLUSIONS AND RECOMMENDATIONS FOR FUTURE WORK

6- 1 Conclusions 188

6-1-1 Transport phenomena in the entrance region of a circular tube 188

a) Momentum transfer in the boundary layer 188

b) Development of the boundary layer 189

c) Mass transfer 191

6-1-2 Transport phenomena around a circular cylinder in cross flow 192

6- 2 Recommendations for future work 193

6-2-1 Transport phenomena in the entrance region of a circular tube 193

6-2-2 Transport phenomena around a circular cylinder in cross flow 194

NOMENCLATURE 196

REFERENCES 201

PART I

TRANSPORT PHENOMENA

IN THE ENTRANCE REGION OF A CIRCULAR TUBE

CHAPTER 1

INTRODUCTION

The flow in the entrance region of a circular tube is a transition from a boundary layer flow at the entrance to a fully developed turbulent flow far downstream.

It is assumed that the fluid enters the tube with an uniform velocity distribution. Through the action of wall friction , a boundary layer is created at the wall which gradually encroaches on the uniform stream as the flow proceeds down the tube. As the total flux remains constant, the flow in the undisturbed core (free stream) must accelerate to compensate for this retardation of the flow near the wall. This acceleration of the free stream velocity causes a negative pressure gradient in the direction of flow which, in turn, deforms the velocity

profile in the boundary layer. When the boundary layer thickness reaches a value equal to the tube radius, the free stream in the undisturbed core and so the boundary layer type flow disappears. Following the disappearance of the free stream, further changes in the velocity profile occur before a fully developed condition is reached. Fig. 1.1 illustrates the growth of the boundary layer and several of its important characteristics.

Below the critical Reynolds number where the flow in the fully developed region is laminar, the boundary layer is laminar throughout the entrance region. Beyond the critical Reynolds number, the boundary layer is laminar up to the transition point and then becomes turbulent.

From a practical point of view the problems of momentum, heat and mass transfer in the entrance region of tubes have been subjects of considerable importance for the design of hydraulic pipe systems, heat exchangers and tubular reactors. From a theoretical point of view, the main interest is concentrated in the interaction between the boundary layer growth and the velocity profile in the boundary layer.

This work is a contribution to the study of this phenom-

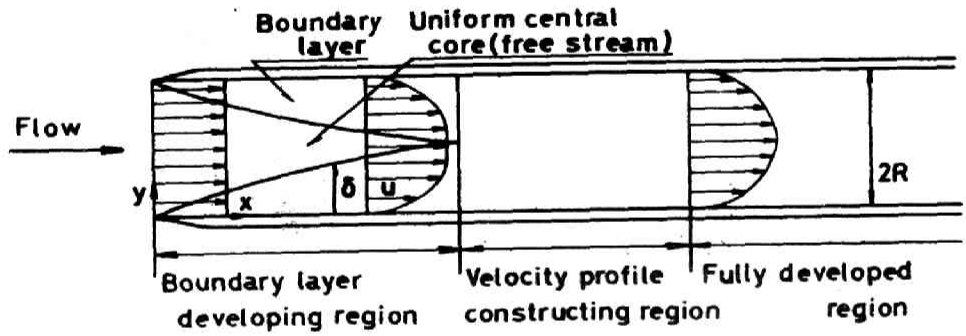

Fig.(1-1) Growth of turbulent boundary layer in the entrance region of a circular tube.

ena, i.e., the momentum, heat and mass transfer in the entrance region of a circular tube. This study is limited to transport phenomena in the turbulent boundary layer which exists in the entrance region.

1-1 Previous work

1-1-1 Momentum transfer

Although laminar flow in the entrance region of a circular tube has been investigated thoroughly, there have been few investigations of turbulent boundary layers in the entrance region. The first experimental study was made by Kirsten(55) in 1927. Kirsten found that the fully developed velocity profile is achieved after an inlet length of 50 to 100 diameters. Later on, Nikuradse(52) found its length to be about 25 to 40 diameters.

An approximate analysis of the development of the turbulent boundary layer in the entrance region was first made by Latzko(33) based on an assumed 1/7-power velocity distribution law and the Blasius resistance formula. A similar analysis was later presented by Glanert(15) and Leont'ev(32). In the

analysis made by Ross(55), he used the kinetic energy equation as well as the continuity and momentum equations. Integration of these equations requires an analytical expression for the skin friction factor. He used the expression suggested by Nikuradse(52) for fully developed tube flow. Szablewski(73) made use of a logarithmic velocity profile for a flat plate boundary layer. Later on, Deissler(7, 8) assumed that the distribution of the eddy diffusivity of momentum for fully developed tube flow may also be applied to a developing boundary layer. With this eddy diffusivity distribution, he determined the velocity profile in the boundary layer and then used the momentum equation to predict the development of the boundary layer.

All of the above prediction methods are based on data obtained for fully developed tube flow or fully developed boundary layer flow with zero pressure gradient, but not for turbulent boundary layer flow with non-zero pressure gradients. As mentioned earlier, the flow in the entrance region is a turbulent boundary layer with negative pressure gradients. In order to predict the development of the boundary layer more accurately, a more detailed examination of the velocity distribution within the boundary layer in the entrance region is necessary. This has not been done until now.

Recently, systematic investigations of the velocity profile in the turbulent boundary layer with pressure gradients have been made by Clauser(4, 5), Townsend(76, 77), Stratford (70, 71), Mellor(40,41) and McDonald(38). Clauser, Townsend and Stratford showed experimentally that the eddy diffusivity of momentum does not depend explicitly on the pressure gradient and remains constant throughout the outer portion of the boundary layer, i.e., in the velocity-defect layer. Townsend and Mellor predicted the effect of pressure gradient on the velocity field in the velocity-defect layer.

In the inner portion of the boundary layer the eddy diffusivity may be reasonably assumed to be independent on the pressure gradient. Mellor and McDonald used this assumption to predict the effect of the pressure gradient on the velocity profile. From a detailed and thorough examination of the velocity profiles in the flow with and without pressure gradients, Coles put forth the so-called "Law of the Wake" and presented an empirical formula for the velocity profile which is valid both in the wall region and the velocity-defect region.

1-1-2 Heat and mass transfer

Experimental study was first carried out by Stanton(68). Later on, Nusselt(50), Humble(27) and Aladyev(2) investigated experimentally the effect of the entrance condition on the heat transfer coefficient and presented an empirical formulae to correct for that effect. Their works were limited to heat transfer at moderate Prandtl numbers, so the applicability of these formulae to the problems of heat and mass transfer at large Prandtl or Schmidt numbers is questionable.

Theoretically, the problems of turbulent heat and mass transfer in the boundary layer have been attacked by two methods. One is the integral method wherein the forms of the velocity and temperature profiles are assumed and the energy integral equation is used to arrive at a relation between the local heat transfer coefficient and the local friction factor. The second is the analogy method proposed by von Kármán(80) wherein the analogy between mechanisms of momentum and heat transfer are assumed and an empirical velocity profile is used to determine the heat transfer rate in terms of the local friction factor.

The theoretical treatment of heat and mass transfer in the entrance region has only been made by Deissler(7, 8).

He assumed that the velocity and temperature profiles in the fully developed tube flow might be applied also to the developing boundary layers in the entrance region. He used the integral method mentioned above and obtained fairly good results at moderate Prandtl numbers. These methods seem to be useful for moderate Prandtl numbers, but their application to heat transfer at large Prandtl numbers is questionable because they do not account adequately for the transport of heat by the eddy motion in the region close to the wall where the temperature gradient exists.

1-2 Purpose and outline

The purpose of the study in Part I is to investigate transport phenomena in the entrance region of a circular tube. The study was started by making precise measurements of the velocity distribution in the turbulent boundary layer at several cross sections in the entrance region. Then theoretical analyses were developed to predict the development of the boundary layer and the rates of heat and mass transfer. Finally, the axial distributions of the boundary layer characteristics, skin friction and mass transfer rate were measured and compared with the pre-

dicted values.

Chapter 2 deals with the velocity distribution in the turbulent boundary layer. At first, the time-smoothed velocity distributions were measured at several cross sections and then the effect of the longitudinal pressure gradient on the velocity distribution was analysed. Finally, two expressions of the velocity profile written in a simple form were recommended for the analyses of the development of the boundary layer. On the other hand, the fluctuating velocity were measured by means of the electrochemical method and the distribution of turbulence intensity and the frequency spectrum density were obtained.

In Chapter 3, methods for the analytical prediction of the development of the boundary layer by use of the recommended velocity profiles were presented. On the other hand, the skin friction were measured directly by means of the electrochemical method. The experimental results of the axial distributions of the skin friction as well as the boundary layer thicknesses and the static pressure were compared with the analytical results.

Chapter 4 deals with mass transfer between the tube wall

and the turbulent stream. The mass transfer at large Schmidt numbers was analysed theoretically by assuming that the distribution of the eddy diffusivity of mass is the same as that for fully developed turbulent flow. Mass transfer measurement were also carried out at a large Schmidt number by means of the electrochemical method and were compared with the predicted results.

In this study measurements were frequently carried out by the electrochemical method, so a brief explanation of that method will be made in the next section.

1-3 Outline of the electrochemical method

In an electrode reaction the ions move from the bulk of the elcrolyte solution to the surface of the electrode where the ions charge or discharge the electrons. The ions are transferred: (a) by migration due to the electric potential field, (b) by diffusion due to the concentration gradient and (c) by convection. When ion transfer is steady and unidirectional in the y direction perpendicular to the electrode surface, the rate of ion transfer may be expressed as

$$N = \left(D+\varepsilon_{\psi} \right) C \frac{n_e}{RT} \frac{\partial \psi}{\partial y} - \left(D+\varepsilon_{D} \right) \frac{\partial C}{\partial y} + vC \qquad (1\text{-}1)$$

and the current density at the electrode is expressed as

$$i / A = n_e F N \qquad (1\text{-}2)$$

The three terms on the right hand side of Eq. (1-1) represent the contributions of migration, diffusion and convection respectively. The last term for convection vanishes in the redox system as used in this work because there is no net flow in the y direction. If one adds a large excess of inert or "supporting"electrolyte, which does not react at the electrode but serves to remove all potential gradients in the vicinity of the electrode surface, then the migration current becomes negligible and almost all of the electrolysis current arises from the reaction of ions which reach the electrode surface by diffusion.

Electron-charge transfer process at the electrode surface is discussed in Appendix 2-1. As the overvoltage at the test electrode increases, the reaction rate constant increases exponentially. At the limiting current condition, the electron-charge transfer occurs so quickly that the concentration of

the reacting ions at the electrode surface becomes substantially zero and the diffusion process of the discharging ions results in an ordinary convective mass transfer with constant wall concentration. The relation between the electric potential and the current is shown in Fig. 2-20.

In this work the redox reaction of a ferri- and ferrocyanide system is used, that is,

$$Fe\,(CN)_6^{-3} + e^- \longrightarrow Fe\,(CN)_6^{-4} \qquad \text{at cathode (test electrode)}$$

$$Fe\,(CN)_6^{-4} \longrightarrow Fe\,(CN)_6^{-3} + e^- \qquad \text{at anode}$$

This reaction is superior to other reactions for the following reasons:

(1) The rate constant of the electron-charge transfer is very large.

(2) There is no side reaction provided that the system is free from dissolved oxygen and light.

(3) The condition of the electrode surface does not change because deposition does not occur during the electrolysis.

(4) The bulk concentration of reacting ions remains constant during the electrolysis.

CHAPTER 2

MOMENTUM TRANSFER IN THE BOUNDARY LAYER

2-1 Time-smoothed velocity distribution

2-1-1 Purpose

The flow in the entrance region of a circular tube is a boundary layer flow. It would be expected that this flow would resemble a boundary layer flow over a flat plate, but there is actually a significant difference between the behavior of the free stream in the two cases. Unlike that encountered in the boundary layer over a flat plate, the free stream in the entrance region is completely surrounded by a growing boundary layer. As the displacement thickness of the boundary layer grows, the free stream accelerates, thereby causing a negative pressure gradient in the flow direction. Therefore, the main characteristic of this type of flow is a turbulent boundary layer with negative pressure gradients.

Although time-smoothed velocity profile in the entrance region of a circular tube have been presented by a few investigators(52,56), but they were unable to obtain reliable data on the skin friction. For that reason, they could not make detailed examinations of the velocity profile in the turbulent boundary layer with non-zero pressure gradients which exists in the entrance region, and so they could not find out the effect of the pressure gradient on the velocity profile. In calculations of the development of the boundary layer in the entrance region, the previous workers(7,15,32,33,55,73) assumed that the velocity profile in the boundary layer was the same as that over a flat plate with zero pressure gradient and their analyses predicted rapid growthes of the boundary layer thickness. This inaccuracy seems to be brought about by insufficient considerations of the velocity profile in the boundary layer.

The purposes of the work covered in this section are:

1: To measure the time-smoothed velocity distributions in the entrance region.

2: To clarify the difference between the velocity distribution in the entrance region and that in the fully developed turbulent boundary layer on a flat plate.

3: To estimate the effect of the longitudinal pressure gradient on the velocity profile.

4: To recommend an expression of the velocity profile in a simple form for the analyses of the development of the boundary layer and of heat and mass transfer.

2-1-2 Experimental apparatus and procedure

a) Water tunnel

The flow system in the experimental apparatus is shown in Fig. 2-1. The design of the tunnel was similar to Hori type water tunnel(25) except that special precautions were taken in order to avoid contamination of the circulating fluid for experiments in which the electrochemical method was used. The only materials in contact with the fluid were nickel, stainless steel and polyvinylchloride. Special care was taken to achieve a flat velocity profile and a small turbulence level at the tube entrance and to eliminate swirling motion of the flow. A convergent nozzle with a contraction ratio of 10:1, three 48-mesh screens and a honeycomb were used for this purpose. The honeycomb consisted of a number of glass tubes, 15cm long and 1cm in diameter, was installed in the calming section. In addition, the flow close to the wall of the convergent nozzle exit was cut off to the

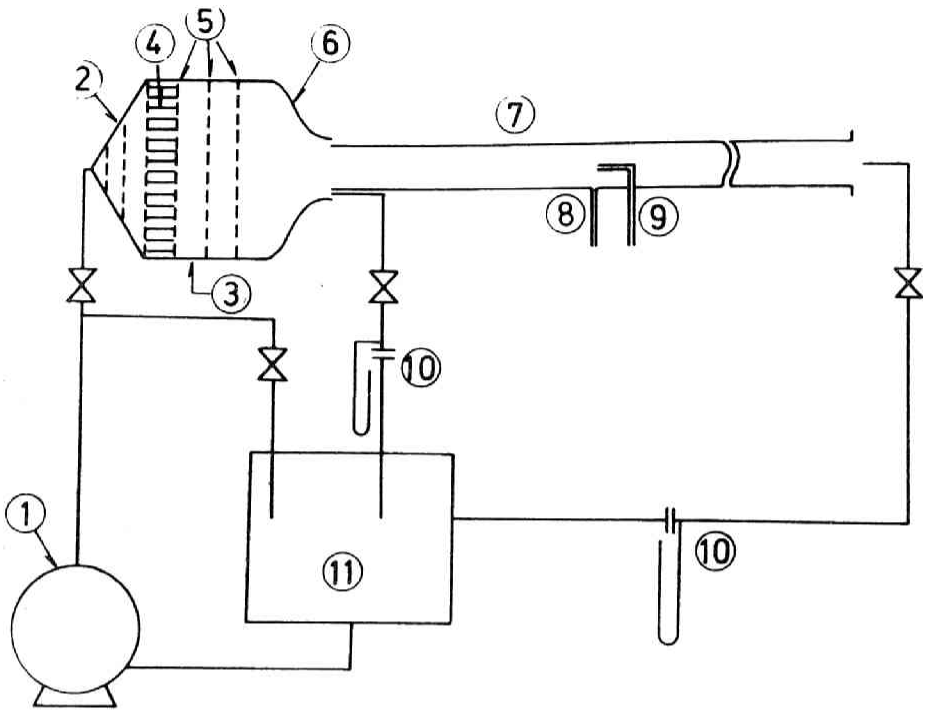

1	Pump	7	Test section
2	Divergent nozzle		(2 inch I.D. PVC tube)
3	Calming section	8	Static pressure tap
4	Honeycomb	9	Total pressure tube
5	Screen	10	Orifice meter
6	Convergent nozzle	11	Storage tank

Fig.(2-1) Flow system.

by-pass as shown in Fig. 2-2. Since the opening angle of the divergent nozzle tends to cause a large swirling motion and since this motion does not disappear in the water tunnel, two 48-mesh screens with a honeycomb between them were installed in the tube preceeding the water tunnel.

A centrifugal pump made of polyvinylchloride was used to circulate the fluid. The temperature of the fluid was maintained at 30±0.05 deg. C by a controller and a cooling coil immersed in the reservoir tank.

b) Test section

A schematic diagram of the entrance to the test section and the location of the co-ordinate axes are shown in Fig. 2-2. The test section was made of polyvinylchloride tube of 52.5 mm I.D. with a sharp leading edge. In this experiment two kinds of leading edges, with and without a trip wire were used. If there is no trip wire, a laminar boundary layer develops at first, followed by a turbulent boundary layer. On the other hand, if there is a trip wire, a turbulent boundary layer develops from the leading edge provided that the Reynolds number is greater

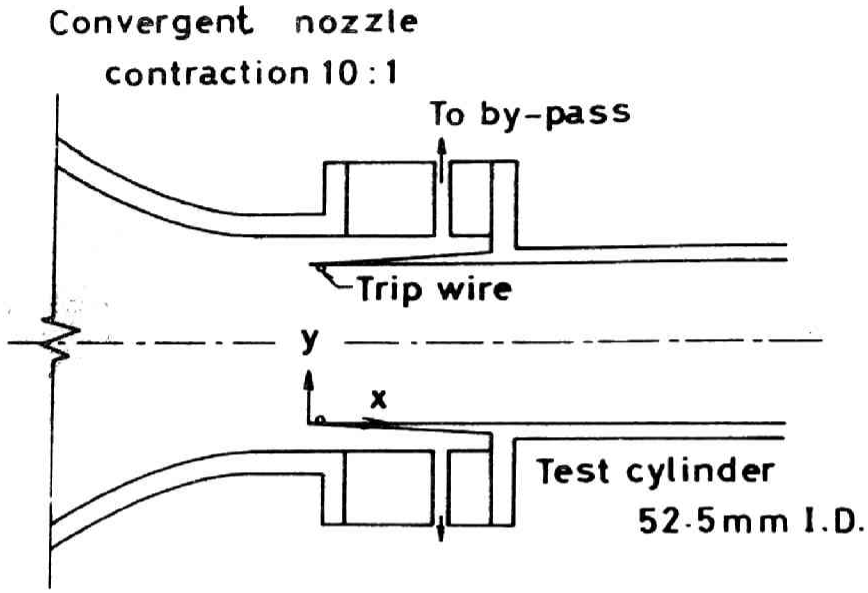

Fig.(2-2) Tube entrance and co-ordinate axes.

than 10^4. The trip wire was made of 1 mm diameter nickel wire attached to the wall of the tube 3 mm downstream from the leading edge. For the measurement of the variation of the static pressure in the flow direction, a tube with eight static pressure holes of 0.8 mm in diameter located at approximately x/D=1.5, 8.0, 17.5, 27.0, 36.5, 46.0, 55.6 and 65.0 was used.

c) Velocity measuring probe

For the measurement of the time-smoothed velocity two kinds of total-pressure tube were used. The one was a stainless steel tube of 0.8 mm O.D. and 0.6 mm I.D. The other was a thin-walled tube of the same inside diameter, but flattened at one end to form a nearly rectangular opening of 1.5 mm wide. The total-pressure tubes were calibrated with the standard Prandtl type pitot tube. A 0.6 mm diameter static pressure hole was drilled in the tube wall at the cross section corresponding to the tip of the total-pressure tube.

2-1-3 Preliminary measurements

When the measurements were initially attempted without a honeycomb in the tube proceeding the water tunnel, a uniform velocity distribution was not established at the tube entrance and swirling flow was quite unstable. Addition of the honeycomb upstream of the divergent nozzle made the flow stable and produced a flat velocity profile as shown in Fig. 2-3. Next, a careful study of the symmetrical nature of the flow in the entrance region was made. Time-smoothed velocity measurements in three cross sections at x/D=6, 9 and 12 from the entrance were carried out by traversing the total-pressure tube along the horizontal and vertical diameters, and it was confirmed that axi-symmetrical flow was established in the entrance region.

2-1-4 Time-smoothed velocity distribution

As seen from Fig. 3-2, a turbulent boundary layer develops from the leading edge if a trip wire is attached, but a laminar boundary layer develops at first, followed by a turbulent boundary layer if there is no trip wire. To restrict the discussion to the turbulent boundary layer, only the experimental results obtained in the case with a trip wire will be shown.

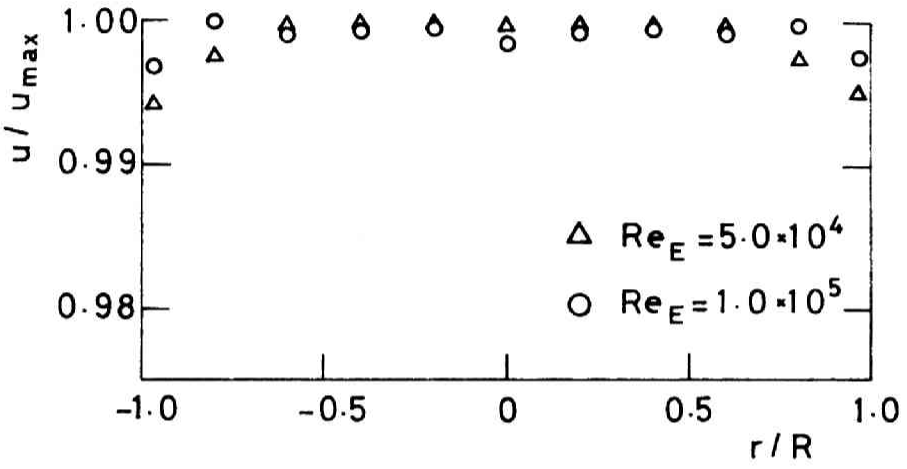

Fig.(2-3) Velocity distribution at the inlet cross section.

The time-smoothed velocity distributions in the cross sections at x/D = 3, 6, 9, 12, 15, 29 and 73 were measured using a total-pressure tube. Figure 2-4 shows the time-smoothed velocity distributions at the Reynolds number of $Re_E = 1 \times 10^5$. In this diagram δ is the boundary layer thickness defined as the y-distance at which $u/U_G = 0.99$.

By use of the local values of the skin friction factor measured directly by the electrochemical method (see in Section 3-6), the velocity distributions are replotted by transforming the coordinates to u^+ vs. y^+, as in Fig. 2-5. In each diagrams, the velocity distributions in any cross sections of the entrance region are correlated by a single curve, which deviates only slightly from the curve for fully developed turbulent flow with zero pressure gradient. This correlation was also confirmed at various other Reynolds numbers, i.e., $Re_E = 2 \times 10^4$, 3.6×10^4 and 5×10^4, as shown in Figs. 2-6, 7. This fact indicates that the similarity exists in the velocity profiles in the entrance region of a circular tube.

These curves for velocity distributions may be represented by the following equation:

$$u^+ = c \left(y^+ \right)^{1/m} \qquad (2\text{-}1)$$

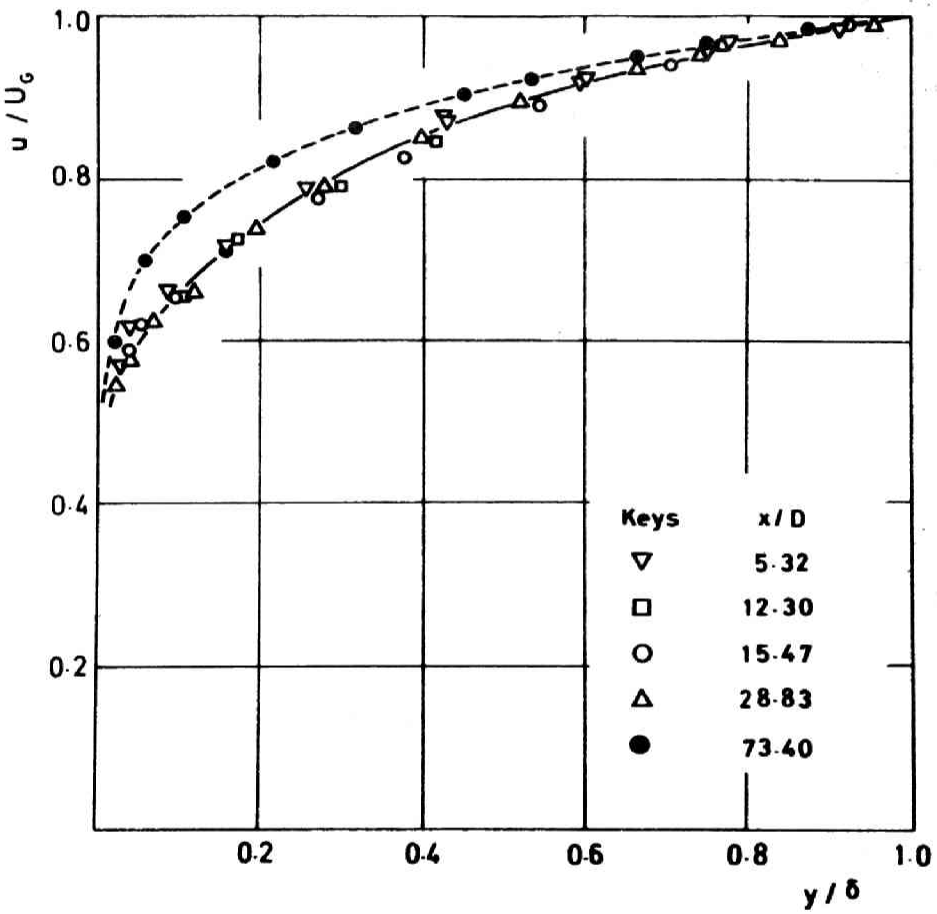

Fig.(2-4) Velocity distribution in the entrance region of a circular tube, $Re_E=1.0\times10^5$.

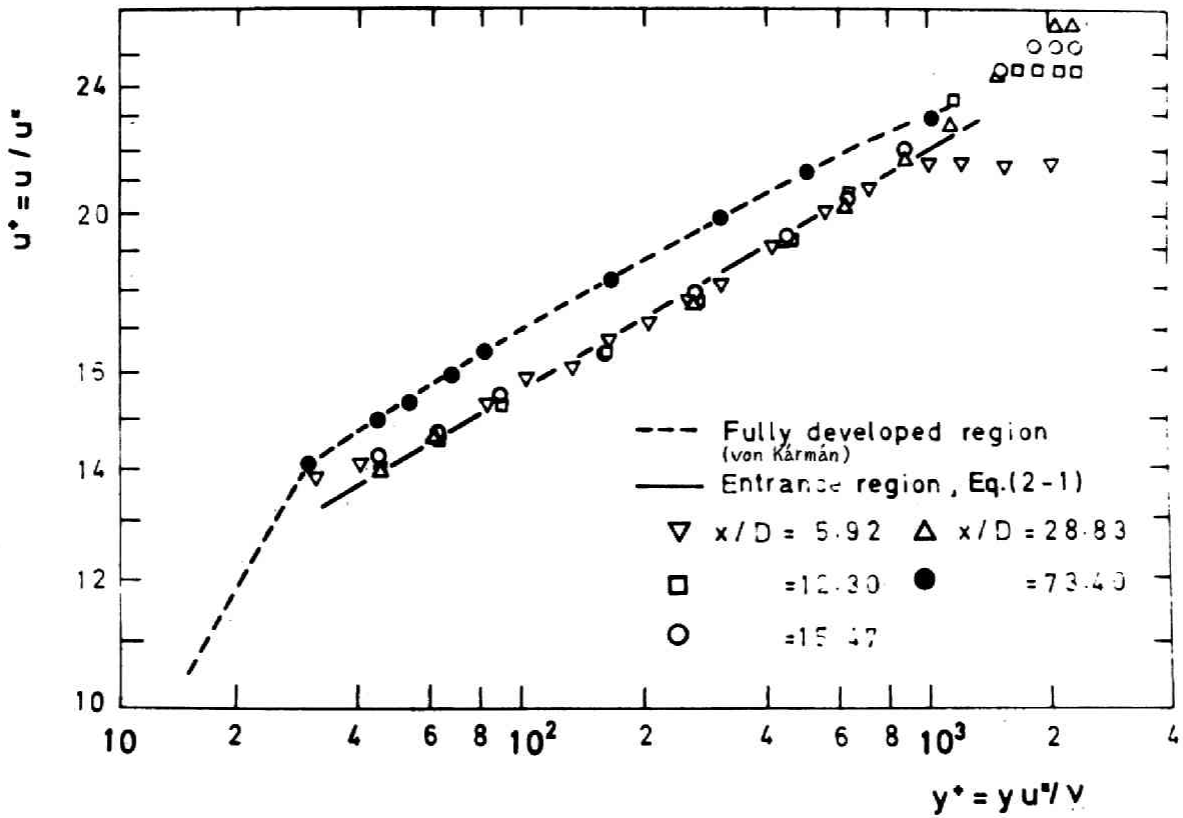

Fig.(2-5) Universal velocity distribution in the entrance region of a circular tube, $Re_E=1.0\times10^5$.

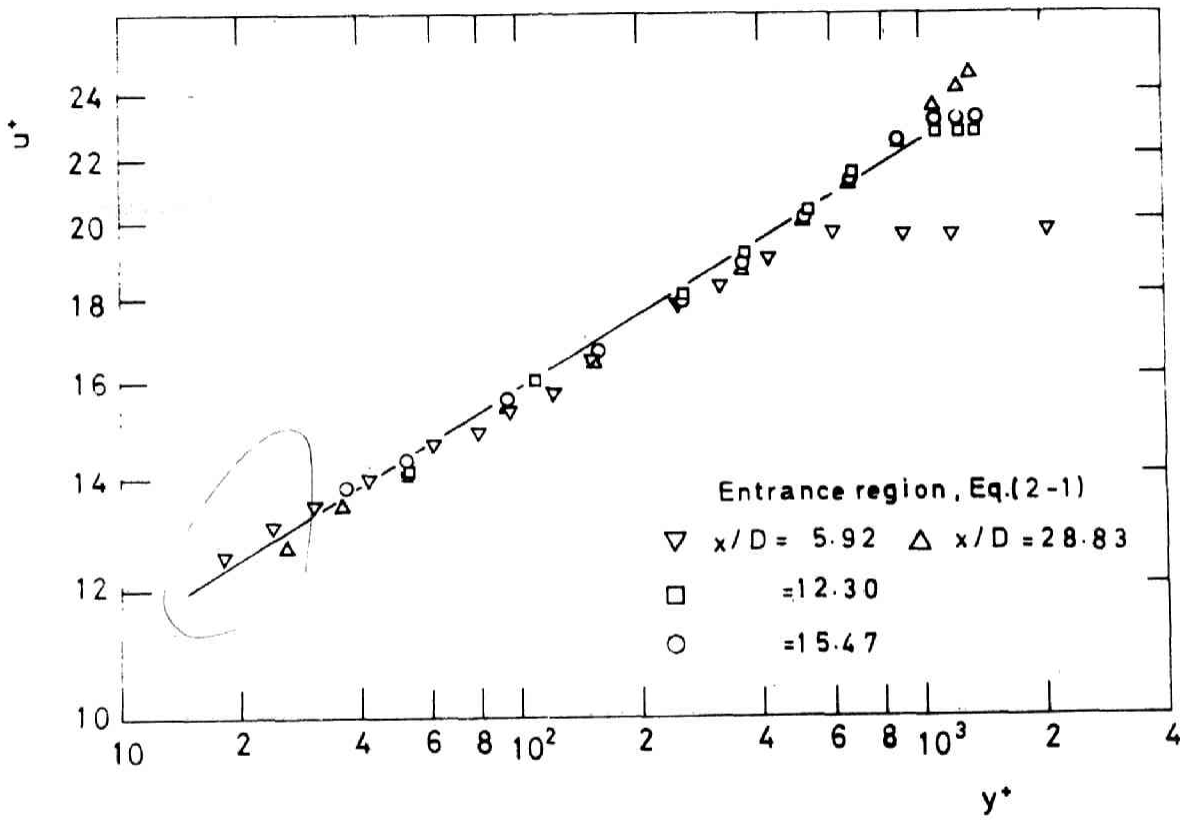

Fig (2-6) Universal velocity distribution in the entrance region of a circular tube, $Re_E=5.0\times10^4$.

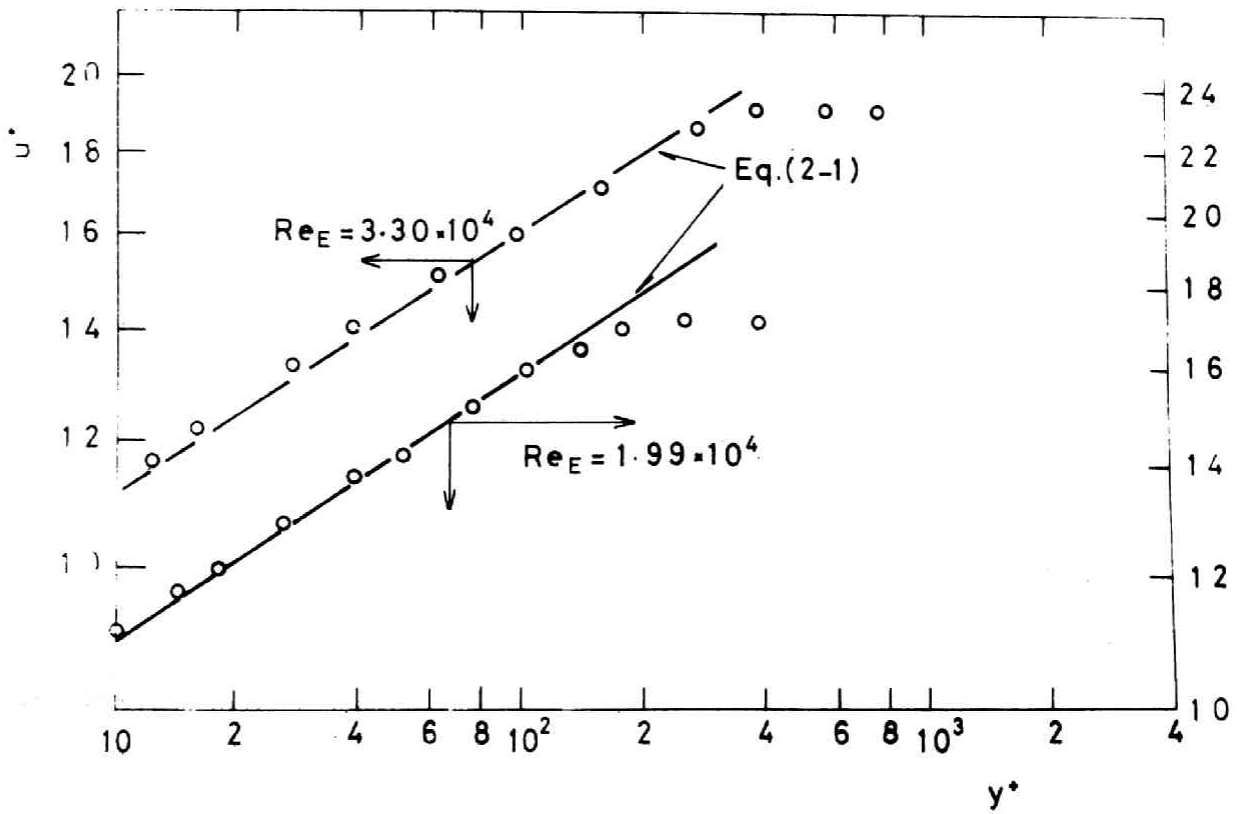

Fig.(2-7) Universal velocity distribution in the entrance region of a circular tube, $Re_E=1.99\times10^4$ and 3.30×10^4.

where m and c are characteristics of the flow and depend only on the Reynolds number based on the inlet velocity and the tube diameter. Nikuradse(52) found that in fully developed turbulent flow the velocity distribution in the turbulent core region shows a straight line in the coordinate of $ln\ u^+$ vs. y^+. He also showed that the velocity distribution is represented by Eq. (2-1) very well. His data for fully developed tube flow shows the dependence of m and c on the Reynolds number as shown in Fig. 2-8. From Figs. 2-5~2-7, m and c for the developing boundary layer in the entrance region are determined. The dependence of m and c on Re_E is shown in Fig. 2-8. Both m and c are a little smaller than those for fully developed turbulent tube flow. The values of m are only slightly dependent on Re_E and the values of c are almost constant. Assuming that the correlation curves of m and c are parallel to those for the fully developed region, the correlations may be represented approximately by the following equations:

$$m = 3.60\ Re_E^{0.0537} \tag{2-2}$$

$$c = 5.99\ Re_E^{0.0241} \tag{2-3}$$

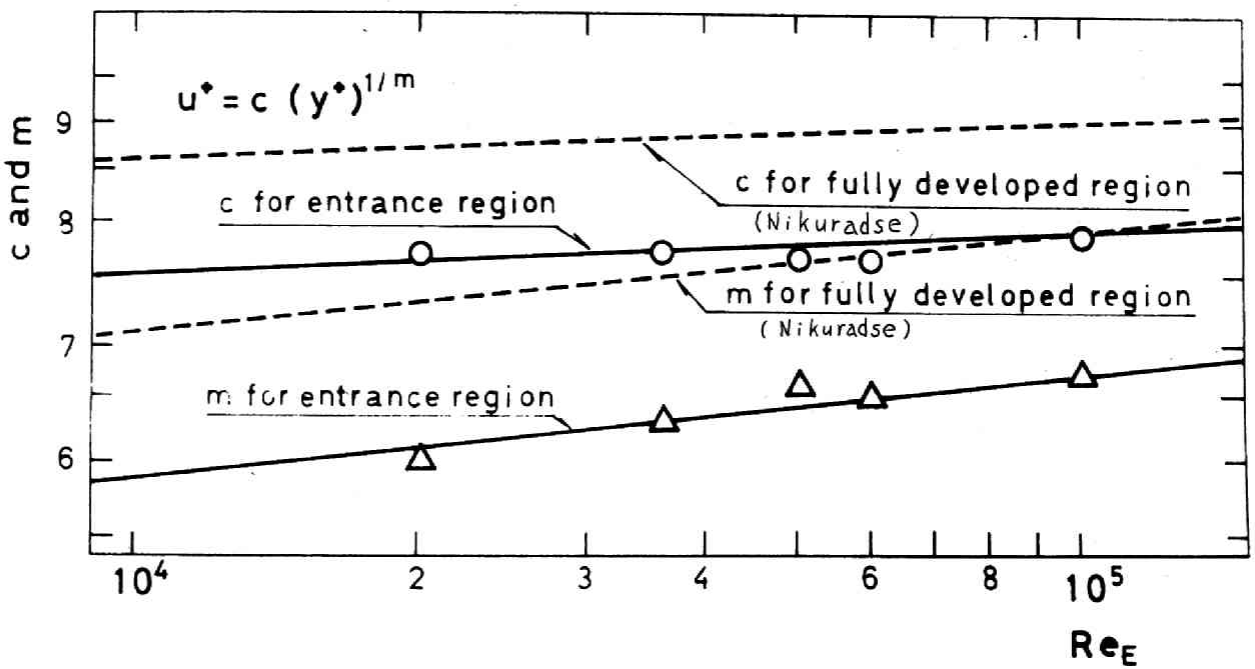

Fig.(2-8) c and m in similarity formula of velocity distribution.

2-1-5 Effect of pressure gradient on the velocity distribution

In the previous section, it was shown experimentally that the measured distribution of the time-smoothed velocity has a similar profile at each of the cross sections in the entrance region and deviates only slightly from that in a turbulent boundary layer with zero pressure gradient. This seems to be due to the effect of longitudinal pressure gradient, which will now examined.

If one introduces the Bousinesq's definition of an "effective viscosity", the shear stress may be described by

$$\tau/\rho = \nu_e \, \partial u/\partial y = (\nu + \nu_t) \, \partial u/\partial y \qquad (2\text{-}4)$$

which includes the molecular shear stress $\nu \, \partial u/\partial y$ as well as the Reynolds stress $-\overline{u'v'}$. Alternatively, $\nu_e = \nu + \nu_t$, where ν_t is the turbulent or eddy viscosity. In the light of the works of Clauser(4, 5), Townsend(75; 76; 77) and Stratford (70) on boundary layer flows with pressure gradients, it seems possible to make a reasonable assumption concerning ν_e which is not explicitly dependent on the pressure gradient.

In the region adjacent to the wall, i.e., in the wall region, the eddy viscosity may be represented by the Prandtl's

mixing-length theory:

$$\nu_t = \frac{\kappa^2 y^2}{\nu} \left| \frac{\partial u}{\partial y} \right| \tag{2-5}$$

where

$$\begin{aligned} (\kappa/\kappa_0) &= 0.00714\ Y + \exp\{3(Y-9)\} \quad \text{for } Y < 9 \\ &= 1 \qquad\qquad\qquad\qquad\qquad\quad Y > 9 \end{aligned} \tag{2-6}$$

and κ_0 is the von Karman constant and $Y=\sqrt{(1/\nu)\partial u/\partial y}\cdot y$. Equation (2-6) is an empirical formula presented by McDonald (38). In the present analysis this equation, as well as $\kappa_0 = 0.41$ is used. On the other hand the shear stress distribution is given by

$$\tau = \tau_w + \frac{dp}{dx} y \tag{2-7}$$

which assumes that the inertia terms in the equation of motion can be neglected in the wall region.

One obtains the velocity distribution by integration of Eq. (2-4), using Eqs. (2-5), (2-6) and (2-7). Simple analytic integration of these expressions is not found possible, so a numerical procedure is adopted. In the outer portion of the

wall region the velocity distribution may be given by Eqs.(2-4), (2-5), (2-6) and (2-7), on neglecting the molecular viscosity contribution, as

$$\frac{\partial u}{\partial y} = \frac{\left(\tau_w + \frac{dp}{dx} y \right)^{1/2}}{\rho^{1/2} \kappa_0 y}$$

which integrates to

$$u^+ = \frac{2}{\kappa} \{(1+\alpha y^+)^{1/2} - 1\} + \frac{1}{\kappa} ln\{\frac{4(1+\alpha y^+)^{1/2} - 1}{\alpha(1+\alpha y^+)^{1/2} + 1}\} + B^+(\alpha) \qquad (2\text{-}8)$$

where the pressure gradient parameter α is defined by

$$\alpha = \frac{\nu}{\rho} \frac{dp}{dx} \frac{1}{u^{*3}} \qquad (2\text{-}9)$$

The resulting equation was presented from the analyses made by Townsend(77), Mellor and Gibson(40) and McDonald(38). $B^+(\alpha)$ is the so-called "slip velocity" and a function of α only. The values of B^+ are determined by comparing Eq.(2-8) with the numerical solution mentioned above.

For small negative values of α, as occured in the entrance region, the values of B^+ were computed and plotted in Fig.(2-9). The velocity profiles predicted by this analysis are shown in Fig.(2-10) with the parameter α. For negative values of α,

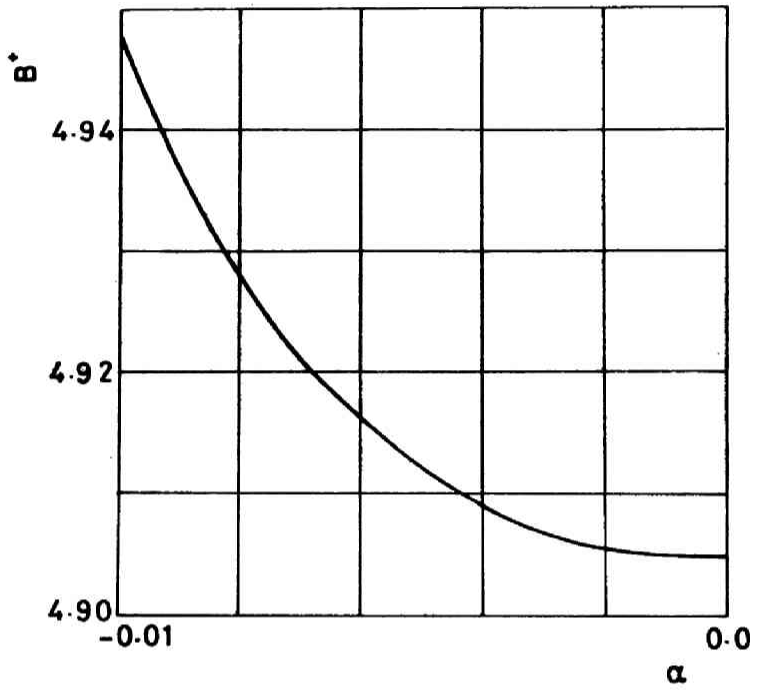

Fig.(2-9) Effect of pressure gradient on the slip velocity B^+.

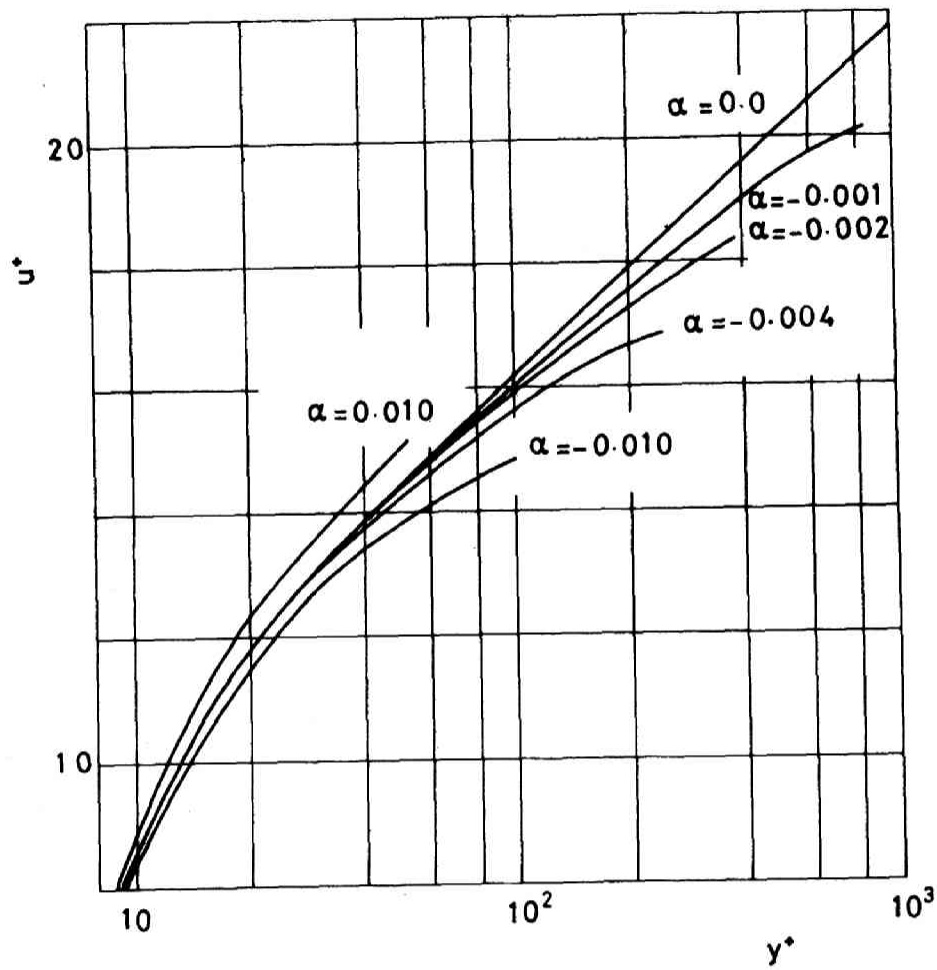

Fig.(2-10) Effect of pressure gradient on the velocity profile near the wall.

the curves of the velocity profiles lie a little below that for the turbulent boundary layer with zero pressure gradient, i.e., $\alpha = 0$.

The experimental results are plotted in Figs.(2-11,12) compared with the analytical one. The agreement is very good and it seems possible to predict the effect of the pressure gradient on the velocity profile by means of this analysis. As will be seen in Section 3-4 and 3-5, dp/dx and τ_w become constant at $x/D \simeq 15$, so that α becomes constant at that point. Therefore this analysis suggests that the velocity profiles at any cross sections downstream from $x/D \simeq 15$ should be perfectly similar.

2-1-6 Velocity-defect layer

From a detailed and thorough examination of the various velocity profiles, Coles(84) put forth the so-called "Law of the Wake". He assumed that the development of a turbulent boundary layer can be interpreted fundamentally in terms of an equivalent wake profile which is characterized by the profile at the point of separation or re-attachment and which is the restraining effect of inertia. This equivalent wake profile

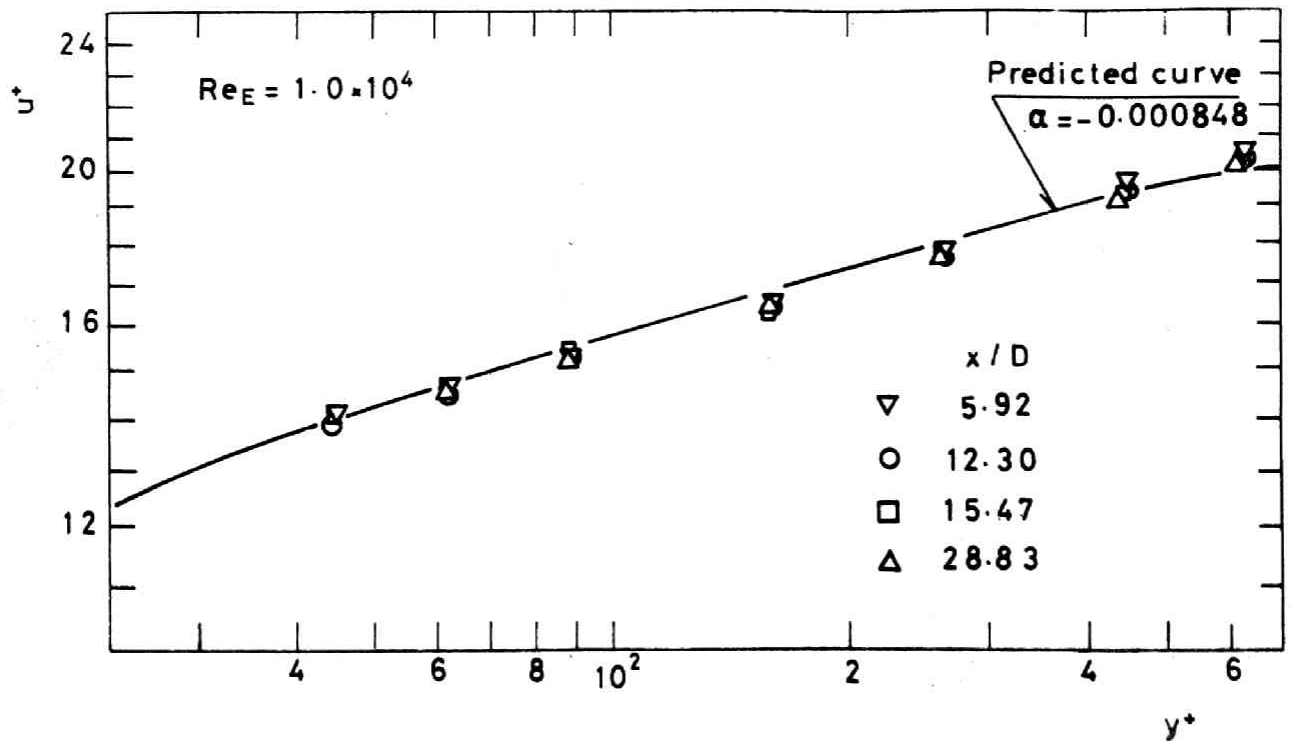

Fig.(2-11) Comparison of experimental u^+ with present analysis, $Re_E = 1.0 \times 10^5$.

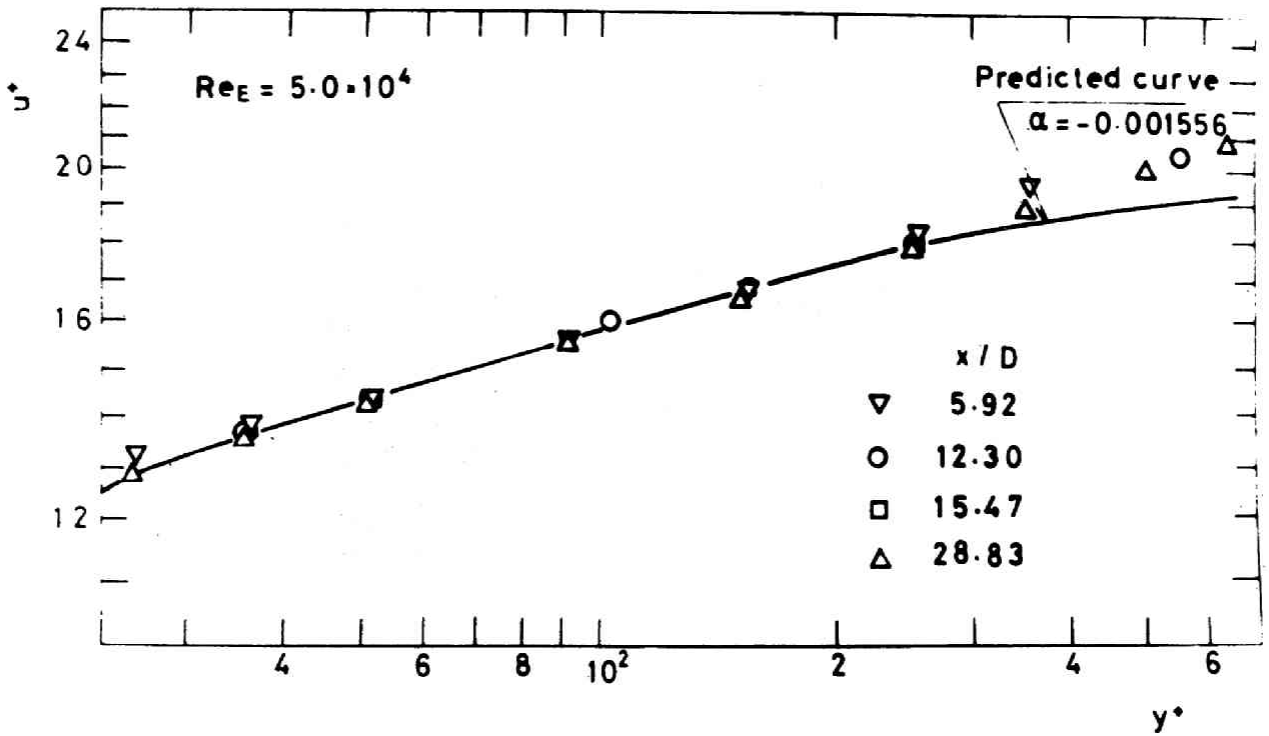

Fig.(2-12) Comparison of experimental u^+ with present analysis, $Re_E=5.0\times10^4$.

is modified by the presence of the wall, at which a further restraint is provided by viscosity. This restraint at the wall , although it penetrates the entire boundary layer, is manifested chiefly in the wall region. Coles presented the following empirical formula for the velocity profile:

$$u^+ = f(y^+) + \P\, \omega(y/\delta) \qquad (2\text{-}10)$$

where $\omega(y/\delta)$ is a universal function known as the "Wake Function" and written by

$$\omega(y/\delta) = (1 - \cos(\pi y/\delta))/2$$

and $\P$ is a profile parameter. Coles showed this formula available to the flow with and without pressure gradients. In the region near the wall $\omega(y/\delta)$ becomes zero and Eq.(2-10) reduces into the ordinary law of the wall:

$$u^+ = f(y^+)$$

With the empirical velocity profile of Eq.(2-1) for $f(y^+)$ and with the boundary condition, i.e., $u=U_G$ at $y=\delta$, one obtains the profile parameter $\P$. Equation (2-10) may be rewritten as

$$u/U_G = Z_E\,(y/\delta)^{1/m} + (1-Z_E)\,\{1-\cos(\pi y/\delta)\}/2 \qquad (2\text{-}11)$$

where

$$Z_E = c\,Re_G^{1/m}\,(c_f/2)^{(1+m)/2m} \quad , \quad Re_G = U_G\delta/\nu \ .$$

Equation (2-11) is compared with the experimental velocity profile in Figs.(2-13, 14). The agreement of these results is fairly good and confirms that Eq.(2-11) may represent the velocity profile in the whole region of the boundary layer. Although this equation may represent the actual velocity profile very well, this equation is a two-parameter velocity profile. In other word, this equation gives the value of the flow velocity when both the skin friction factor and the Reynolds number are given.

2-1-7 Concluding remarks

The following conclusions were obtained from an investigation of the time-smoothed velocity distribution in the entrance region of a circular tube.

1: A similarity in the time-smoothed velocity distribution exists at any cross section in the entrance region. The velocity distribution may be represented by

$$u^+ = c\,(y^+)^{1/m}$$

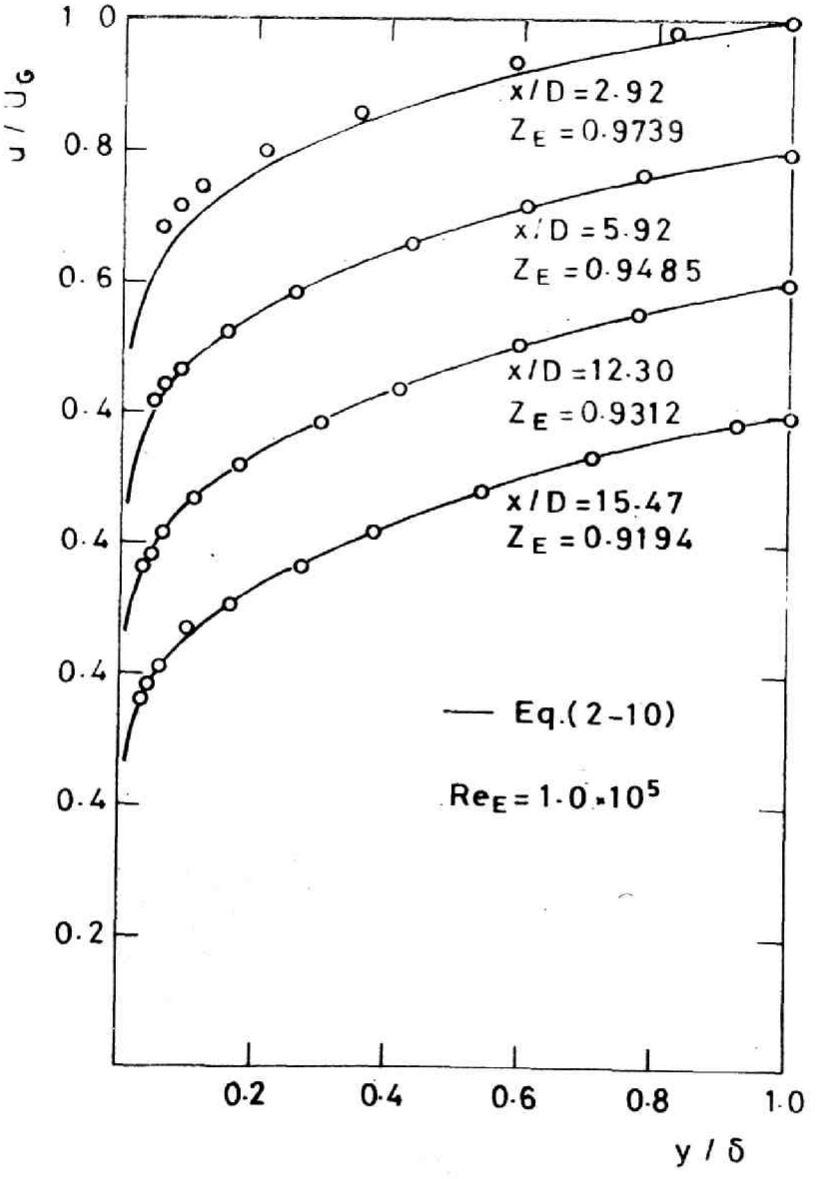

Fig.(2-13) Velocity distribution in the velocity-defect layer, $Re_E=1.0\times10^5$.

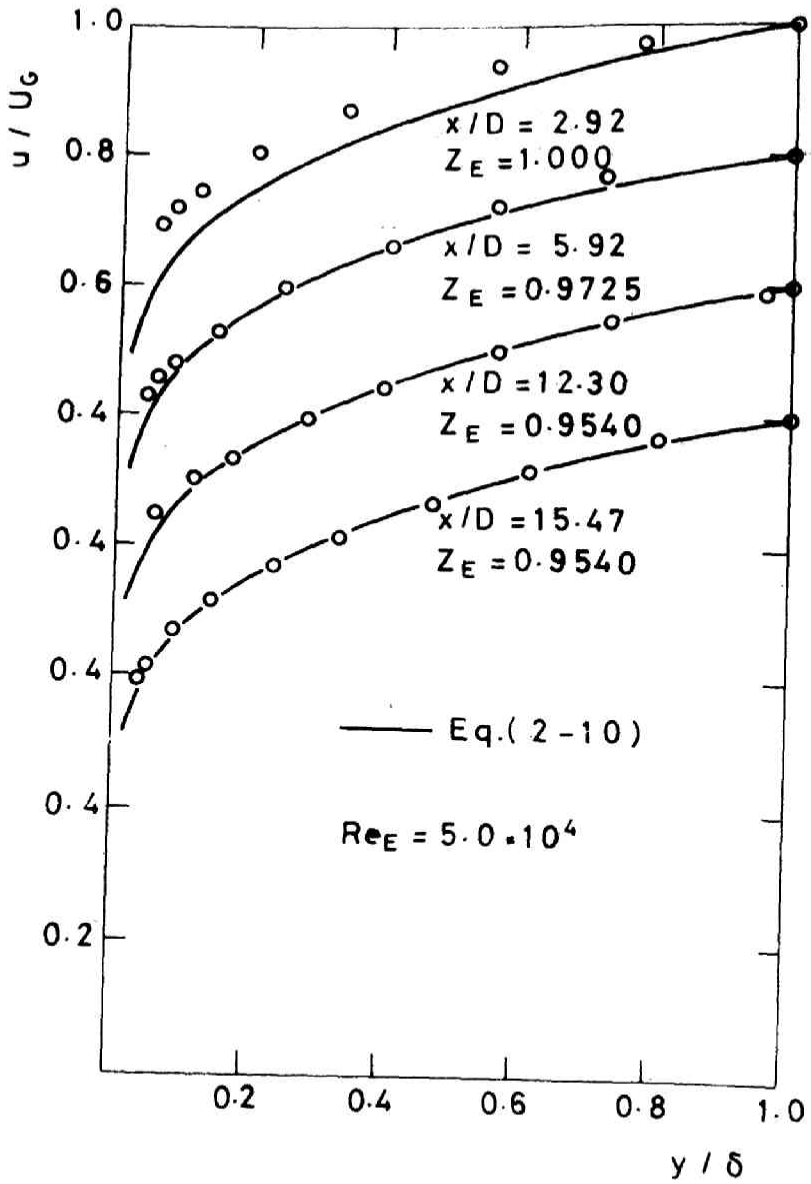

Fig.(2-14) Velocity distribution in the velocity-defect layer, $Re_E=5.0\times10^4$.

The coefficient c and the exponent m depend only slight on the Reynolds number Re_E and are given by

$$c = 3.60\ Re_E^{0.0537}$$
$$m = 5.99\ Re_E^{0.0241} \qquad \text{for } 10^4 < Re_E < 10^5$$

These values of m and c are slightly less than those for fully developed turbulent flow, so the velocity distribution in the entrance region deviates slightly from that in the fully developed region.

2: This deviation of the velocity distribution is caused by the influence of pressure gradient in the flow direction, and may be predicted by a theory based on Prandtl's mixing length hypothesis and the assumption of linear shear stress distribution. This theory also predicts the existence of a similarity in the velocity distribution in the entrance.

3: Coles' "Law of the Wake" is valuable for representing the velocity distribution in the whole of the boundary layer and gives:

$$u/U_G = Z_E\ (y/\delta)^{1/m} + (1-Z_E)\ \{1-\cos(\pi y/\delta)\}\ /2$$

where $Z_E = c\ Re_G^{1/m}\ (c_f/2)^{(1+m)/2m}$.

2-2 Fluctuating velocity

2-2-1 Purpose

In the previous section, it was found that the time-smoothed velocity distributions at any cross sections in the entrance region have a similar profile and that under the influence of longitudinal pressure gradients this profile differs slightly from that of a boundary layer over a flat plate. It would be expected that the longitudinal pressure gradient also affects the mechanism of turbulence and the distributions of the fluctuating properties in the boundary layer. Examination of these effects offers us, in turn, an understanding of the time-smoothed velocity field.

The purposes of this work covered in this section are:

1: To measure the distributions of the turbulence intensity at various cross sections in the entrance region.

2: To measure the power spectrum densities of the fluctuating velocity at various distances from the tube wall.

3: To examine the difference between these results and those for the boundary layer with zero pressure gradient.

Since there have been no convenient and reliable technique for measuring the fluctuating velocity in the liquid flow, an

electrochemical technique was developed and used in these experiments.

2-2-2 Method in the measurement of the fluctuating velocity

In measuring the fluctuating velocity in a gas flow, a hot wire anemometer is generally used. However, convenient and reliable techniques have not yet been developed for liquid flows. Because of the thermal inertia of the hot wire, the hot wire anemometer needs compensation for phase shift and amplitude, and its mechanical strength and operating temperature are limited. Furthermore, the wire length is important because a short wire gives a larger error due to the cooling effect of the supports.

A diffusion-controlled electrochemical process on an extremely small cathode which was used as velocity measuring probe was found to be suitable for this purpose. The electrochemical reaction used was the reduction of ferri-cyanide ion on a platinum cathode in the presence of a large excess of potassium hydroxide.

For the measuring probe, a blunt-nose type and a hot-wire type probes were made as shown in Fig.(2-15). The blunt-nose

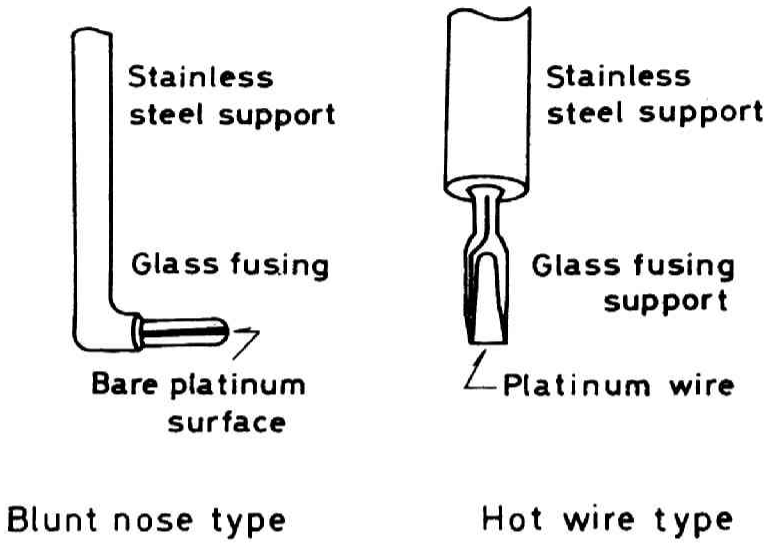

Fig.(2-15) Velocity measuring probes.

type probe has a 0.01 cm diameter platinum wire cathode embedded in the blunt glass nose and smoothed flush with nose surface so that only the tip of the wire is exposed. This type of probe has two appreciable advantages. Hardly any dirt particles cling to the probe during an experiment and the output signal is most reliable. Secondly, the output signal is hardly affected by the angle θ between the flow direction and the axis of the measuring probe provided that $\theta < \pi/6$. The hot-wire type probe has a glass-coated platinum wire cathode, 0.003 cm in diameter by 0.15 cm long at the tips of the prongs. In the experiment, the blunt-nose type probe was used.

The limiting currents of these very small electrodes are related to the liquid velocity and are generally expressed by

$$i = \alpha + \beta u^{0.5} \qquad (2\text{-}12)$$

where α is the natural convection term and $\beta u^{0.5}$ is the forced convection term. For practical use, α and β are determined by experimental calibration. A typical calibration curve of u vs. i is shown in Fig.(2-16).

Since u and i may be written as the sum of the time-smoothed value and the fluctuating one, the Taylor expansion

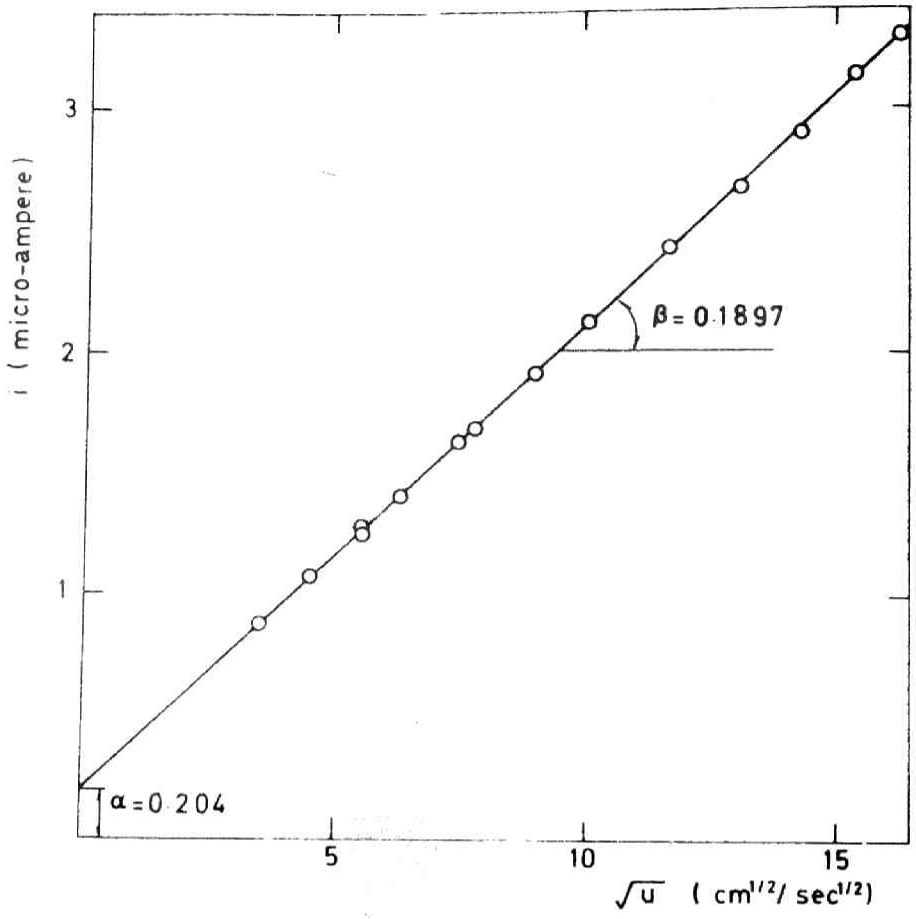

Fig.(2-16) Typical calibration curve for velocity-measuring probe.

of Eq.(2-12) gives the root mean square of the fluctuating velocity as

$$\left(\overline{u'^2}\right)^{1/2} / \bar{u} = 2 \left(\overline{i'^2}\right)^{1/2} / (\bar{u})^{1/2}\, \beta \qquad (2\text{-}13)$$

The derivation of this equation is presented in Appendix 2-2. As seen in Eq.(2-13), β is a very important value, so a more detailed discussion is presented in Appendix 2-2.

For the hot wire anemometer, compensation for phase shift and amplitude attenuation of the fluctuating signal due to the thermal inertia or heat capacity of the hot wire is a serious problem. In the electrochemical method, this compensation is not necessary because there is no capacity for the transferred quantity. However, since this method is based on the transfer of ions, it would be expected that at large Schmidt numbers a capacitance effect of the concentration boundary layer limits the frequency range of the velocity fluctuation that can be detected. The response of a blunt-nose type electrode and a hot wire anemometer to velocity fluctuation was discussed in Appendix 2-3. The amplitude attenuation estimated for Pr=0.7 and 2431 are shown in Fig.(2-23). It is seen that the amplitude ratio decreases more rapidly at higher Prandtl numbers and so the response of mass transfer to velocity fluctuation in liquid flow is not so good as the response of heat transfer in

air flow.

2-2-3 Experimental apparatus and procedure

The experimental apparatus is the same as described in Section 2-1. An electrolyte solution containing 0.01 mole of $K_3Fe(CN)_6$, 0.01 mole of $K_4Fe(CN)_6$ and 2 moles of NaOH per liter was circulated through the flow system and the temperature was controlled at a constant value of 30.00±0.05 deg C. In order to avoid the side reaction on the cathode, dissolved oxygen was purged with nitrogen before running and a positive nitrogen pressure was maintained in the flow system while running.

To obtain a good reproducibility of the measurement, the electrodes were polished with fine emery paper before each run. After each run, the probe was rinsed with demineralized water and wiped with a clean soft cloth. When this procedure was followed, the reproducibility of the measurements was within 3 %.

The electric circuit used is shown in Fig.(2-17). The electric potential of the probe(cathode) was held at -200 mV relative to a Hg_2O reference electrode with a potentio-

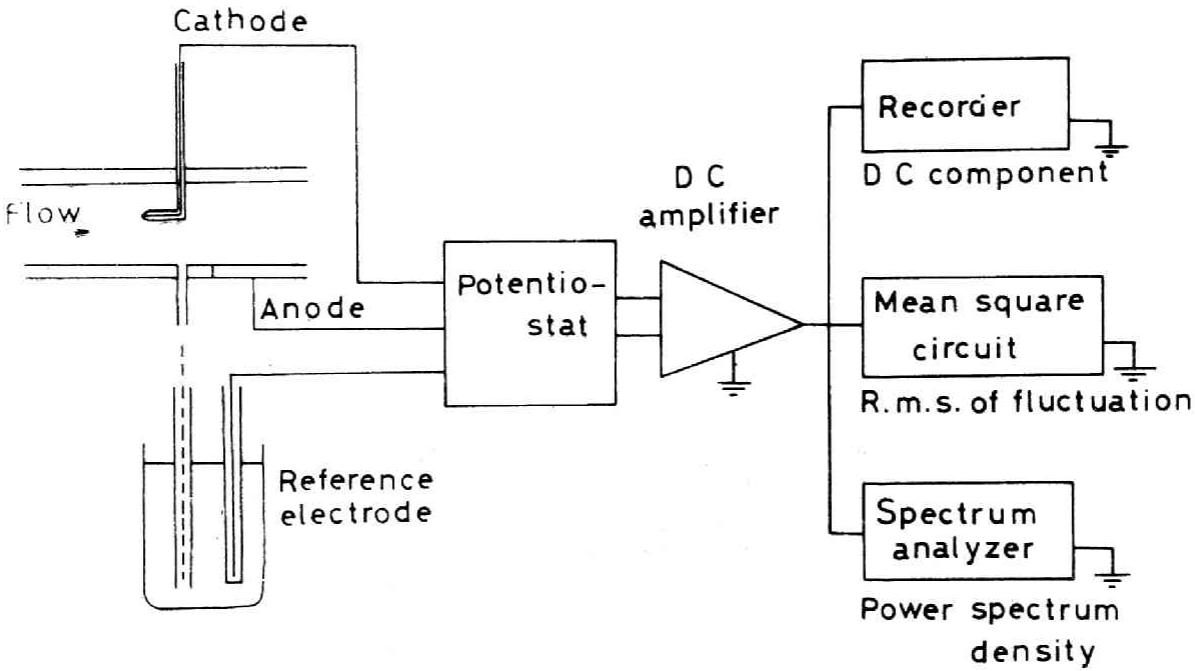

Fig.(2-17) Electric circuit for measurement of fluctuating velocity.

stat. The potentiostat can respond to a fluctuation of the electric potential within 10^{-5} sec and hold the potential constant even if the electric current at the cathode surface is fluctuating. Thus the electric current due to the potential fluctuation may be eliminated. The limiting current was amplified 10^{4} times with a D.C. amplifier. The root-mean-square of the fluctuating signal was measured by passing the signal through a square circuit and an averaging circuit and then to a recorder. Power spectrum densities were measured with a frequency analyser.

2-2-4 Distribution of turbulence intensity

The measured distributions of turbulence intensity based on the free stream velocity, u''/U_G were shown in Fig. (2-18). The measurements were carried out at the cross sections of x/D = 4.638,12.05 and 29.77. It will be noticed that the similarity exist in the distributions of turbulence intensity in any cross sections in the entrance region. The distribution of the turbulence intensity extends into the free stream region and the outer edge is approximately 1.2δ from the tube wall. When the distributions are compared with Klebanoff's results (29) obtained in the turbulent boundary layer flow over a flat

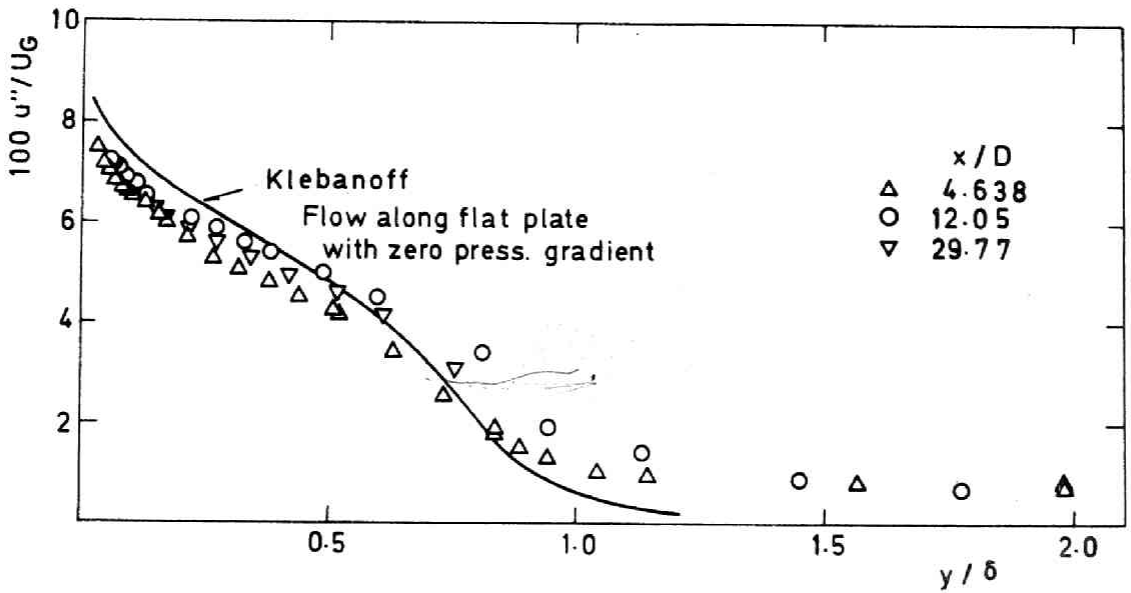

Fig.(2-18) Distribution of turbulence intensity, u'', in the entrance region of a circular tube.

plate with zero pressure gradient, it can be seen that these results agree with each other.

Small increases in the turbulence intensity with increasing x/D were detected in the non-turbulent region. This can be explained by velocity changes in the non-turbulent region caused by irregular motion of the boundary between turbulent boundary layer flow and non-turbulent flow. This is the so-called potential flow disturbance.

2-2-5 Power spectrum density of u'

The power spectrum densities of the velocity fluctuation u' were obtained at $y/\delta = 1.086$ and 0.136 at the cross section $x/D = 12.05$. The results presented in Fig. (2-19) are normalized as

$$\int_0^\infty W_\sigma \, d\sigma = 1 \qquad (2\text{-}14)$$

where the wave number σ is given by

$$\sigma = 2\pi \, n/u \qquad (2\text{-}15)$$

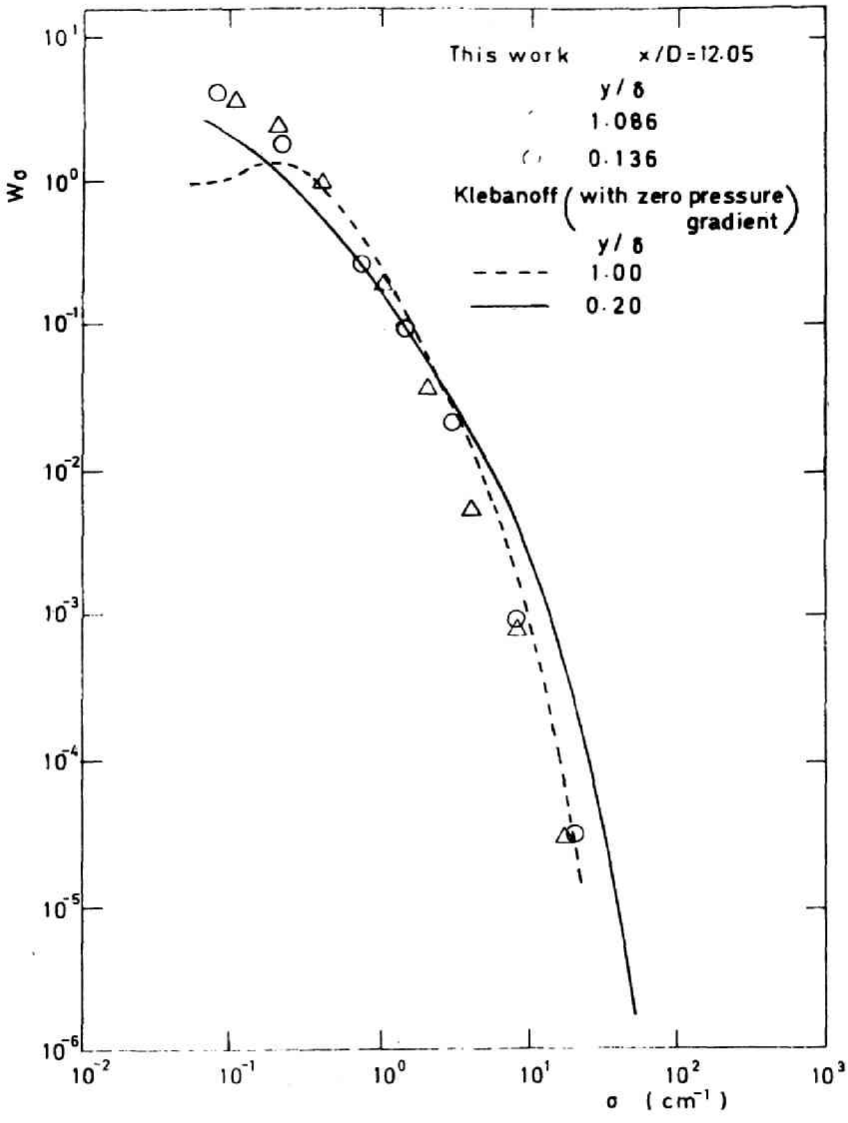

Fig.(2-19) Power spectrum density of u' in the entrance region of a circular tube.

The results obtained by Klebanoff for a flat-plate boundary layer are also represented in Fig.(2-19). There is a similarity in these results except the data of $y/\delta=1.086$ in the low frequency range. The discrepancy in the low frequency range seems to be due to the difference in mechanism of the intermittent flow in the outer portion of the boundary layer, and it is caused by the longitudinal pressure gradient. In the higher frequency range, the turbulent eddies are at local isotropic condition and the spectrum densities decrease in the same way as the Klebanoff's results. All of the spectrum have two extensive regions(23). One is the inertial sub-range where the spectrum varies in proportion to $\sigma^{-5/3}$ and the other is the highest frequency range where viscosity plays an important role and the spectrum is proportional to σ^{-7}.

As described in Section 2-2-2, the electrochemical method has a limited frequency range. This limit at which the amplitude ratio becomes 0.9, corresponds to $\sigma\sim20$. Accordingly, measurements up to $\sigma\sim20$ may be considered reliable.

Finally, it should be mentioned that the magnitude of the electrode potential had no effect on the spectra. This indicates that the reaction kinetics at the electrode surface do not influence the measurement of the fluctuating mass transfer and

that the concentration of the diffusing ions can be regarded as zero at the surface of the electrode.

2-2-6 Concluding remarks

As a result of this experimental and theoretical investigation, an electrochemical method based on a diffusion-controlled reaction was found to be a very useful and convenient method for measuring the turbulent stream velocity in liquid flow. If the measuring probe is made sufficiently small, it needs no compensation for amplitude attenuation and phase shift up to the sufficiently high frequency range

As a result of the experimental investigation by means of the electrochemical method, the following conclusions can be drawn concerning the turbulence mechanism in the entrance region of a circular tube.

1: Similarity exists in the distributions of turbulence intensity at any cross sections in the entrance region. These distributions agree closely with that in a boundary layer over a flat plate with zero pressure gradient.

2: The power spectrum densities of the fluctuating velocity u' at various values of y/δ in the entrance region show a re-

similarity with those for flat-plate boundary layer with zero-pressure gradient except the data of $y/\delta=1.086$ in the low frequency range seems to be due to the difference in mechanism of intermittent flow in the outer portion of the boundary layer, and is caused by the longitudinal pressure gradient.

Appendix 2-1 Electrochemical kinetics

The overall resistance of the electrode reaction consists of a series of partial resistances. In the ferri- and ferrocyanide system, three kinds of resistances are in series, viz. 1: the resistance to diffusion of the ferri-cyanide ion from the main stream to the cathode surface. 2: the resistance to electron-charge transfer at the cathode surface. 3: the resistance to diffusion of the reaction product from the cathode surface to the main stream.

The electrochemical kinetic theory may be used to predict the rates of transfer of electron-charge. The net current at the cathode is the sum of the anodic partial current density

and the cathodic one and may be represented as

$$\frac{i}{nF} = k_s\{C_{ox,w} f_{ox} \exp\{-\frac{\alpha nF}{RT}\eta_E\} - C_{red,w} f_{red} \exp\{\frac{(1-\alpha)nF}{RT}\eta_E\}\} \tag{2-16}$$

where α and k_s are the charge-transfer coefficient and the rate constant respectively. η_E is the overvoltage with respect to the equilibrium potential and f is the activity coefficient.

On the other hand, the diffusion process may be described with the mass transfer coefficient as

$$\frac{i}{nF} = K_{ox} (C_{ox,b} - C_{ox,w}) \tag{2-17-a,b}$$

$$\frac{i}{nF} = K_{red} (C_{red,w} - C_{red,b})$$

Combining Eqs.(2-16) and (2-17-a,b), one obtains the relationship between current density and potential as

$$\frac{i}{nF} = \frac{C_{ox,b} - \frac{f_{red}}{f_{ox}} C_{red,b} \exp\{\frac{nF}{RT}\eta_E\}}{\frac{1}{K_{ox}} + \frac{1}{K_{ox}} \frac{1}{f_{ox}} \exp\{\frac{nF}{RT}\eta_E\} + \frac{1}{K_{red}} \frac{f_{red}}{f_{ox}} \exp\{\frac{nF}{RT}\eta_E\}} \tag{2-18}$$

Measurement of the relationship between current density and potential was carried out with the blunt nose type probe

in a liquid stream of 20 deg C, containing 1 molar potassium hydroxide and equimolar quantities(0.01 mole) of ferri- and ferro-cyanide. The electric current was plotted against the potential difference between the cathode and the silver-oxide standard electrode. The equilibrium potential was 0.402 volt. The diffusion-controlling condition seemed to be established at about 0.25 volt. This condition was maintained until the potential becomes larger than the hydrogen overvoltage(approximately -1.2 volts) where the discharge current of hydrogen ions adds to the limiting current of the ferri- and ferro-cyanide redox system. The reaction rate constant k_s and the charge-transfer coefficient α have been determined to be 9.0×10^{-2} cm/sec and 0.61 respectively(6) when this redox reaction occurs on a platinum cathode at 20 deg C in the presence of 1 mole of KCl per liter. If these values of the reaction rate parameters, α and k_s, are accepted as the approximate values for this experimental condition, Eq.(2-18) predicts the current-potential relation and the result is plotted in Fig.(2-20). Since it agrees well with the experimental curve, it shows that these values of α and k_s are approximately correct. With these reaction rate parameters the contribution of the electron-charge transfer process to the overall reaction process may be predicted.

If the blunt nose type probe of 0.12 cm in diameter is im-

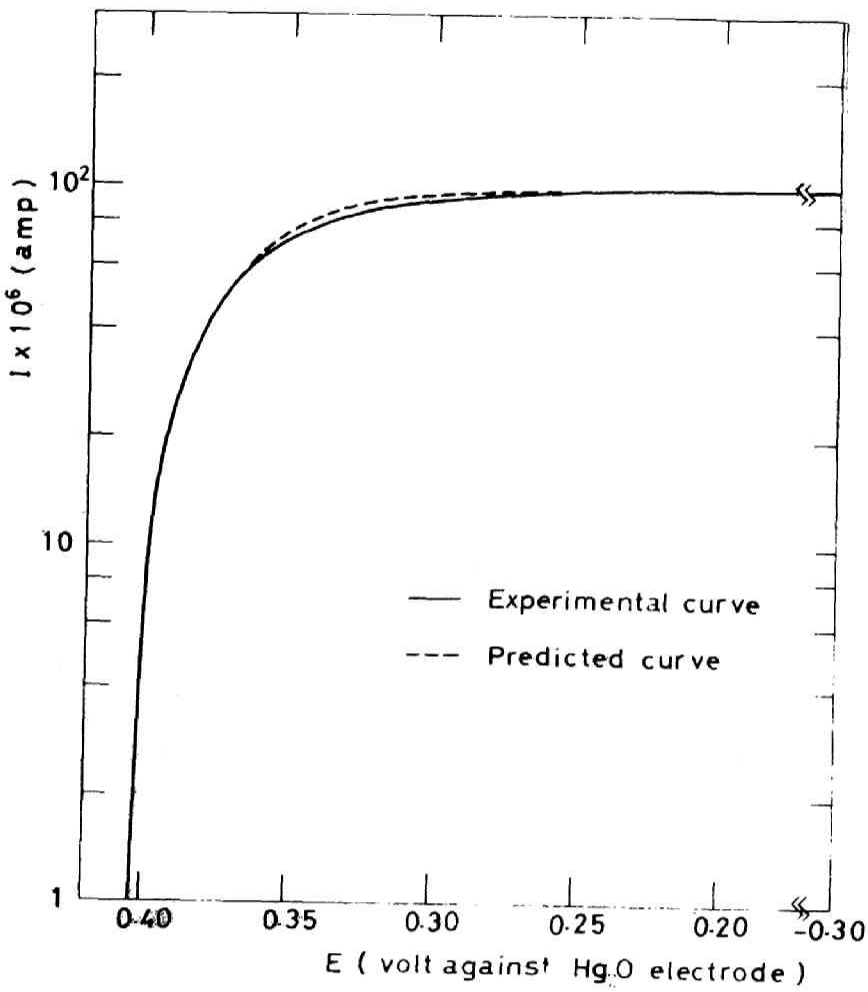

Fig.(2-20) Current - potential curve of ferri-cyanide ion reduction.

mersed in a flow of velocity u=100 cm/sec and the electric potential is held at -0.300 volt against the silver-oxide standard electrode, the concentration ratio $C_{ox,w}/C_{ox,b}$ is calculated to be 1.43×10^{-4}. Therefore, the concentration on the electrode surface may be regarded as zero. The influence of the electron-charge transfer process on the measurement of the fluctuating velocity may also be ignored. An experimental check was performed and mentioned in Section 2-2-5.

Appendix 2-2 Principle in the measurement of the turbulent velocity

In the electrochemical reaction under the diffusion controlling condition the electric current to the electrode surface of the velocity measuring probe is related to the liquid velocity. At large Schmidt numbers the correlations of mass transfer coefficients are very scarce. However, they are highly required for measuring the stream velocity by means of the electrochemical method.

Velocity measurement with the hot wire type probe is based

on mass transfer around a circular cylinder in cross flow. Van der Hegge Zijnen(79) compiled the results of many investigators and obtained the following correlation:

$$Sh = 0.38\ Sc^{1/5} + (0.56Re^{1/2}+0.001Re)\ Sc^{1/3} \qquad (2\text{-}19)$$

which is valid for Re=1∿500.

The mass transfer coefficient at the front stagnation point of a cylindrical electrode may be predicted by the methods described in Chapter 5 and may be represented approximately by the following equation:

$$Sh = 1.30\ Re^{1/2}\ Sc^{1/3} \qquad (2\text{-}20)$$

A comparison with the exact solution is given in Table 2-1 and shows that Eq.(2-20) is a good approximation at large Schmidt numbers.

Velocity measurement with the blunt-nose type probe is based on mass transfer at the stagnation point of an axi-symmetrical body. The rates of mass transfer are correlated approximately by the following equation;

$$Sh = 1.46\ Re^{1/2}\ Sc^{1/3} \qquad (2\text{-}21)$$

A comparison with the exact solution is also given in Table

2-2. Anyhow, at large Schmidt numbers the rates of mass transfer on the electrode surface of these probes are proportional to 1/3-power of the Schmidt number and 1/2-power of the Reynolds number.

For practical use, the limiting current is correlated by the following equation:

$$i = \alpha + \beta u^{0.5} Sc^{1/3}$$

Although Eqs.(2-19),(2-20) and (2-21) give a good estimation for the forced convection term of β , some inaccuracies cannot be avoided, that is, contribution of the natural convection term and inaccuracy of the dimension of the probe.

In the turbulent stream the momentary values of the limiting current and the velocity are assumed to be correlated by Eq.(2-12). (Here the amplitude attenuation and the phase lag of the limiting current from the velocity fluctuation is ignored. Those will be discussed in Appendix 2-3.) If u' is the fluctuating velocity component in the direction of the main stream $\overline{u}$ which is assumed to be perpendicular to the wire and if v' is the lateral one perpendicular to the wire, the effective velocity is written by

Table 2-1 Mass transfer at the stagnation point of a circular cylinder

Sc	$Sh/\sqrt{Re}$ Exact solution (Eqs. (5-9, 10))	$Sh/\sqrt{Re}$ Eq.(2-20)	Error %
11.0	2.78	2.89	+4.0
36.6	4.23	4.32	+2.1
122.0	6.39	6.44	+0.8
404.0	9.62	9.61	+0.1
1340	14.4	14.3	-0.7
4460	21.6	21.4	-0.9
14800	32.3	31.9	-1.2

Table 2-2 Mass transfer at the stagnation point of a sphere

Sc	$Sh/\sqrt{Re}$ Exact solution (Ref. (62))	$Sh/\sqrt{Re}$ Eq.(2-21)	Error %
11.0	3.14	3.25	+3.5
36.6	4.76	4.85	+1.9
122.0	7.17	7.24	+1.0
404.0	10.8	10.8	0.0
1340	16.6	16.1	0.0
4460	24.1	24.0	-0.3
14800	36.0	35.9	-0.3

$$u_{eff} = \left((\bar{u} + u')^2 + v'^2 \right)^{1/2} \qquad (2\text{-}22)$$

Substituting this equation into Eq.(2-12) and expanding the resulting equation into Taylor series, one obtains

$$\bar{i} + i' = \alpha + \beta \bar{u}^{\frac{1}{2}} \left(1 + \frac{u'}{2\bar{u}} - \frac{1}{8} \frac{u'^2}{\bar{u}^2} + \frac{1}{4} \frac{v'^2}{\bar{u}^2} + \ldots \right) \qquad (2\text{-}23)$$

By neglecting the higher order terms and after some algebraic calculation, one obtains the intensity of turbulence in the direction of main stream as follows:

$$(\bar{u}'^2)^{1/2} / \bar{u} = 2 (\bar{i}'^2) / (\bar{u}) \quad \beta \qquad (2\text{-}13)$$

Appendix 2-3 Response of the probe output signal to fluctuations in the stream velocity

For the measurement of the velocity fluctuations of liquid flow the electrochemical method has a serious problem that is a capacitance effect of the concentration boundary layer over the electrode surface. However, no consideration for this problem has been accomplished up to now. Even in the technique of the hot-wire anemometer, this effect may not be overlooked in measuring high frequency components of the velocity fluctuation.

The capacitance effect is the response of laminar heat and mass transfer to fluctuations in the velocity of oncoming flow. It is expected that this effect grows as diffusivity of heat or mass decreases. In the liquid flow of large Schmidt numbers as used in the electrochemical method, this effect must be considered.

In Chapter 5, effects of the velocity fluctuations on mass transfer around a cylinder in cross flow will be discussed. In that case the scale of turbulence is smaller than or comparable with the size of the cylinder and the interaction between eddies which increases the rate of heat or mass transfer is the most important problem, whereas in this case the scale of turb-

ulence is much larger than the electrode size so that the electrode is regarded to be immersed in a turbulent eddy where the free stream velocity around the electrode oscillates uniformly in magnitude. In two dimensional case Lighthill(34) solved the linearized equations for the response of laminar skin friction and heat transfer to fluctuations in the oncoming velocity. He calculated numerically the amplitude ratio and phase lag in the case of two dimensional stagnation flow at Pr=0.7. A similar calculation at large Schmidt numbers gives an reasonable estimation for the response of a hot-wire type probe in the electrochemical method.

In this section the response of a blunt-nose type probe to the velocity fluctuations will be analysed by an extension of the Lighthill's procedure to axi-symmetrical flow. The results obtained will be compared with those for two dimensional flow, and then the influence of the Schmidt number or the Prandtl number on the capacitance effect will be discussed.

Basic equations

The boundary layer equations for axi-symmetrical incompressible flow are

$$\frac{\partial(ur)}{\partial x} + \frac{\partial(vr)}{\partial y} = 0 \tag{2-24}$$

$$\frac{\partial u}{\partial t} + u\frac{\partial u}{\partial x} + v\frac{\partial u}{\partial y} + \frac{1}{\rho}\frac{\partial p}{\partial x} = \nu\frac{\partial^2 u}{\partial y^2} \tag{2-25}$$

$$\frac{\partial U}{\partial t} + U\frac{\partial U}{\partial x} + \frac{1}{\rho}\frac{\partial p}{\partial x} = 0 \tag{2-26}$$

$$\begin{aligned} &u = v = 0 \quad \text{at } y = 0 \\ &u \to U(x,t) \quad \text{at } y \to \infty \end{aligned} \tag{2-27}$$

where r denotes the distance of a point on the wall from the axis of symmetry. The equation of conservation of mass is written as

$$\frac{\partial C}{\partial t} + u\frac{\partial C}{\partial x} + v\frac{\partial C}{\partial y} = D\frac{\partial^2 C}{\partial y^2} \tag{2-28}$$

$$C = C_w \quad \text{at } y = 0, \quad C = C_b \quad \text{at } y \to \infty \tag{2-29}$$

One now assumes that the fluctuations in the free stream velocity, U(t, x), are produced by fluctuations of the oncoming velocity in magnitude but not in direction. Secondly, if the oncoming velocity is written by

$$U_\infty \quad (1 + \varepsilon e^{i\omega t})$$

,then since irrotational flow responds instantaneously to alterations in the conditions producing it, the free stream velocity may be assumed to fluctuate by the same factor so that

$$U(t, x) = U_0(x) \quad (1 + \varepsilon e^{i\omega t}) \qquad (2\text{-}30)$$

One now supposes that the quantities(u,v,C) are all performing small oscillations around those steady means, and writes

$$u = u_0(x, y) + \varepsilon u_1(x, y)e^{i\omega t}, \quad v = v_0(x, y) + \varepsilon v_1(x, y)e^{i\omega t}$$

$$C = C_0(x, y) + \varepsilon C_1(x, y)e^{i\omega t} \qquad (2\text{-}31,32,33)$$

Substituting these equations into Eq.(2-25) and retaining only the terms of order ε, one obtains linearized equations and its boundary conditions as

$$i\omega u_1 + u_0 \frac{\partial u_1}{\partial x} + \frac{\partial u_0}{\partial x} u_1 + v_0 \frac{\partial u_1}{\partial y} + \frac{\partial u_0}{\partial y} v_1 = i\omega U_0 + \frac{dU_0^2}{dx} + \nu \frac{\partial^2 u_1}{\partial y^2} \qquad (2\text{-}34)$$

$$u_1 = v_1 = 0 \quad \text{at } y = 0, \quad u_1 \to U_0 \quad \text{at } y \to \infty \qquad (2\text{-}35)$$

$$i\omega C_1 + u_0 \frac{\partial C_1}{\partial x} + \frac{\partial C_0}{\partial x} u_1 + v_0 \frac{\partial C_1}{\partial y} + \frac{\partial C_0}{\partial y} v_1 = D \frac{\partial^2 C_1}{\partial y^2} \qquad (2\text{-}36)$$

$$C_1 = 0 \qquad \text{at } y = 0 \quad \text{and } y \to \infty \tag{2-37}$$

Solution for large ω

For large ω, only the terms involving ω and the derivative of highest order are retained in Eq.(2-34). The solution of this equation may be easily obtained as

$$u_1 = U_0 \left(1-e^{-y\sqrt{i\omega/\nu}} \right) \tag{2-38}$$

For a spherical body, $r(x)$ is obtained geometrically as

$$r(x) = R \sin(x/R) \tag{2-39}$$

Substituting Eqs.(2-38) and (2-39) into the equation of continuity, Eq.(2-24), one obtains the transverse velocity v_1 as

$$v_1 = - \left\{ \frac{dU_0}{dx} + \frac{U_0}{x} \right\} \left\{ y + \frac{1}{\sqrt{i\omega/\nu}} \left(1-e^{-y\sqrt{i\omega/\nu}} \right) \right\} \tag{2-40}$$

Let us now consider the response of mass transfer. For small y, C_0 may be approximated by $C_0 = C_w + y(\partial C_0/\partial y)_w$. Substitution of this equation into the right hand side of Eq.(2-36) gives

$$C_1 = - \frac{i}{\omega} \frac{dU_0}{dx} \left(\frac{\partial C_0}{\partial y} \right)_{y=0} \left\{ y - \frac{1-Sc+Sc\ e^{-y\sqrt{i\omega/\nu}} - e^{-y\sqrt{i\omega/D}}}{(1-Sc)\sqrt{i\omega/\nu}} \right\} +$$

$$+\frac{i}{\omega}U_0\left(\frac{\partial^2 C_0}{\partial x \partial y}\right)_{y=0}\left\{y+\frac{Sc}{1-Sc}\,y\,e^{-y\sqrt{i\omega/\nu}}+\left(\frac{2Sc}{1-Sc}\right)^2\frac{e^{-y\sqrt{i\omega/\nu}}-e^{-y\sqrt{i\omega/D}}}{\sqrt{i\omega/\nu}}\right\} \tag{2-41}$$

Then the mass transfer rate at the front stagnation point of a sphere is obtained as

$$N = D\left.\frac{\partial C_0}{\partial y}\right|_{y=0}\left\{1-e^{i\omega t}\left(\frac{2i}{\omega}\frac{dU_0}{dx}\frac{1}{1+\sqrt{Sc}}\right)\right\} \tag{2-42}$$

Solution for $\omega \to 0$

The solution of Eqs.(2-34) and (2-36) in the limiting case $\omega \to 0$ is called as the quasi-steady solution to be denoted by (u_s, v_s, C_s). Since the velocity distribution in the laminar boundary layer is generally discribed in the form(see ref.(57))

$$u_0 = U_\infty\, f(x/R,\ y\sqrt{U_\infty/\nu R}) \tag{2-43}$$

so that

$$u_s = u_0 + \varepsilon U_\infty \frac{\partial u_0}{\partial U_\infty} = u_0 + \varepsilon\frac{1}{2}\,y\,\frac{\partial u_0}{\partial y} \tag{2-44}$$

and similarly

$$C_s = C_0 + \varepsilon\frac{1}{2}\,y\,\frac{\partial C_0}{\partial y} \tag{2-45}$$

Then the mass transfer rate is given as

$$N = D \left.\frac{\partial C_0}{\partial y}\right|_{y=0} \{1 + \frac{1}{2} \varepsilon e^{i\omega t}\} \qquad (2\text{-}46)$$

Solution for small ω

For small ω, it is convenient to write

$$(u_1, v_1, C_1) = (u_s, v_s, C_s) + i\omega\,(u_2, v_2, C_2) \qquad (2\text{-}47)$$

Substituting Eq.(2-47) into Eqs.(2-34) and (2-36), and using the fact that (u_s, v_s, C_s) is a solution for $\omega \to 0$, one obtains the equations for (u_2, v_2, C_2), that is,

$$\frac{\partial u_2 r}{\partial x} + \frac{\partial v_2 r}{\partial y} = 0 \qquad (2\text{-}48)$$

$$i\omega u_2 + u_0 \frac{\partial u_2}{\partial x} + \frac{\partial u_0}{\partial x} u_2 + v_0 \frac{\partial u_2}{\partial y} + \frac{\partial u_0}{\partial y} v_2 - \nu \frac{\partial^2 u_2}{\partial y^2} = U_0 - u_s \qquad (2\text{-}49)$$

$$i\omega C_2 + u_0 \frac{\partial C_2}{\partial x} + v_0 \frac{\partial C_2}{\partial y} - D \frac{\partial^2 C_2}{\partial y^2} = -C_s - \frac{\partial C_0}{\partial x} u_2 - \frac{\partial C_0}{\partial y} v_2 \qquad (2\text{-}50)$$

At first let us consider the velocity field. For very small ω, Lighthill obtained a solution for two-dimensional stagnation flow, using the Pohlhausen's approximate method(53). In this analysis for axi-symmetrical flow the approximate meth-

od presented by Tomochika(74) will be used. In solving the equation of motion by the approximate method, one makes use of the last equation at $y \to 0$;

$$\nu \left(\frac{\partial^2 u_2}{\partial y^2}\right)_{y=0} = - U_0(x) \tag{2-51}$$

and the integral form of Eq.(2-49) after eliminating v_0 and v_2 by the equation of continuity. Then one obtains

$$-U_o(x) = \frac{1}{2}\int_0^\infty (U_0 - u_0)dy + \left(U_0\frac{d}{dx} - i\omega + U_0\frac{1}{r}\frac{dr}{dx}\right)\int_0^\infty u_2 dy$$

$$-\left(2\frac{d}{dx} + 2\frac{1}{r}\frac{dr}{dx}\right)\int_0^\infty u_0 u_2 dy \tag{2-52}$$

Unperturbed velocity u_0 in Eq.(2-52) is approximated by the quartic velocity profile, that is,

$$u_0/U_0 = 1 - (1-\eta)^3\{\, 1+(1-\tfrac{1}{6}\Lambda)\,\eta\,\} \tag{2-53}$$

where Λ is a shape factor defined by $(\delta^2/\nu)(dU_0/dx)$. Substituting Eq.(2-53) into Eq.(2-25), one obtains the basic equation for predicting the growth of the boundary layer around the spherical body. Near the stagnation point, the following relations hold true:

$$U_0 = \beta x = 3U_\infty x/d, \quad \Lambda = 4.716$$

$$\frac{1}{r}\frac{dr}{dx}\frac{U_0}{U_0'} = 1 \ , \qquad \frac{d\Lambda}{dx} = 0 \tag{2-54}$$

Now for u_2, another quartic profile may be assumed

$$u_2 = \frac{U_0\delta^2}{\nu}(1-\eta)^2\{ A\eta + (2A-\tfrac{1}{2})\eta^2 \} \tag{2-55}$$

This inherently satisfies all of the boundary conditions. Substitution of Eqs.(2-53) and (2-55) into Eq.(2-52) gives

$$U_0\delta A = \frac{36-\Lambda}{240}U_0\delta + (U_0\frac{d}{dx} - i\omega + U_0\frac{1}{r}\frac{dr}{dx})(\frac{9A-1}{60}\frac{U_0\delta^3}{\nu})$$
$$-(2\frac{d}{dx} + 2\frac{1}{r}\frac{dr}{dx})\{(\frac{263A-32}{2520} + \Lambda\frac{10A-1}{6048})\frac{U_0^2\delta^3}{\nu}\} \tag{2-56}$$

For small ω and constant Λ, the second and third terms of the right hand side of Eq.(2-56) may be neglected. This neglection was verified by Lighthill for the two dimensional case and may be also verified for the axi-symmetrical case, so that

$$A = (36 - \Lambda)/240 \tag{2-57}$$

Let us now consider the mass transfer rate. For this purpose one may use the approximate method which may be deduced by some extention of Dienemann's method(9) presented for two dimensional flow. At first an unperturbed concentratation pro-

file is assumed to be

$$C_0/C_w = (1-a\eta)^3 (1+a\eta) \tag{2-58}$$

where a is the ratio of the hydraulic boundary layer thickness to the concentration one, i.e., $a=\delta/\delta_c$. Substituting Eqs.(2-53) and (2-58) into the equation of conservation of mass, Eq. (2-28), and integrating the resulting equation over the concentration boundary layer, one obtains the following equation for a ($a \geq 1$):

$$\frac{2a}{Sc} = \{\Lambda + (\frac{1}{r}\frac{dr}{dx}\frac{U_0}{U_0'})\Lambda + \frac{1}{2}U_0 z' + U_0 z \frac{d}{dx}\}$$

$$\times\{\frac{2}{15}a^{-2} - \frac{3}{140}a^{-4} + \frac{1}{180}a^{-5} + \Lambda(\frac{1}{90}a^{-2} - \frac{1}{84}a^{-3} + \frac{3}{560}a^{-4} - \frac{a^{-5}}{1080})\} \tag{2-59}$$

where $z=\delta^2/\nu$. At the stagnation point, a is obtained by

$$\frac{a}{Sc} = \Lambda\{\frac{2}{15}a^{-2} - \frac{3}{140}a^{-4} + \frac{a^{-5}}{180} + \Lambda(\frac{1}{90}a^{-2} - \frac{1}{84}a^{-3} + \frac{3}{560}a^{-4} - \frac{a^{-5}}{1080})\} \tag{2-60}$$

Here a quartic profile is also assumed for C_2:

$$C_2 = BC_w \frac{\delta^2}{\nu} a\eta(1-a\eta)^2(1+2a\eta) \tag{2-61}$$

which also inherently satisfies all the boundary conditions.

Substituting these profiles into Eq.(2-50) and taking into account for the fact that Λ, A and a are constant at the stagnation point, then one obtains the equation for B (for $a \geq 1$):

$$-B\frac{a}{Sc} = -\frac{3}{20}\frac{1}{a} + (i\omega/\beta)B\frac{3\Lambda}{20a} + 2\Lambda\{A(\frac{1}{15}a^{-2} - \frac{9}{280}a^{-4} + \frac{1}{90}a^{-5})$$

$$+(-\frac{1}{84}a^{-3} + \frac{3}{280}a^{-4} - \frac{1}{360}a^{-5})\} + 2\Lambda B\{\frac{2}{15}a^{-2} - \frac{3}{70}a^{-4}$$

$$+\frac{a^{-5}}{72} + \Lambda(\frac{1}{90}a^{-2} - \frac{1}{56}a^{-3} + \frac{3}{280}a^{-4} - \frac{1}{432}a^{-5})\} \qquad (2\text{-}62)$$

From Eqs.(2-45) and (2-47) the rate of mass transfer at the stagnation point is given by

$$N = D\frac{\partial C_0}{\partial y}\Big|_{y=0}\{1 + \frac{1}{2}\epsilon e^{i\omega t}(1-(i\omega/\beta)\Lambda B)\} \qquad (2\text{-}63)$$

Figure(2-21) shows the amplitude ratio and the phase lag of mass transfer from those in quasi-steady state. In this diagram the broken lines show both the solution for small ω and that for large ω, and the full lines are the conjectural curves which are seen to be fairly good representations. In Figs.(2-22) and (2-23) the dependence of the frequency response on the Prandtl or the Schmidt numbers are shown for two dimensional and axi-symmetrical flow respectively. These diagrams may be used to compensate the amplitude attenuation of the out-

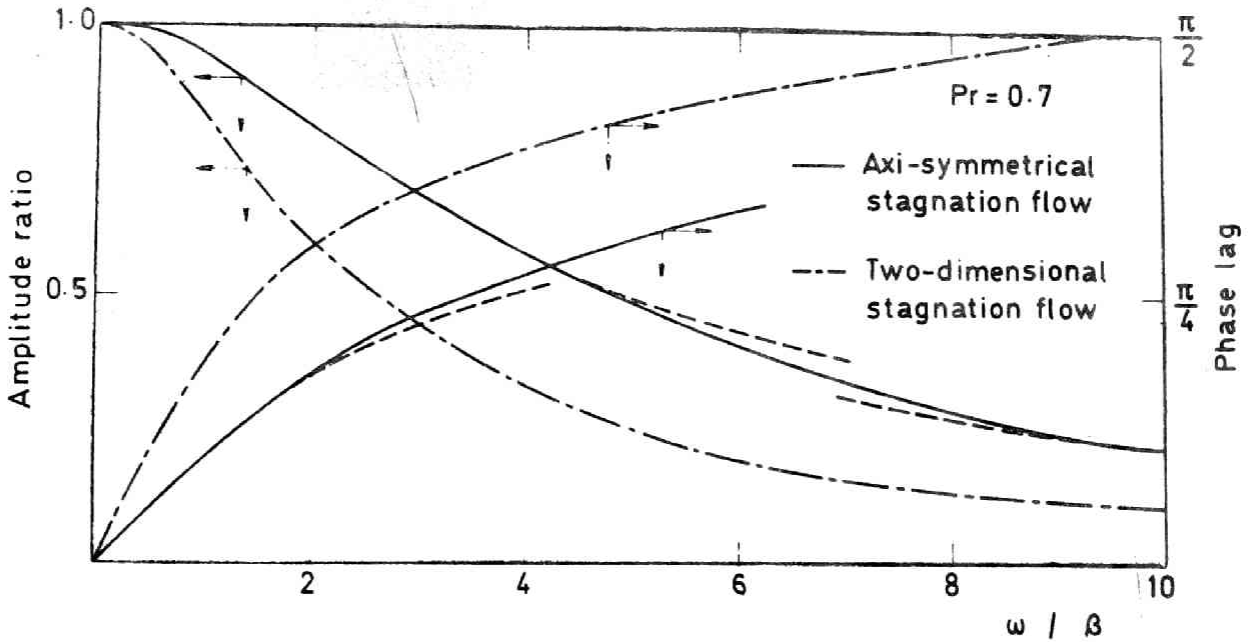

Fig.(2-21) Response of mass transfer to velocity fluctuations in two dimensional flow ($\beta=4U_\infty/D$) and axi-symmetrical flow ($\beta=3U_\infty/D$).

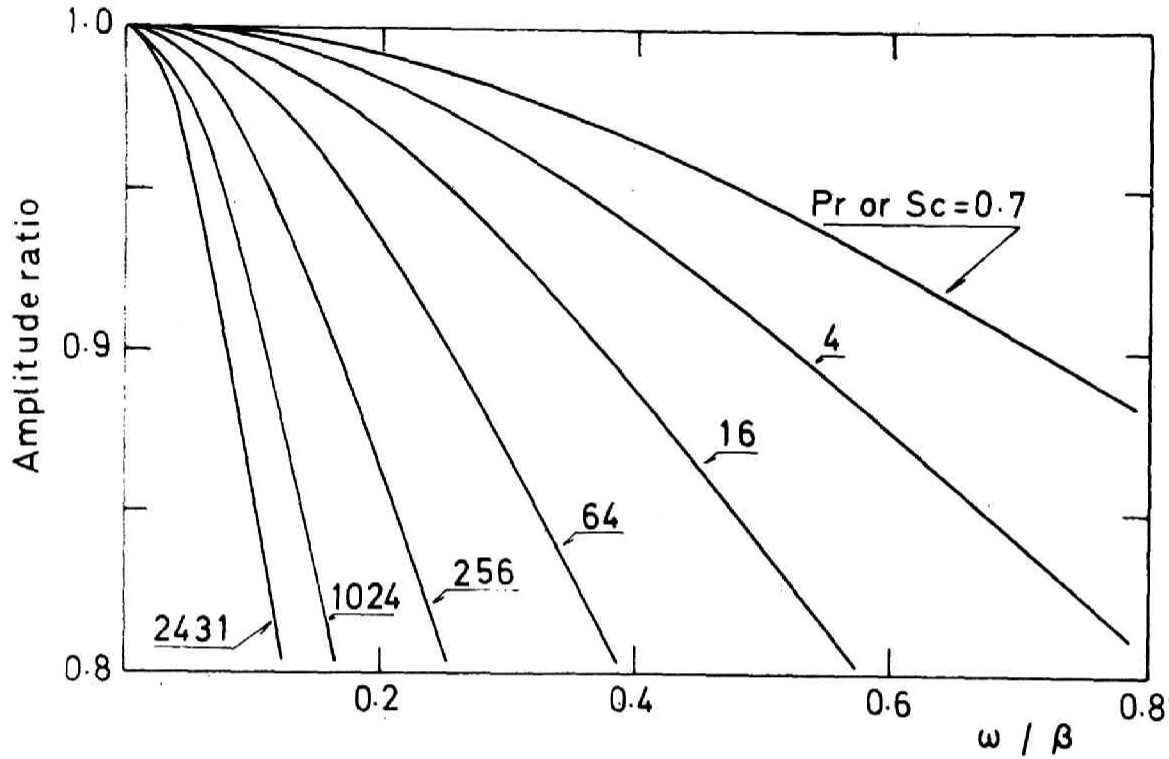

Fig.(2-22) Dependence of frequency response on Pr or Sc number for two dimensional stagnation flow ($\beta=4U_\infty/D$).

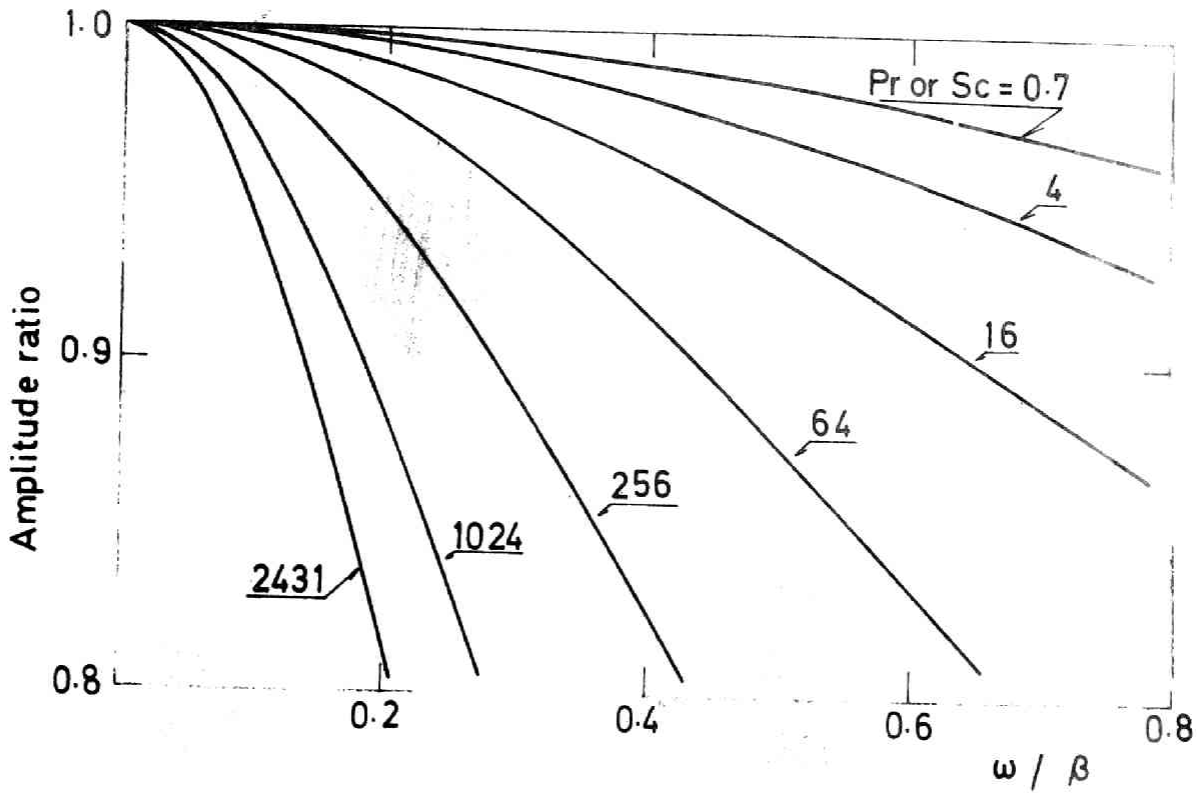

Fig.(2-23) Dependence of frequency response on Pr or Sc number for axi-symmetrical stagnation flow ($\beta=3U_\infty/D$).

put signal of the velocity measuring probe. In Fig.(2-24) the critical frequency at which the amplitude ratio becomes equal to 0.9 is plotted against the Prandtl or Schmidt number. This diagram may be useful for an estimation of the upper limit up to which one may need no compensation for amplitude attenuation for a practical point of view.

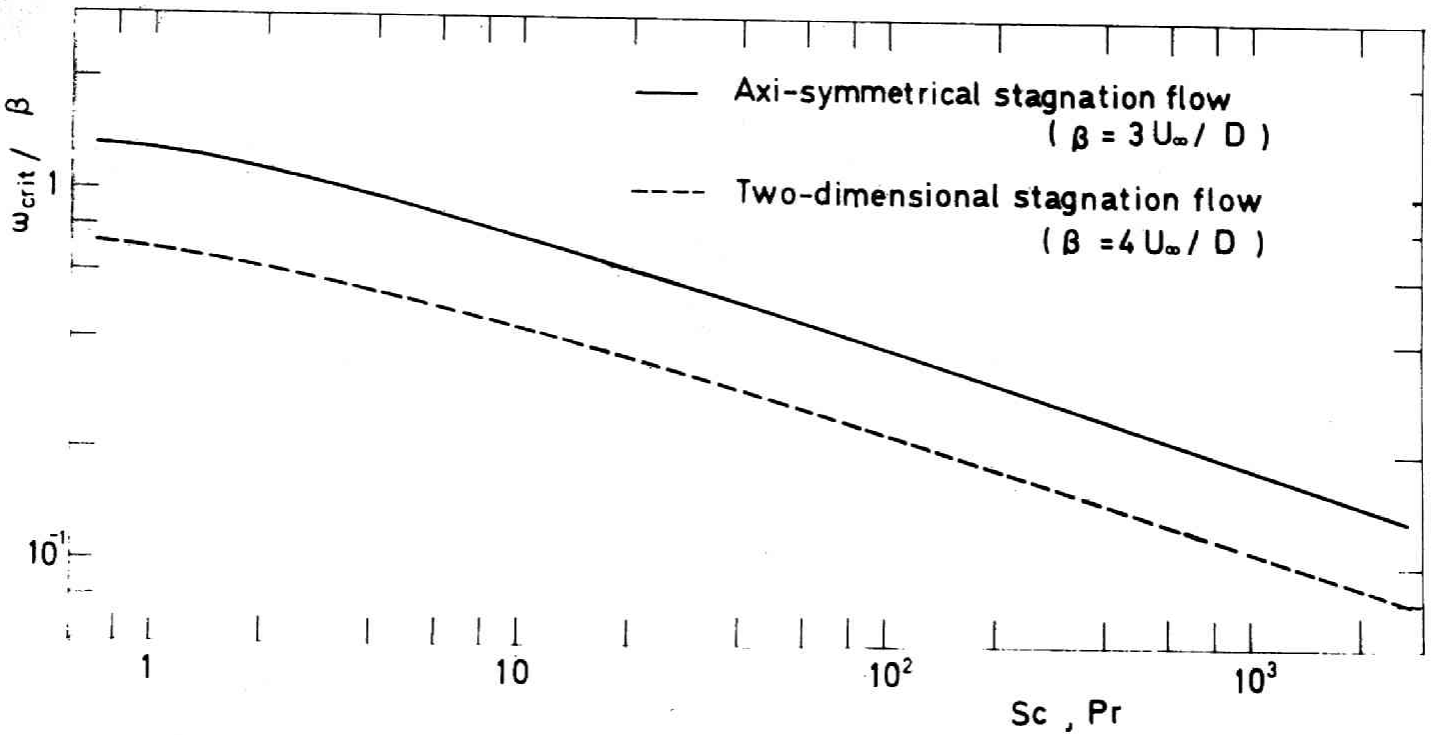

Fig.(2-24) Variation of critical frequency with Pr or Sc number.

CHAPTER 3

DEVELOPMENT OF THE BOUNDARY LAYER

3-1 Purpose

The knowlegde of the development of the turbulent boundary layer in the entrance region of a circular tube is of special importance for the design of working sections of wind tunnels and for the design of hydraulic systems. It is also important for the design of heat exchangers and tubular reactors. There have been few experimental works for the development of the turbulent boundary layer in the entrance region. In addition, the variation of the skin friction along the flow direction have not been measured. According to the measurements performed by Kirsten(56), the fully developed velocity profile exists after an inlet length of 50 to 100 diameters. But Nikuradse(52) obtained its length to be about 25 to 40 diameters. The discrepancy of these results is surprising.

On the other hand the entrance-region problem has been solved for turbulent boundary layers by several investigators (7, 8, 15, 32, 33, 55, 77, 78). However, all of them assumed the velocity profile to be equal to that for the fully developed flow.

The purposes of the work covered in this chapter are

1: To measure the boundary layer quantities such as the boundary layer thickness as careful as possible.

2: To measure the skin friction directly.

3: To predict the development of the boundary layer by use of the expressions of the velocity profile which represent in itself the effect of the longitudinal pressure gradient.

3-2 Theoretical prediction: method I (with one-parameter velocity profile)

3-2-1 One-parameter velocity profile

The method I is based on the assumption of a similarity which exists in the velocity distributions at any cross sections in the entrance region. The similar velocity profile is represented by Eq.(3-1):

$$u^+ = c\,(y^+)^{1/m} \tag{3-1}$$

The coefficient c and the exponent m are characteristic values of the flow in the entrance region and depend only on the inlet Reynolds number (see Eqs.(2-2) and (2-3)). Substituting the condition of $u=U_G$ at $y=\delta$ into Eq.(3-1), one obtains the skin friction factor, c_f, based on U_G as follows:

$$\frac{c_f}{2} = \frac{\tau_w}{\rho U_G^2} = c^{-2m/(m+1)} \left\{\frac{U_G \delta}{\nu}\right\}^{-2/(m+1)} \tag{3-2}$$

3-2-2 Basic equations

The equation of motion and the equation of continuity are

$$u\frac{\partial u}{\partial x} + v\frac{\partial u}{\partial y} = -\frac{1}{\rho}\frac{dp}{dx} + \frac{\partial}{r\partial r}\left(r\nu_e \frac{\partial u}{\partial r}\right) \tag{3-3}$$

$$\frac{\partial ur}{\partial x} + \frac{\partial vr}{\partial y} = 0 \tag{3-4}$$

In analysing the boundary layer flow in a circular tube, the adequate definitions of the displacement thickness and the momentum thickness are introduced as

$$\delta_1 = \int_0^R \left(1-\frac{u}{U_G}\right)\left(1-\frac{y}{R}\right) dy \tag{3-5}$$

$$\delta_2 = \int_0^R \left(1-\frac{u}{U_G}\right) \frac{u}{U_G} \left(1-\frac{y}{R}\right) dy \qquad (3\text{-}6)$$

Integrating Eq.(3-3) from y=0 to y=R and using the equation of continuity and the definition of the displacement and the momentum thicknesses, one obtains the momentum equation as follows. This is formally identical to that for two dimensional flow.

$$\frac{d\delta_2}{dx} + (H+2) \frac{\delta_2}{U_G} \frac{dU_G}{dx} = \frac{c_f}{2} \qquad (3\text{-}7)$$

where H is a shape factor defined as

$$H = \delta_1 / \delta_2 \qquad (3\text{-}8)$$

This equation is valid provided only that there exists an undisturbed central core(free stream) in which the shear stress is zero. In this central core, the Bernoulli's equation is established along each streamline and the longitudinal pressure gradient is related to the velocity gradient by

$$\frac{dp}{dx} = -\rho U_G \frac{dU_G}{dx} \qquad (3\text{-}9)$$

The macroscopic mass balance for circular tube flow gives

$$\pi R^2 U_E = \int_0^R 2\pi r u \, dr \tag{3-10}$$

By use of the definition of the displacement thickness, Eq.(3-10) leads to

$$\delta_1 = \frac{R}{2}\left(1 - \frac{U_E}{U_G}\right) \tag{3-11}$$

Substituting Eq.(3-1) into Eqs.(3-5) and (3-6), one obtains the following expressions for δ_1 and δ_2 which are functions of δ only.

$$\delta_1 = \frac{\delta}{m+1} - \frac{\delta^2}{2R(2m+1)} \tag{3-12}$$

$$\delta_2 = \frac{m\delta}{(m+1)(m+2)} - \frac{m\delta^2}{2R(2m+1)(m+1)} \tag{3-13}$$

δ is expressed by δ_1 by accepting only minus sign of two roots of Eq.(3-12)

$$\frac{\delta}{R} = \frac{2m+1}{m+1}\{1 - B(\delta_1)\} \tag{3-14}$$

where

$$B(\delta_1) = \sqrt{1 - \frac{(m+1)^2}{2m+1}\frac{2\delta_1}{R}} \tag{3-15}$$

From Eq.(3-13) and (3-14), δ_2 is expressed by δ_1 as

$$\frac{\delta_2}{R} = \frac{m}{m+1}\frac{\delta_1}{R} - \frac{m(2m+1)}{(m+1)^3(m+2)}\{1 - B(\delta_1)\} \tag{3-16}$$

Substituting Eqs.(3-2) and (3-16) into the momentum equation, one obtains the basic equation for δ_1:

$$\frac{d\delta_1}{dx} = c^{-\frac{2m}{m+1}}\left\{\frac{2m+1}{2(m+1)}\,Re_E\frac{R(1-B(\delta_1))}{R-\delta_1}\right\}^{-\frac{2}{m+1}}$$

$$\times\left\{\frac{m}{m+1}\left\{1-\frac{1}{(m+2)B(\delta_1)}\right\} + (\delta_1+2A(\delta_1))\frac{2}{R-2\delta_1}\right\}^{-1} \tag{3-17}$$

where

$$A(\delta_1) = \frac{m}{m+1}\delta_1 - \frac{m(2m+1)}{(m+1)^3(m+2)}(1-B(\delta_1))R \tag{3-18}$$

The boundary condition for Eq.(3-17) is

$$\delta_1 = 0 \quad \text{at } x = 0 \tag{3-19}$$

The differential equation was solved by a standard Runge-Kutta procedure on the Kyoto University KDC II digital computer. When δ_1 was obtained, all values of U_G/U_E, δ, δ_2 and c_f could be calculated.

3-3 Theoretical prediction: method II

(with two-parameter velocity profile)

3-3-1 Two-parameter velocity profile

The two-parameter velocity profile was presented in Section 2-1 as

$$u/U_G = Z_E\,(y/\delta)^{1/m} + (1-Z_E)\,\{1-\cos(\pi y/\delta)\}/2 \qquad (3\text{-}20)$$

where

$$Z_E = c\,Re_G^{1/m}\,(c_f/2)^{(1+m)/2m} \qquad (3\text{-}21)$$

Though both Eqs.(3-1) and (3-20) represent the velocity profile in the wall region very well, Eq.(3-20) is a better representation in the outer region of the boundary layer. However, Eq.(3-1) involves in itself a relation between the skin friction factor and the boundary layer thickness as represented by Eq.(3-2). In contrast with that, Eq.(3-20) does not present the relation like Eq.(3-2). In other word, Eq.(3-20) is a two-parameter velocity profile. Hence, in order to determine three independent quantities δ, c_f, U_G, one more differential equation as well as the macroscopic mass balance and the momentum equation are required. This may be satisfied by the introduc-

tion of the entrainment theory.

3-3-2 Entrainment function

The entrainment theory was presented by Head(20) who related the shape parameter of the velocity profile to the rate of fluid entrained in the boundary layer. His assumption is that the rate of irrotational fluid entering the region of turbulent motion depends on the intensity of velocity fluctuations near the outer edge of the turbulent boundary layer. On the other hand, the turbulent shear stress, which controls the velocity profile, is also a function of the fluctuation intensity. It is thus plausible to postulate a dependence between the rate of entrainment and the shape of the velocity profile. In two dimensional flow, the amount of fluid entrained per unit length and unit width of the layer is assumed to be

$$\frac{dQ}{dx} = \frac{d}{dx}\{\int_0^{\delta} u\, dy\} = \frac{d}{dx}\{U_G(\delta-\delta_1)\} = U_G\, F(H) \qquad (3\text{-}22)$$

where F(H) is referred to as the "entrainment function" which is a dimensionless function of the shape factor, H. Several recommendations for the entrainment function have been made by the previous investigators(11, 20, 51, 67, 68). Those curves

are plotted in Fig.(3-1) along with the experimental results (49,59). These results are scattering and a strong support for choosing one entrainment function from others can not be found. Since Nicoll's entrainment function is given in a simpler form and seems to correlate many experimental results as well as those of this work, his function is chosen in this analysis, that is,

$$F(H) = 0.0354\sqrt{H-1.25} \qquad (3\text{-}23)$$

3-3-3 Basic equation

The auxiliary equation(3-22) was derived for two dimensional flow. For axi-symmetrical flow as exists in the entrance region, this equation must be modified on the basis of the physical concept of the entrainment theory. The auxiliary equation for axi-symmetrical flow is derived from the mass balance in the boundary layer and written as

$$\frac{dQ}{dx} = \frac{d}{dx}\int_0^{\delta} u(R-y)\,dy = \frac{d}{dx}\{U_G(\delta-\delta_1)\} = F(H)(R-\delta)U_G \qquad (3\text{-}24)$$

With the dimentionless quantities defined as

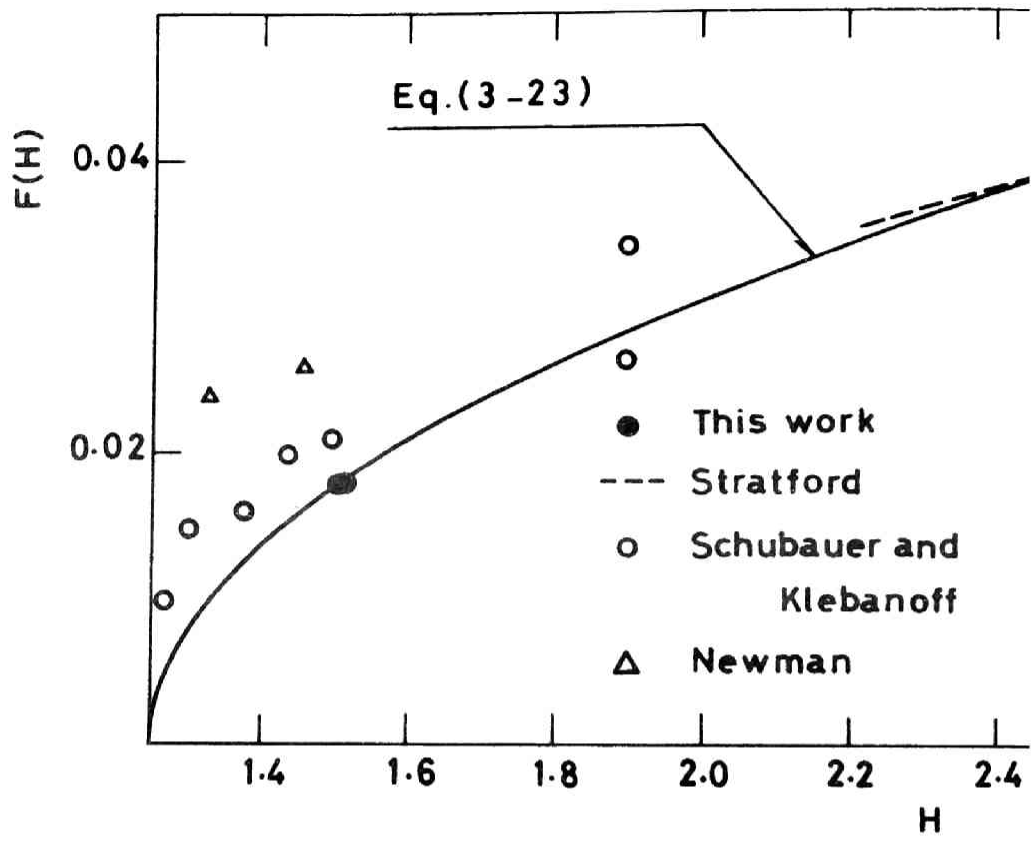

Fig.(3-1) Entrainment function.

$$Re_\delta = \frac{U_G\ \delta}{\nu} \quad , \quad Re_1 = \frac{U_G\ \delta_1}{\nu}$$

$$Re_2 = \frac{U_G\ \delta_2}{\nu} \quad , \quad Re_x = \int_0^x \frac{U_G}{\nu}\, dx \qquad (3\text{-}25)$$

the basic equations can be written as:

Auxiliary equation

$$\frac{d\ Re_1}{d\ Re_x} = F(H)\ (1 - \frac{\delta}{R}) \qquad (3\text{-}26)$$

Momentum equation

$$\frac{d\ Re_2}{d\ Re_x} + (1+H)\ \frac{d(\ln U_G)}{d\ Re_x}\ Re_2 = \frac{c_f}{2} \qquad (3\text{-}27)$$

Macroscopic mass balance

$$\frac{d(\ln U_G)}{d\ Re_x} = \{Re_\delta - (Re_x - 2Re_1)/\ 2(dRe_1/dRe_x)\}^{-1} \qquad (3\text{-}28)$$

As done by Spalding, let us introduce the following quantities

$$I_1 = \int_0^1 \frac{u}{U_G}\ (1 - \eta\ \frac{\delta}{R}\ )\ d\eta, \quad I_2 = \int_0^1 (\frac{u}{U_G})^2 (1 - \eta\ \frac{\delta}{R})\ d\eta$$

$$F = \int_0^1 (1 - \eta\ \frac{\delta}{R})\ d\eta$$

then the boundary layer thicknesses are represented by these

quantities:

$$\delta_1 = \delta(F-I_1), \qquad \delta_2 = \delta(I_1-I_2)$$

With these definitions the basic equations may be rewritten as

$$Re_\delta(I_{1\delta}Re'_\delta+I_{1s}c_f')+ I_1Re'_\delta = F(H)\ (1-2Re_\delta/Re_G) \tag{3-29}$$

$$Re_\delta\{(I_1-I_2)Re'_\delta+(I_{1s}-I_{2s})c'_f\}+(I_1-I_2)Re'_\delta + Re_\delta(I_1-I_2)(1+H)\frac{d(lnU_G)}{d\ Re_x} = \frac{c_f}{2} \tag{3-30}$$

$$\frac{d(lnU_G)}{d\ Re_x} = \frac{4}{Re_G}(F-I_1)Re'_\delta - Re_\delta(I_{1\delta}Re'_\delta+I_{1s}c'_f)-\frac{Re_\delta Re'_\delta}{Re_G} \tag{3-31}$$

where the prime denotes differentiation with respect to Re_x and

$$I_{1\delta}=\partial I_1/\partial Re_\delta,\ I_{2\delta}=\partial I_2/\partial Re_\delta,\ I_{1s}=\partial I_1/\partial c_f,\ I_{2s}=\partial I_2/\partial c_f$$

These equations are the basic equations for the prediction of the boundary layer growth and have independent variables which are Re_δ, c_f and U_G. With the velocity profile of Eq.(3-20) and the entrainment function of Eq.(3-23), three basic equations of Eqs.(3-29),(3-30) and (3-31) should be solved simultaneously. The calculations were performed by the n-th order Runge-Kutta procedure on the Kyoto University FACOM 230-60 digital comput-

er. Since the skin friction factor, c_f, should be infinite at x=0, the numerical calculation can not be performed from x=0. As the starting values for calculation, the values of Re_δ, c_f and U_G predicted by the method I at x/D=0.1 were used.

3-4 Boundary layer thickness

The measurements were made by use of two kinds of leading edges, i.e., one with a trip wire and another without a trip wire. The longitudinal distributions of the boundary layer thickness for $Re_E=5\times10^4$ and 1×10^5 are shown in Fig.(3-2) where the boundary layer thickness is defined as y-distance at which $u/U_G=0.99$. The point of effective zero thickness is determined by the extrapolation of the uncorrected data for δ vs. x to be denoted by x_0. The abscisa, x, in Figs.(3-2)∿(3-6) was corrected with x_0.

If there is no trip wire, at first a laminar boundary layer develops and then a turbulent boundary layer is achieved. This is confirmed by the change of shape factor, H, defined as the ratio of the displacement thickness and the momentum thickness, as shown in Figs.(3-3-a,b). In the laminar boundary lay-

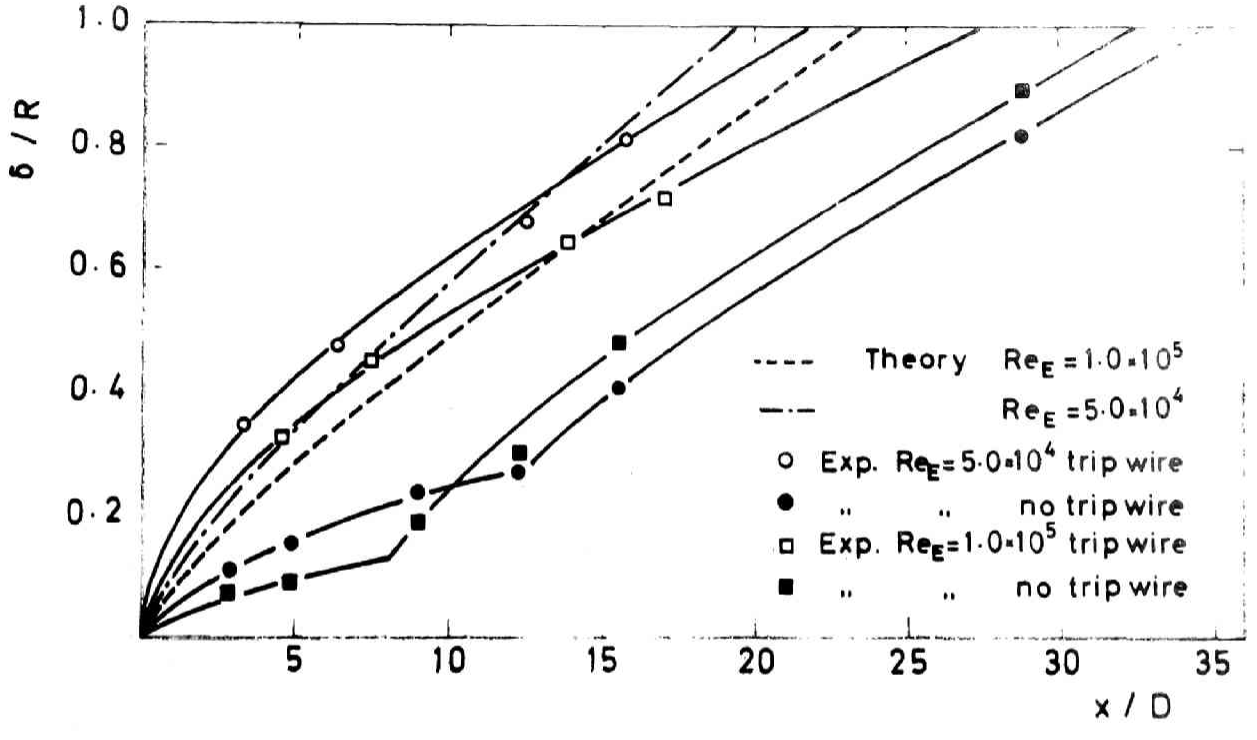

Fig.(3-2) Development of boundary layer thickness.

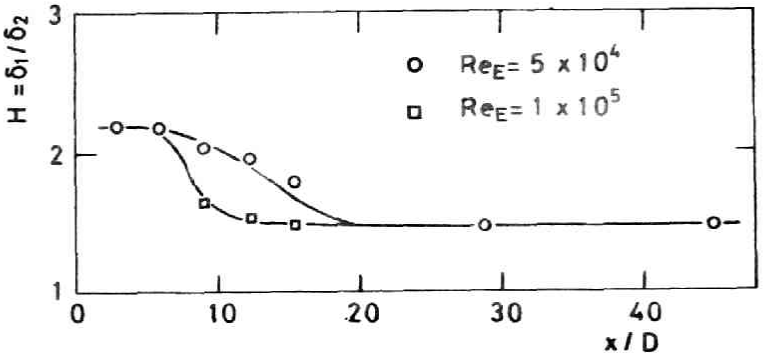

Fig.(3-3-a) Variation of shape factor with x/D in the case without trip wire.

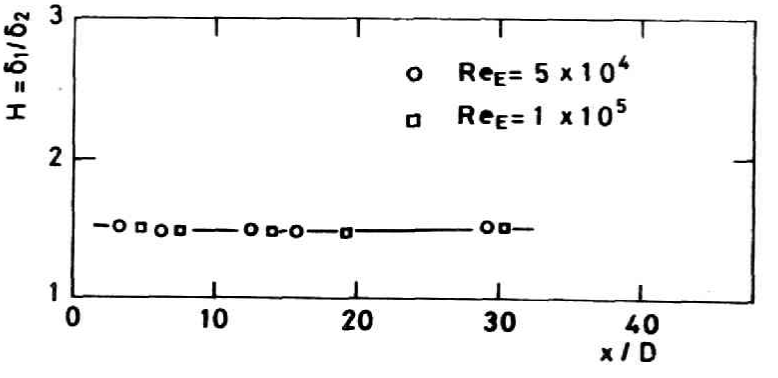

Fig.(3-3-b) Variation of shape factor with x/D in the case with trip wire.

er H is approximately 2.2 and it gradually decreases to the value 1.35 for the turbulent boundary layer in the region of $5<x/D<20$. If the transition point is defined as the point of inflection of the curve(δ vs. x/D), the transition Reynolds number , $U_E x_c/\nu$, is 6.2×10^5 and 7.7×10^5 at $Re_E=5\times10^4$ and 1×10^5 respectively. These values fall in the range of the transition Reynolds number for the boundary layer over a flat plate. When the length of the entrance region is defined as the length from the tube inlet to the point at which the boundary layer thickness becomes equal to the tube radius, it is 32.4 and 34.8 diameters for $Re_E=5\times10^4$ and 1×10^5 respectively.

In another case with trip wire, H is nearly constant and the curves of δ vs. x/D show smoothly increasing distributions. From these facts the boundary layers as exist in this region can be presumed to be turbulent from the leading edge. The length of the entrance region is 22.0 and 27.4 diameters for $Re_E=5\times10^4$ and 1×10^5 respectively. According to the measurement performed by Kirsten, its length is about 50 to 100 diameters. Later on, Nikuradse carried out an experiment of the flow in the entrance region and found that the fully developed velocity profile exists already after an inlet length of 25 to 40 diameters. The results of this work agrees with the Nikuradse's results. As shown later, this results also agree with the pre-

dicted ones. Therefore, the Kirsten's results are not acceptable. This seems to be due to the flow condition at the inlet cross section of the test tube, such as deformed velocity profile and swirling motion of the flow.

The longitudinal distributions of dimensionless free stream velocity, U_G/U_E, for $Re_E=5\times10^4$ and 1×10^5 are plotted against x/D in Fig.(3-4). The displacement and the momentum thicknesses are calculated from the measured velocity distributions and are plotted in Figs.(3-5) and (3-6).

In these diagrams theoretical curves predicted by the method I and II are also plotted. It is surprising that the difference between the curves predicted by these two methods is not distinguishable, although expressions of the velocity profile employed in these methods are slightly different with each other in the outer region of the boundary layer. This seems to be due to the choice of the entrainment function made in the method II.

The theoretical curves agree fairly well with the experimental results. The agreement confirms the availability of the method I and II to predict the flow behavior in the entrance region of a circular tube. When the method I and II are com-

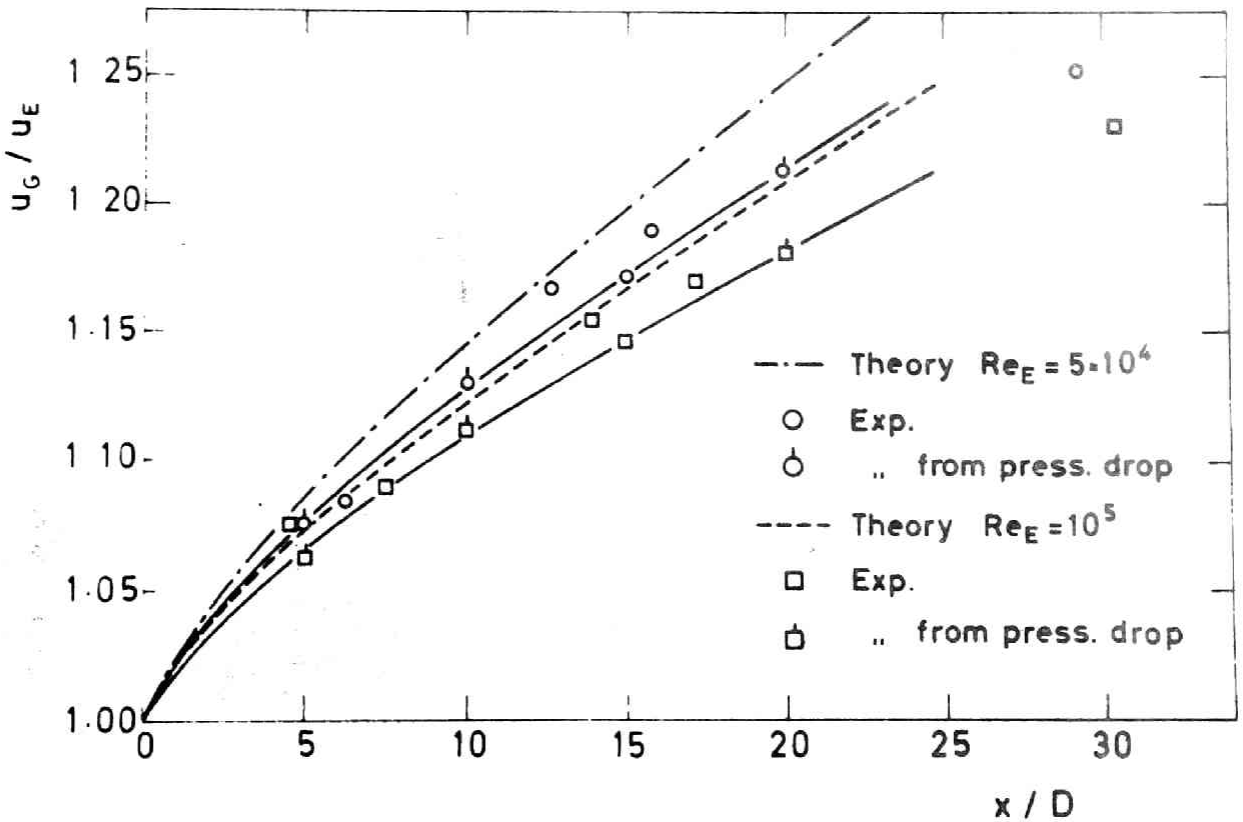

Fig.(3-4) Variation of U_G/U_E with x/D.

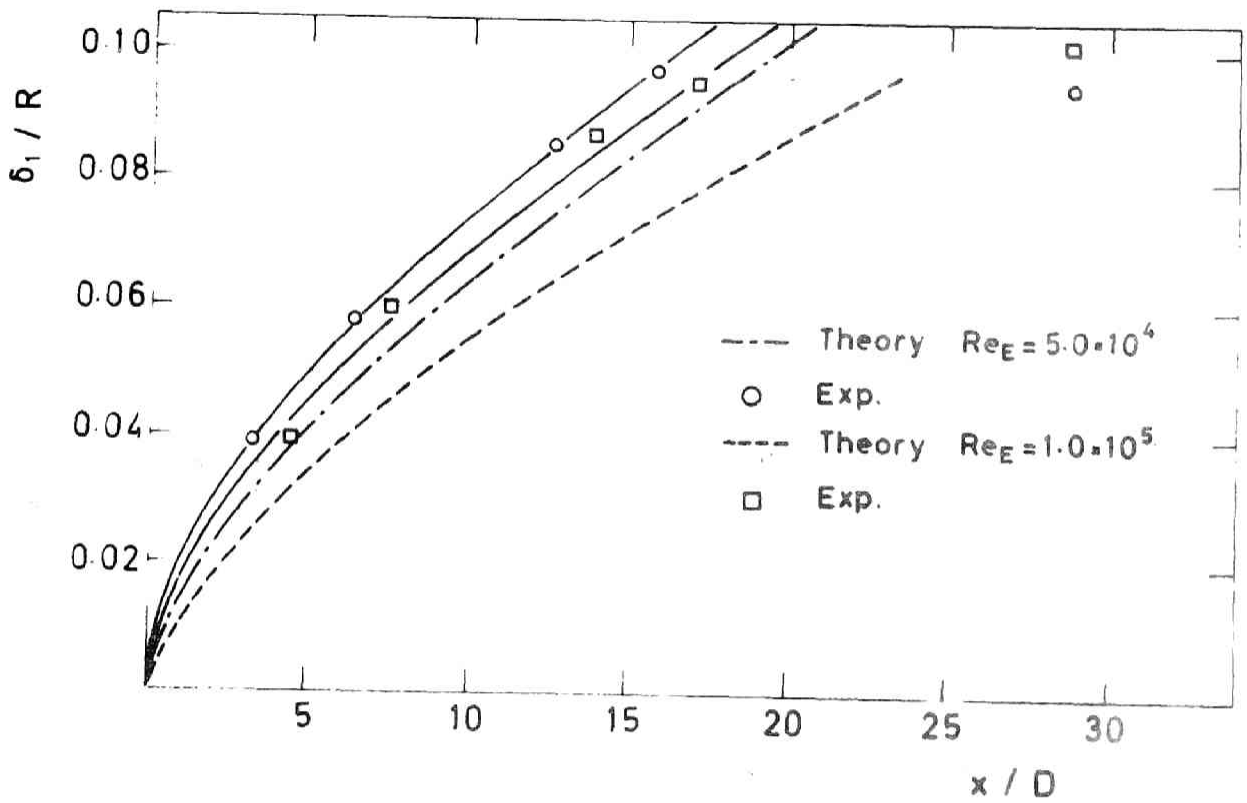

Fig.(3-5) Development of displacement thickness.

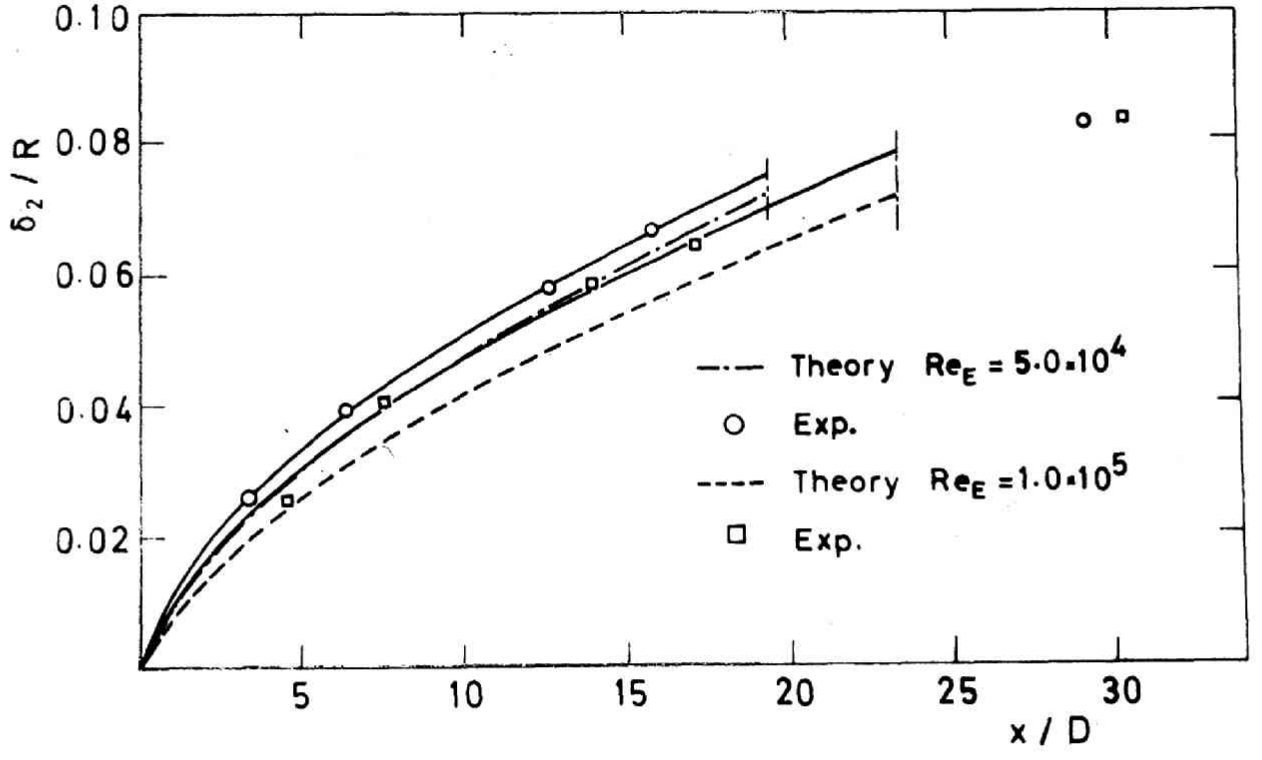

Fig.(3-6) Development of momentum thickness.

pared, in the method II the velocity profile is more adequate but the entrainment function is only an empirical formula. Furthermore, the calculation followed by the method II is more laborious. Therefore it is recommended to use the method I for the prediction of the growth of the boundary layer in the entrance region.

3-5 Skin friction

The skin friction is one of the most important properties for the understandings of the flow field and for the prediction of the heat and mass transfer. In spite of this importance, there have been no reliable and convenient method which may be used in the boundary layer flow with pressure gradients except for the method used by Ludwieg and Tillmann(37). The preston tube and the sublayer fence which have been applied in the flat-plate boundary layer flow have a defect since these techniques are affected by the longitudinal pressure gradient. Ludwieg and Tillmann used a hot film sticked on the wall and obtained the skin friction from the heat loss of the film. The electro-chemical method may also be applied to obtain the skin friction (43,44,45).

3-5-1 Principle, method and equipment in the measurement of the skin friction

A diffusion controlled reaction on the surface of a small electrode of 1 mm in diameter enbedded in the tube wall is used to measure directly the shear stress on the tube wall. In this experiment, the reaction which occurs on the test electrode is reduction of ferri-cyanide in the presence of a large excess of potassium hydroxide which eliminates the migration of reacting ions.

Since the size of the electrode for the measurement of the skin friction is very small and since the Schmidt number of the electrolyte solution is very large, the concentration boundary layer thickness is much thinner than the viscous sublayer thickness and the velocity field is approximated by the following equations:

$$u = s(X)\, y = \{\tau(X)/\mu\}\, y \tag{3-32}$$

$$v = -\int_0^y \frac{\partial u}{\partial X}\, dy = -\frac{1}{2} y^2 \frac{d\, s(X)}{d\, X} \tag{3-33}$$

where X is longitudinal distance from upstream edge of mass transfer section. This is schematically shown in Fig.(3-7). The equation of conservation of the diffusing species leads to

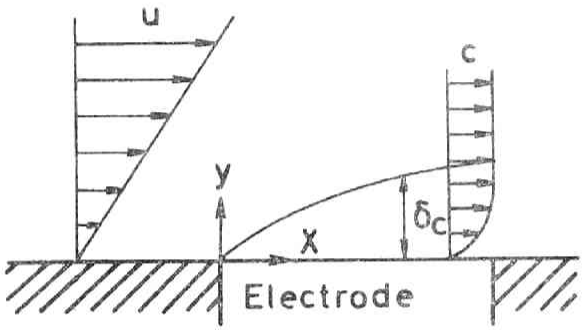

Fig.(3-7) Concentration and velocity profiles over electrode surface.

$$u\frac{\partial C}{\partial X} + v\frac{\partial C}{\partial y} = D\frac{\partial^2 C}{\partial y^2} \qquad (3\text{-}34)$$

Here, the transport of mass by eddy motion is neglected since the concentration changes occur only at the vicinity to the wall. The contribution of the eddy motion to the mass transfer process will be discussed in Chapter 4. Since the concentration at the electrode surface is zero under diffusion controlling condition, the initial and boundary conditions are given as

$$\begin{aligned} &C = 0 \quad \text{at } y = 0 \quad \text{for all } X > 0 \\ &C = C_b \quad \text{at } y \to \infty \quad \text{for all } x > 0 \\ &C = C_b \quad \text{at } X = 0 \quad \text{for all } y > 0 \end{aligned} \qquad (3\text{-}35)$$

Assuming a similar concentration profile given by

$$C = C(\eta) \qquad (3\text{-}36) \qquad \text{where } \eta = y/\delta_c(X) \qquad (3\text{-}37)$$

and substituting it into Eq.(3-34), then one obtains

$$D\frac{d^2C}{d\eta^2} - \eta^2\frac{dC}{d\eta}\{-s(X)\,\delta_c^2(X)\frac{d\delta_c(X)}{dX} + \frac{1}{2}\frac{ds(X)}{dX}\delta_c(X)\} = 0 \qquad (3\text{-}38)$$

Since C is a function of η only, and δ_c is a function of X only, Eq.(3-38) leads to

$$\frac{d^2C}{d\eta^2} + \alpha^2\eta^2\frac{d\,C}{d\,\eta} = 0 \qquad (3\text{-}39)$$

$$s(X)\frac{d\delta_c(X)}{d\,X} + \frac{1}{2}\frac{ds(X)}{d\,X}\,\delta_c(X) + \alpha^2\frac{D}{\delta_c^2(X)} = 0 \qquad (3\text{-}40)$$

where α is an arbitrary constant and is chosen to be $\alpha^2=3$. Equation(3-39) and the boundary condition lead to

$$C(\eta) = C_b \int_0^\eta e^{-\eta^3}\,d\eta \;/\; \int_0^\infty e^{-\eta^3}\,d\eta \qquad (3\text{-}41)$$

Equation(3-40) is a Bernoulli-type equation and the introduction of a new variable $z=\delta_c^3$ transforms this equation into a linear differential equation. With the initial condition, the transformed equation is solved as

$$\delta_c^3(X) = \exp\{-\int_0^X \frac{3}{2s(X)}\frac{ds(X)}{d\,X}\,dX\} \int_0^X \frac{9D}{s(X)}\exp\{\int_0^X \frac{3}{2s(X)}\frac{ds(X)}{d\,X}\,dX\}dX \qquad (3\text{-}42)$$

With Eqs.(3-41) and (3-42) the mass transfer coefficient is obtained as

$$K(X) = \frac{1}{\Gamma(4/3)}\left\{\frac{D}{9}\right\}^{1/3}\frac{s(X)^{1/2}}{\{\int_0^X s(X)^{1/2}dX\}^{1/3}} \qquad (3\text{-}43)$$

An estimation of $s(X)$ or $\tau_w(X)$ from the momentum equation shows

that except for a region in the vicinity to the leading edge the variation of s(X) in Eq.(3-32) over the electrode surface may be neglected. Then Eq.(3-43) is reduced into the Lévêque solution written by

$$K(X) = \frac{1}{\Gamma(4/3)} \left\{\frac{D^2 s}{9X}\right\}^{1/3} \tag{3-44}$$

The mass transfer averaged over the electrode surface is

$$\langle K(L_e) \rangle = \frac{3}{2\Gamma(4/3)} \left\{\frac{\tau_w D^2}{9 L_e \mu}\right\}^{1/3} \tag{3-45}$$

The measurements of electric current to the test electrode determine the values of mass transfer coefficient<K> from which s(X) can be calculated by Eq.(3-45). Then the skin friction, τ_w, is obtained. As shown by Hanratty et al.(60), if the circular electrode is considered as a rectangle whose effective length in the direction of flow is L_e and whose space-averaged mass transfer coefficient is equal to that for a circular electrode, then one obtains

$$\frac{1}{L_e} \int_0^{L_e} K(X)\, dX = \frac{\int K(X)\, dA}{\pi d_e^2 / 4} \tag{3-46}$$

Space integration of the above equation gives

$$L_e = 0.8136\, d_e \qquad (3\text{-}47)$$

3-5-2 Preliminary experiment

In order to confirm the principle of the skin friction measurement, a preliminary experiment was carried out in the fully developed tube flow where the skin friction remains constant in the flow direction and so is simply related with the pressure drop.

The electrodes used were small platinum wires of 1.035 and 1.000 mm in diameter and were mounted flush with the pipe wall as shown in Fig.(3-7). These electrodes were located at the position of x/D=100 from the entrance of the tube where the fully developed velocity profile was established. Measurements were performed at the Schmidt number of Sc=2586 in the Reynolds number range of $2\times10^{3} < Re_E < 7\times10^{4}$. The reproducibility of the measurements ranged within 3 %. In Fig.(3-8) the data are represented in the form of skin friction factor based on the mean velocity, along with that obtained from the pressure drop. These results agree very well with each other and also with the Blasius equation, i.e.,

$$c_f' = 0.0791\, Re_E^{-1/4}$$

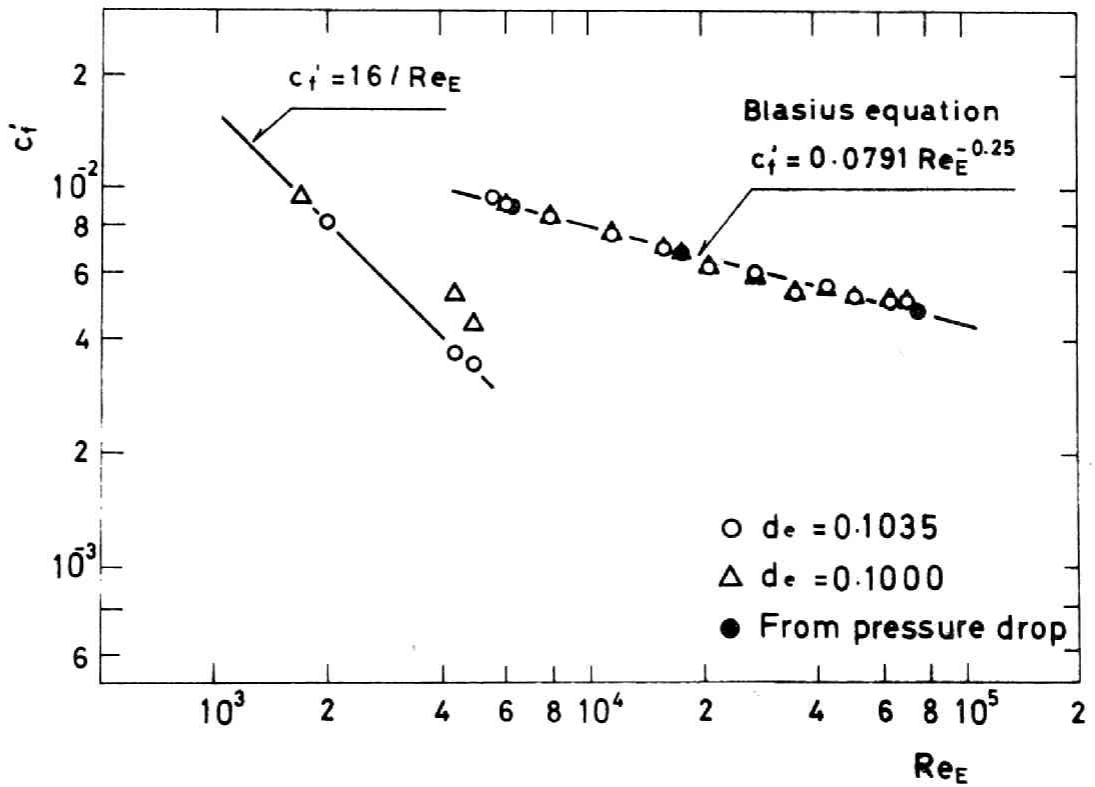

Fig.(3-8) Skin friction factor in the fully developed flow region of a circular tube.

These agreement confirms that the skin friction measurement based on the electrochemical method is very useful.

3-5-3 Distribution of the local skin friction factor

The longitudinal distributions of the friction factor based on the inlet velocity in the case with trip wire are shown in Fig. (3-9). The distributions of the skin friction factor are calculated from the prediction method I and are shown in this diagram. These predicted curves are in good agreement with the experimental results. From this agreement the validity of the method I is confirmed.

In order to examine the behavior in the vicinity to the inlet of the tube the same measurements were made at Reynolds numbers of $Re_E=1x10^4$, $2x10^4$and $3x10^4$ in the test section which will be described in Section 4-3. The representative curves of the experimental results are drawn in Fig.(3-10). For $x/D> 1$, the agreement with the predicted curve is very good. However, for $x/D<1$ the experimental results show the poor agreement with the predicted curve. The reason may be that the disturbances produced by the trip wire cause considerable alterations in the velocity profile which are, however, obliterated in the down-

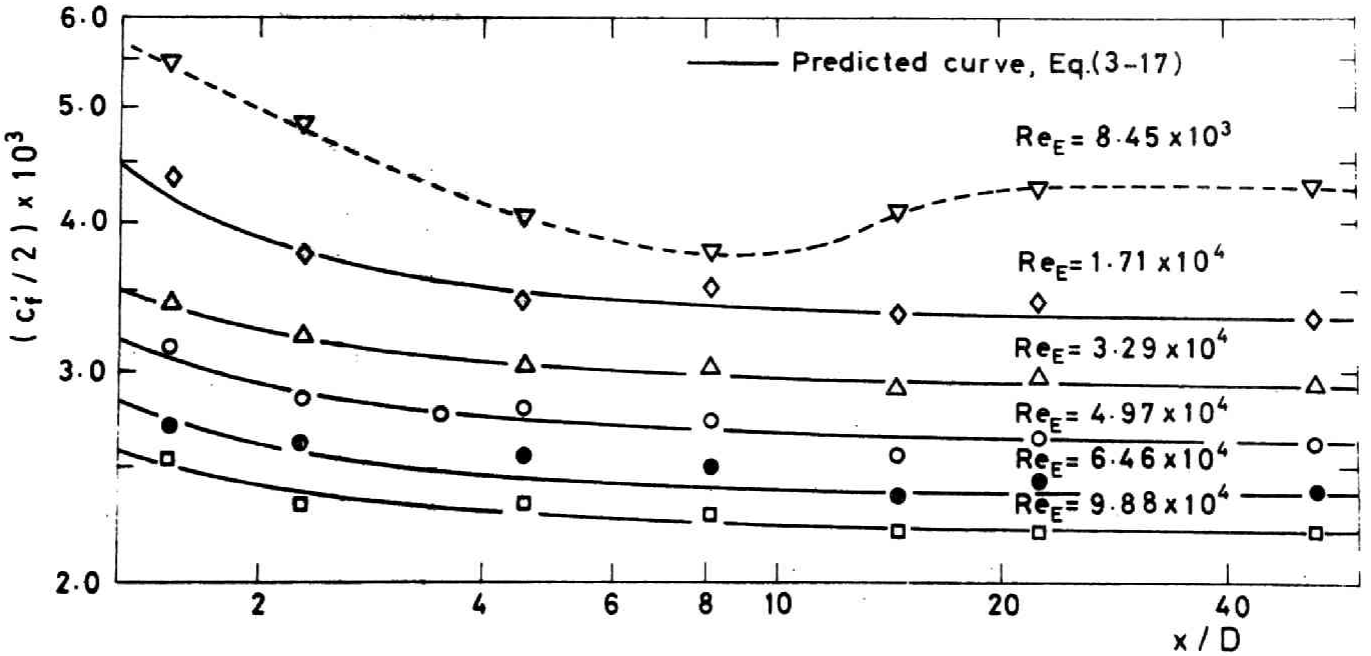

Fig.(3-9) Longitudinal distribution of skin friction factor in the entrance region of a circular tube.

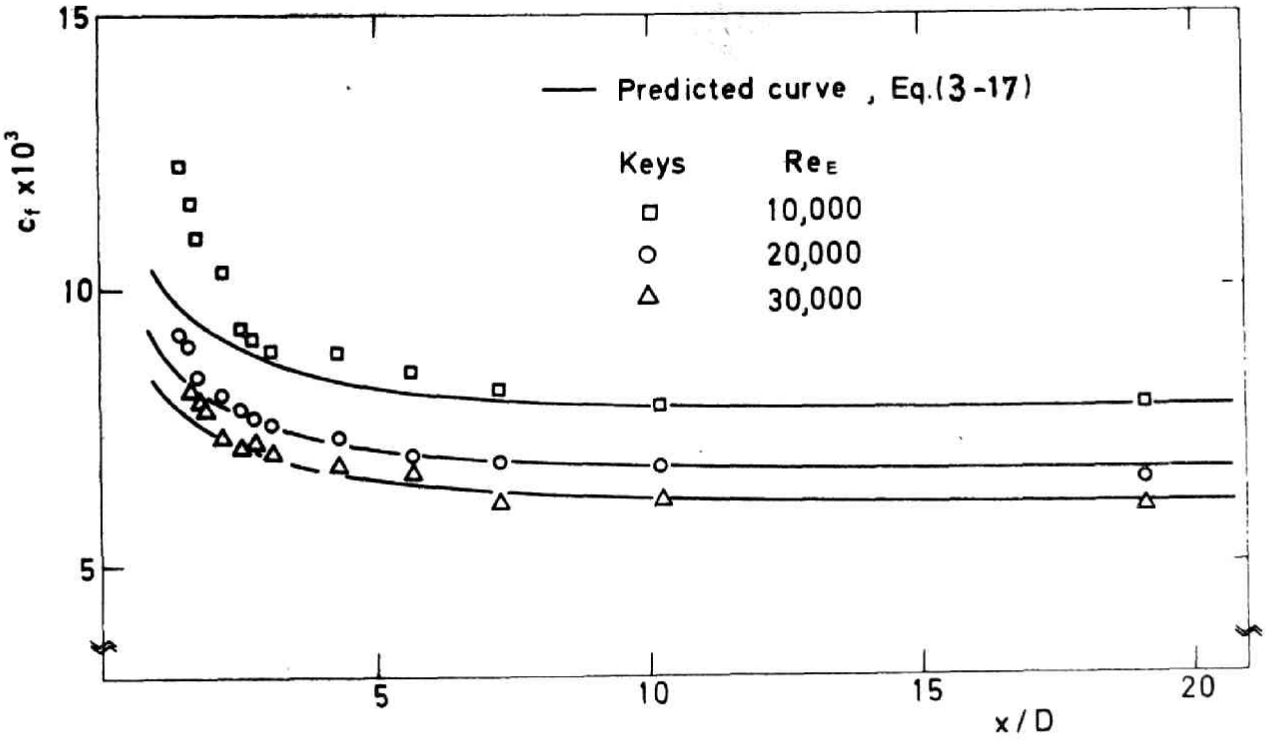

Fig.(3-10) Longitudinal distribution of skin friction factor in the entrance region of a circular tube.

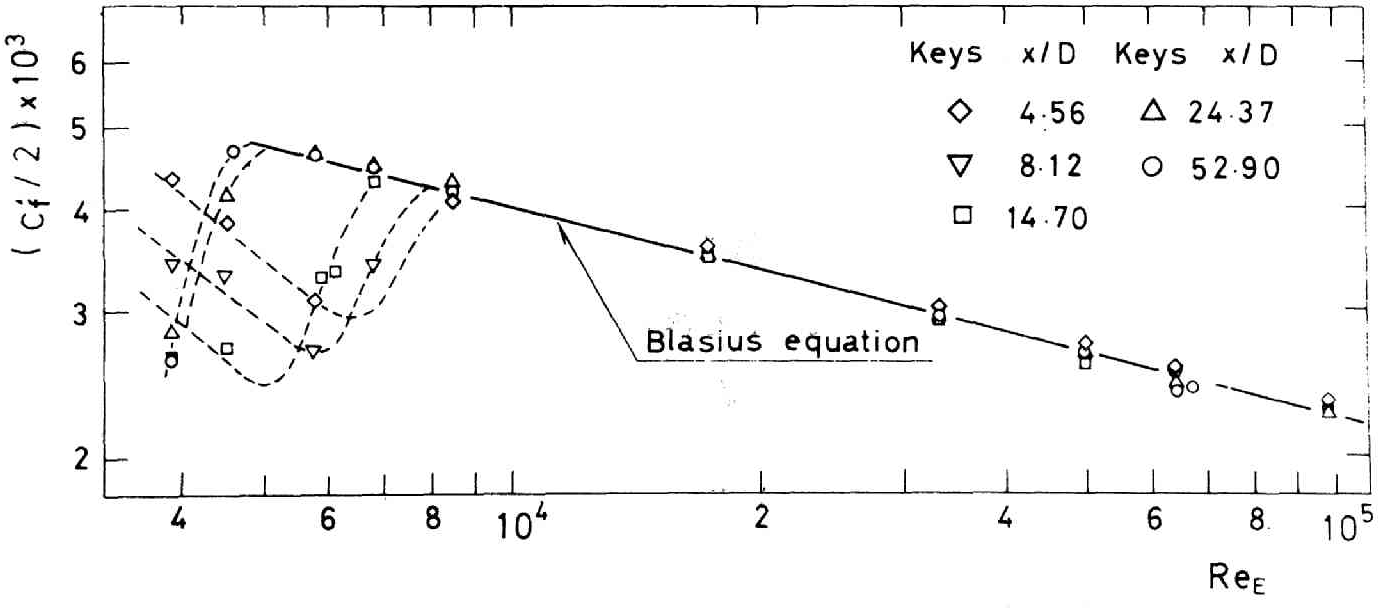

Fig.(3-11) Dependence of local skin friction factor on inlet Reynolds number.

stream direction quite soon.

For $Re_E > 10^4$, after approximately 15 pipe diameters downstream from the leading edge the friction factor reaches a constant value which is equal to that in the fully developed region. For $Re_E < 10^4$ there is observed a transition of the laminar boundary layer to the turbulent one even in the case with a trip wire. This is clearly seen in Fig.(3-11) in which the data are replotted as a function of Re_E with x/D as a parameter. Obviously the transition occurs at the location of smaller x/D when the Reynolds number increases.

3-6 Concluding remarks

The following results were obtained from the analytical and experimental investigation of the development of the turbulent boundary layer in the entrance region of a circular tube.

1: If there is no trip wire, at first a laminar boundary layer develops and then a turbulent boundary layer is achieved. The transition occurs in the same Reynolds number region as

that for a flat-plate boundary layer. The transition Reynolds number is approximately 6.2×10^5 and 7.7×10^5 and the length of the entrance region is 32.4 and 34.8 pipe diameters for $Re_E=5\times10^4$ and 1×10^5 respectively.

If there is a trip wire, the turbulent boundary layer develops from the leading edge. The length of the entrance region is 22.0 and 27.4 pipe diameters for $Re_E=5\times10^4$ and 1×10^5 respectively.

2: Availability of the electrochemical method for direct measurement of the skin friction was confirmed.

After approximately 15 pipe diameters downstream from the leading edge, the skin friction factor based on the inlet velocity reaches a constant value which is equal to that in the fully developed region.

3: Two prediction methods for the development of the turbulent boundary layer are presented. The method I is based on the similarity in the velocity distributions at any cross sections and on the one-parameter velocity profile. The another method II is based on the entrainment theory and on the two-parameter velocity profile. The difference between the results predicted by these methods is not distinguishable.

4: The theoretical results predicted by these two methods agree fairly well with the experimental results of the

growth of the boundary layer, the displacement and the momentum thicknesses. The theoretical results agree very well with the experimental results of the skin friction.

CHAPTER 4

MASS TRANSFER

4-1 Purpose

Heat and mass transfer between the tube wall and the turbulent stream in the entrance region of a circular tube is an important problem in chemical industries, for example, in heat exchangers and tube reactors. In this case a thermal or a concentration boundary layer develops in a turbulent boundary layer with small negative pressure gradients.

Experimental study was first carried out by Stanton (68). Later, Nusselt (49), Humble (27) and Aladyev (2) investigated experimentally the effect of the entrance condition on the heat transfer coefficient and presented empirical formulae

to correct for the effect of the entrance length. Their works are limited to the heat transfer at moderate Prandtl numbers.

The theoretical treatment of heat transfer in the entrance region has only been made by Deissler (7, 8). He assumed that the velocity and the temperature profiles in the fully developed turbulent flow may be applied also to the developing boundary layers in the entrance region. He used the momentum and the energy integral equations to predict the development of the hydrauric and the thermal boundary layer thicknesses. He obtained a fairly good agreement with the experimental results at moderate Prandtl numbers. These experimental and theoretical results seem to be useful for moderate Prandtl numbers. However, their application and extension to mass transfer at large Schmidt numbers is questionable because they do not account adequately for the transport of heat by eddy motion in the region close to the wall.

The purposes of the work covered in this chapter are:

1: To measure the turbulent mass transfer at large Schmidt numbers.

2: To provide a general method for predicting the local and the space-averaged heat and mass transfer rates in the large Plandtl or Schmidt number range.

4-2 Theoretical prediction

4-2-1 Differential equation

When the transport of mass from the tube wall to the turbulent stream occurs, the mass is transported by molecular diffusion and by eddy motion of the turbulent flow. The effect of turbulence on the rate of transport may be conveniently characterized in terms of an eddy diffusion coefficient (3).

In the turbulent mass transfer the concentration gradients in the direction perpendicular to the wall are usually much larger than that in the direction of flow because of the small liquid diffusion coefficient and the large Reynolds number.

In the case of turbulent mass transfer at large Schmidt numbers, the concentration changes occur in a region close to

the wall, so the curvature of the tube wall may be ignored. Making use of the eddy diffusion coefficient, and neglecting the diffusion in the flow direction and the curvature of the tube wall, one obtains the two dimensional equation of conservation of the diffusing species as

$$u\frac{\partial C}{\partial x} + v\frac{\partial C}{\partial y} = \frac{\partial}{\partial y}\left\{ (D + \varepsilon_D)\frac{\partial C}{\partial y} \right\} \qquad (4\text{-}1)$$

When the boundary layer is laminar, ε_D is zero. Falkner and Skan (12), and Hartree (19) obtained the exact solution of the boundary layer equation which gives similar velocity profile at different stations along the surface. With these results of the velocity distribution, they obtained a solution of the energy equation in the case of the uniform wall temperature. Lighthill (34) solved a problem of the laminar heat transfer, in which the velocity distribution is linear but its gradient at the tube wall (or the skin friction) changes along the flow direction. His solution is an excellent approximation in the case of large Prandtl numbers. The analysis which will be developed hereinafter is an extension of the Lighthill's procedure to the turbulent heat and mass transfer at large Schmidt numbers.

Introducing a new variable Ψ as

$$\frac{\partial \Psi}{\partial y} = u \ , \qquad - \frac{\partial \Psi}{\partial x} = v \qquad (4\text{-}2), (4\text{-}3)$$

, then one obtains the transformed equation

$$\frac{\partial C}{\partial x} = \frac{\partial}{\partial \Psi} \{ (D + \varepsilon_D) \, u \, \frac{\partial C}{\partial \Psi} \} \qquad (4\text{-}4)$$

where Ψ is the so-called "stream function". This procedure is known as the von Mises' transformation.

In the case of the turbulent boundary layers with small negative pressure gradients as exist in the entrance region of a circular tube, the effect of the pressure gradient on the velocity field is very small. As mentioned in Section 2-1-5, this effect may be neglected in the region close to the wall, i.e., in the laminar sublayer where the concentration changes occur. Therefore, the flow field in the laminar sublayer may be described by the law of the wall, i.e.,

$$u \ (x \ , \ y) = \frac{\tau_w(x)}{\mu} \, y \qquad (4\text{-}5)$$

where $\tau_w(x)$ is the skin friction at station x . Then one may describe the stream function as

$$\Psi = \int_0^y u dy = (\ \tau_w(x) \ / \ 2\mu \ ) \ y^2$$

and so

$$u = (2\tau_w(x)\ \Psi\ /\mu\ )^{1/2} \qquad (4\text{-}6)$$

Here, it is assumed that the distribution of ε_D for the fully developed tube flow may be applied to developing boundary layers as exist in the entrance region of a circular tube. The distribution for the fully developed tube flow has been investigated by Mizushina et al. (46), Lin et al. (36) and Son et al. (64). They have proposed several formulae for the distribution of ε_D in which the wall parameter y^+ is a single variable. In this analysis the following experimental formula which was obtained by Lin et al. from the mass transfer experiments at large Schmidt numbers, is used:

$$\varepsilon_D\ /\nu = (y^+\ /\ 14.5\ )^3 \qquad 0 \leqq y^+ \leqq 5 \qquad (4\text{-}7)$$

The wall parameter y^+ is related with the stream function as follows:

$$y^+ = yu^*\ /\nu = (\ 2\ /\nu\ )^{1/2}\ \ \Psi^{1/2} \qquad (4\text{-}8)$$

Introducing dimensionless variables and a dimensionless concentration as

$$\psi\ =\ \{y\ (\tau_w\ (x)\ /\rho\ )^{1/2}\ /\ \nu\}^2 = (\ y^+\ )^2 \qquad (4\text{-}9\text{-}a)$$

$$\xi\ =\ (\frac{4}{Sc})\ \frac{1}{\nu}\ \int_0^x\ (\frac{\tau_w(x)}{\rho})^{\frac{1}{2}}\ dx \qquad (4\text{-}9\text{-}b)$$

$$b = Sc / (14.5)^3 \qquad (4\text{-}9\text{-}c)$$

$$c = (C - C_b) / (C_w - C_b) \qquad (4\text{-}9\text{-}d)$$

and substituting Eqs. (4-6), (4-7) and (4-9-a, b, c, d) into Eq. (4-4), one may obtain the basic differential equation as

$$\frac{\partial c}{\partial \xi} = \frac{\partial}{\partial \psi} \{ (1 + b \psi^{\frac{3}{2}}) \psi^{\frac{1}{2}} \frac{\partial c}{\partial \psi} \} \qquad (4\text{-}10)$$

with initial and boundary conditions

$$\begin{array}{lllll} \text{I.C.} & c = 0 & \text{at} \quad \xi = 0 , & \psi \geq 0 & \\ \text{B.C.1} & c = 0 & \text{at} \quad \psi = \infty , & \xi \geq 0 & \\ \text{B.C.2} & c = f(\xi) & \text{at} \quad \psi = 0 , & \xi \geq 0 & \end{array} \qquad (4\text{-}11)$$

In the case of the uniform skin friction distribution this equation becomes the basic equation for mass transfer in the fully developed turbulent flow, where ξ corresponds to the familiar dimensionless coordinate $x^+ = \frac{xu^*}{\nu}$ multiplied by $4 / Sc$.

4.2.2 Solution

For simplicity Eq. (4-10) is rewritten as

$$\frac{\partial c}{\partial \xi} = \frac{\partial}{\partial \psi} \quad k(\psi) \frac{\partial c}{\partial \psi} \tag{4-10}$$

where

$$k(\psi) = (1 + b \psi^{\frac{3}{2}}) \psi^{\frac{1}{2}} \tag{4-12}$$

This equation is the same form as that for the conduction of heat where the heat conductivity is a function of position. However, in contrast with the heat conduction problem, the conductivity $k(\psi)$ becomes zero as ψ approaches to zero, so that the procedure used in the heat conduction theory gives a singular solution at $\psi \to 0$. The analytical procedure described hereafter is a modification of the method used in the heat conduction problems. This problem will be solved as an eigen-value problem.

Now, let the concentration profile be expressed by

$$c = \frac{4}{\pi} R \int_0^{\xi} ds \; f(s) \int_0^{\infty} e^{2i\beta^2 (\xi - s)} \Phi(\beta , \psi) \; \beta \; d \; \beta \tag{4-13}$$

where $R\,F(\xi)$ is the real part of a complex function $F(\xi)$

and Φ is a solution of the following ordinary differential equation:

$$\frac{d}{d\psi}\left(k(\psi) \frac{d\Phi}{d\psi} \right) - 2i\beta^2\Phi = 0 \qquad (4\text{-}14)$$

with boundary conditions

$$\Phi = 1 \quad \text{at} \quad \psi \to 0 , \quad \Phi = 0 \quad \text{at} \quad \psi \to \infty \qquad (4\text{-}15)$$

It is clear that the concentration profile expressed by this equation satisfies Eq. (4-10)' and the initial and boundary conditions (4-11). Equation (4-13) may be transformed into a Fredholm integral equation of the first kind by the introduction of a Green's function defined by

$$G(\psi , s) = \frac{1}{g} \int_0^s \frac{d\eta}{k(\eta)} \int_\psi^\infty \frac{d\eta}{k(\eta)} \qquad 0 \leq s \leq \psi \qquad (4\text{-}16\text{-a})$$

$$G(\psi , s) = \frac{1}{g} \int_0^\psi \frac{d\eta}{k(\eta)} \int_s^\infty \frac{d\eta}{k(\eta)} \qquad \psi \leq s \leq \infty \qquad (4\text{-}16\text{-b})$$

where

$$g = \int_0^\infty \frac{d\eta}{k(\eta)} \qquad (4\text{-}17)$$

Using the Green's theorem, one obtains the Fredholm integral equation for the unknown function $\Phi(\psi)$.

$$\Phi(\psi) = \frac{1}{g}\int_{\psi}^{\infty} \frac{d\eta}{k(\eta)} - 2\,i\beta^2 \int_{0}^{\infty} G(\psi,s)\,\Phi(s)\,ds \qquad (4\text{-}18)$$

Here, it must be noticed that

$$\frac{1}{g}\int_{\psi}^{\infty} \frac{d\eta}{k(\eta)} = \{k(\psi)\,\frac{\partial G}{\partial \psi}\}_{\psi=0} = \{k^*(\psi)\,\frac{\partial\ G}{\partial\ \psi^{1/2}}\}_{\psi=0} \qquad (4\text{-}19)$$

where $k^*(\psi)$ is $k(\psi)/2\psi^{1/2}$ and has a finite value at $\psi\to 0$. Introduction of $k^*(\psi)$ prevents the solution of Eq.(4-10) from becoming singular at $\psi\to 0$.

Now, introduce a homogeneous integral equation:

$$\Phi(\psi) = \lambda \int_{0}^{\infty} G(\psi,s)\,\Phi(s)\,ds \qquad (4\text{-}20)$$

Then, the Green's function may be expanded in terms of eigenvalues λ_n and eigen-functions $\phi_n(\psi)$ of Eq.(4-20) as follows:

$$G(\psi,s) = \sum_{n=1}^{\infty} \frac{\phi_n(\psi)\,\phi_n(s)}{\lambda_n} \qquad (4\text{-}21)$$

By combining Eqs.(4-19) and (4-21), one can transform the first term of the right hand side of Eq.(4-18) to

$$\frac{1}{g}\int_{\psi}^{\infty} \frac{d\eta}{k(\eta)} = \frac{1}{2}\sum_{n=1}^{\infty} \frac{\left.\frac{d\phi_n}{d\psi^{1/2}}\right|_{\psi=0}\,\phi_n(\psi)}{\lambda_n} \qquad (4\text{-}22)$$

Introducing Eqs.(4-20), (4-21) and (4-22) into the right hand side of the integral equation(4-18), one obtains finally a solution of Eq.(4-18) in an infinite series:

$$\Phi = \sum_{n=1}^{\infty} \frac{d\phi_n(\psi) \,/\, d\psi^{1/2}\big|_{\psi=0}\ \phi_n(\psi)}{2(\lambda_n + 2i\beta^2)} \tag{4-23}$$

Since the right hand side of Eq.(4-13) is evaluated as

$$R\int_0^{\infty} e^{i\beta^2(\xi-s)}\ \Phi(\beta,\psi)\beta d\beta$$

$$= \frac{\pi}{4} \sum_{n=1}^{\infty} e^{-\lambda_n(\xi-s)}\ \frac{1}{2}\left|\frac{d\phi_n}{d\psi^{1/2}}\right|_{\psi=0} \phi_n(\psi) \tag{4-24}$$

finally the concentration profile is given by the following equation:

$$c = \int_0^{\xi} ds\ f(s) \sum_{n=1}^{\infty} e^{-\lambda_n(\xi-s)} \frac{1}{2} \frac{d\phi_n}{d\psi^{1/2}}\bigg|_{\psi=0}\ \phi_n(\psi) \tag{4-25}$$

The local value of the dimensionless mass transfer coefficient K^+ is given by

$$K^+ = \frac{1}{2\ Sc}\int_0^{\infty} ds\ f(s) \sum_{n=1}^{\infty} e^{-\lambda_n(\xi-s)}\ \frac{d\phi_n}{d\psi^{1/2}}\bigg|_{\psi=0}^{2} \tag{4-26}$$

The method for calculating the eigen-values and eigen-functions numerically will be mentioned in Appendix 4-1. The validity

of this solution will be discussed in Appendix 4-2.

This solution includes the case with a step change in the wall concentration following an initial zero mass transfer region and the case with an arbitrary distribution of the wall concentration, $f(\xi)$, from the leading edge of the boundary layer.

In the case with an uniform wall concentration, i.e., $f(\xi)=1$, the concentration profile is given by

$$c = \sum_{n=1}^{\infty} \frac{1-e^{-\lambda_n \xi}}{\lambda_n} \frac{1}{2} \left| \frac{d\ \phi_n}{d\psi^{1/2}} \right|_{\psi=0} \phi_n(\psi) \tag{4-27}$$

and then the local mass transfer coefficient is

$$K^+ = \sum_{n=1}^{\infty} \frac{1-e^{-\lambda_n \xi}}{2\,Sc\lambda_n} \left| \frac{d\ \phi_n}{d\psi^{1/2}} \right|^2_{\psi=0} \tag{4-28}$$

The mass transfer averaged over Ξ with respect to ξ is calculated from Eq.(4-28) to

$$\langle K^+ \rangle = \frac{1}{\Xi} \int_0^{\Xi} K^+ \, d\xi = \frac{1}{2Sc} \sum_{n=1}^{\infty} \left\{ \frac{1}{\lambda_n} + \frac{1-e^{-\lambda_n \Xi}}{\lambda_n^2\ \Xi} \right\} \left| \frac{d\ \phi_n}{d\psi^{1/2}} \right|^2_{\psi=0} \tag{4-29}$$

This may be related to the space-averaged mass transfer coefficient as

$$\langle K^+ \rangle = \langle K \rangle / \langle u^* \rangle \tag{4-30}$$

Mass transfer in the short transfer section

(for small value of ξ)

For sufficiently short mass transfer section, the concentration boundary layer is so thin that the eddy diffusivity ε_D is small compared to the molecular diffusivity and may be neglected. Then, Eq.(4-10) becomes

$$\frac{\partial c}{\partial \xi} = \frac{\partial}{\partial \psi}\{\psi^{1/2} \frac{\partial c}{\partial \psi}\} \tag{4-31}$$

The solution of Eq.(4-31) is given by the so-called "Lévêque solution" which is

$$c = \frac{1}{\Gamma(4/3)} \int_0^{\eta} e^{-\eta^3} d\eta \tag{4-32}$$

where

$$\eta = \psi^{1/2} (4/9\xi)^{1/3} \tag{4-33}$$

The local and space-averaged mass transfer coefficients are given by the following equations:

$$K^+ = 0.3392 (\xi)^{-1/3} (Sc)^{-1} \tag{4-34}$$

$$\langle K^+ \rangle = 0.5088\ (\Xi)^{-1/3}\ (Sc)^{-1} \qquad (4\text{-}35)$$

Mass transfer in the well developed region

(for large value of ξ)

For very large values of ξ, the concentration profile becomes well developed and the concentration gradient in the ξ-direction may be neglected which is clearly shown by Eq.(4-27). Replacing the variable ψ by the ordinary wall parameter y^+ ($=\sqrt{\psi}$), one obtains the concentration profile as

$$c = 1 - \frac{\sin(\pi/3)3}{\pi}\left\{\frac{1}{6}\ln\frac{(y^+ + b^{-1/3})^3}{(y^+)^3 + b^{-1}}\right.$$

$$\left. + \frac{1}{\sqrt{3}}\left(\arctan\frac{2y^+ - b^{-1/3}}{\sqrt{3}\ b^{-1/3}} + \arctan\left(-\frac{1}{\sqrt{3}}\right)\right)\right\} \qquad (4\text{-}36)$$

and the mass transfer coefficients as

$$K^+ = \langle K^+ \rangle = \frac{3}{\pi}\, b^{1/3} \sin(\pi/3)\ Sc^{-2/3} \qquad (4\text{-}37)$$

4-3 Description of experiments

The flow system is the same as that mentioned in Section 2-2-2 and is shown in Fig.(4-1). The experiments were perform-

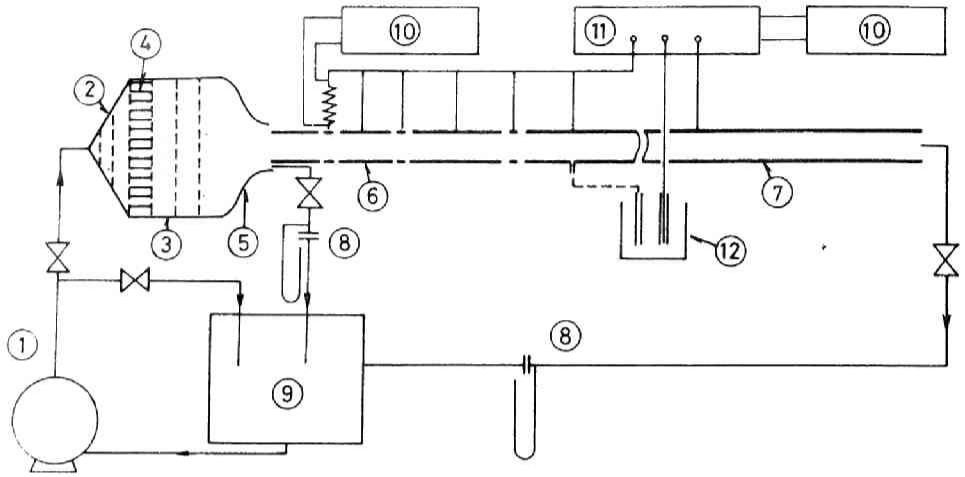

1	Pump	7	Anode
2	Divergent nozzle	8	Orifice meter
3	Calming section	9	Storage tank
4	Honeycomb	10	Recorder
5	Convergent nozzle	11	Potentiostat
6	Test section (cathode)	12	Standard electrode

Fig.(4-1) Schematic diagram of the experimental apparatus.

ed in the closed flow channel containing a test tube of which short sections of the wall were made of nickel cathodes. A nickel tube of much larger surface area than that of the test electrode was located downstream and was used as the anode. An electrolyte solution which contained small equimolar quantities(approximately 0.002 to 0.0004 mole) of ferro- and ferri-cyanide and 3 moles of potassium hydroxide as an indifferent electrolyte was circulated through the flow loop. The leading edge of the test tube was located at the outlet of the convergence nozzle where a flat velocity profile was obtained. The circular test tube, shown in Fig.(4-2) had 30 separate electrodes in the form of a ring of 3.80 cm I.D., ranging in length from 0.3 to 49.3 cm and isolated by 0.1 mm of epoxy resin. These rings were held together by supporting pipes of poly-vinylchloride. Shorter electrode sections were used for the measurements of the skin friction and the local mass transfer rate. The inner surface of the test electrodes was made smooth by sanding and polishing. A nickel trip wire of 1 mm in diameter was attached to the inner wall of the tube 2 mm downstream from the tube inlet and the first 3 mm from the tube inlet was coated with epoxy resin, so the mass transfer section begins 3 mm downstream from the inlet of the tube.

The electrode reaction carried out on the surface of the

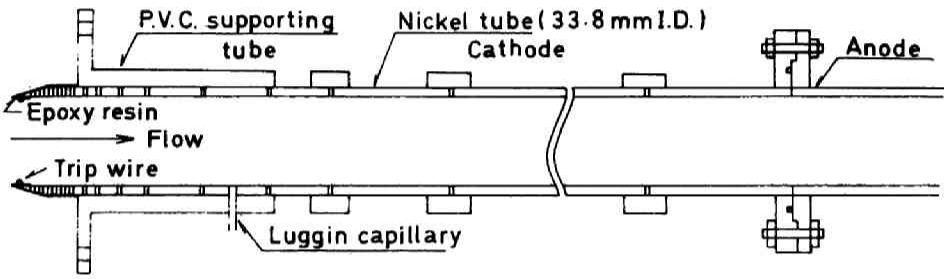

Fig.(4-2) Test section

Table 4-1 Physical properties of the electrolyte solution

		(at 30.0 degree C)
Density	1.127	(g/cm^3)
Viscosity	0.01107	(poise)
Diffusion coefficient for $Fe(CN)_6^{-3}$ ion	6.29×10^{-6} *	(cm^2/sec)
Schmidt number	1561	(-)

* This value was calculated by substitution of Hanratty's data(60) into Eisenberg's empirical formula(10);

$$D = 2.298\times10^{-10}\ (T/\mu)$$

where D should have the unit (cm^2/sec) and T (degree K) and μ (poise).

cathode was the reduction of ferri-cyanide ions under the diffusion controlling condition. The electric circuit is shown in Fig.(4-1). A negative potential relative to a Hg_2O standard electrode was applied to all the sections of the test electrode and was held at -100 mV by a potentiostat. In the measurement of the local rates of mass transfer, all sections of the cathode were active and the output signal at each section was recorded. The measurements were carried out at a Schmidt number of 1561 and inlet Reynolds numbers of 1×10^4, 2×10^4 and 3×10^4. The concentration of the ferri-cyanide ions in the electrolyte solution was determined by the standard iodometry. Physical properties of the electrolyte solution are tabulated in Table (4-1).

4-4 Experimental results and discussion

4-4-1 Local mass transfer coefficient

The distribution of the local rates of mass transfer was measured at a Schmidt number of 1561 and Reynolds numbers of 1×10^4, 2×10^4 and 3×10^4. In Fig.(4-3) the measured distributions of Stanton number are plotted as a function of x/D from the front edge of the mass transfer section which is located

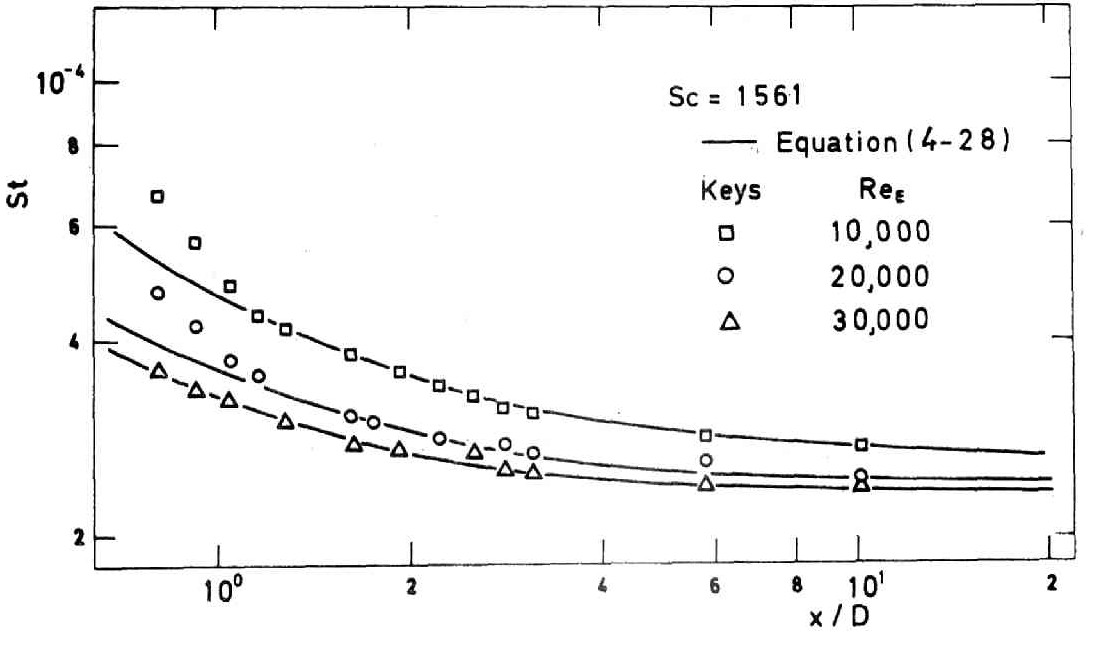

Fig.(4-3) Variation of local Stanton number with x/D.

at 3 mm downstream from the tube inlet.

In order to compare the experimental results with the analytical theory, the dimensionless streamwise distance ξ was calculated numerically from the measured distribution of the skin friction factor(see in Fig.(3-12)) and was plotted in Fig.(4-4). By use of this diagram the experimental results of the local mass transfer coefficients are replotted in Fig.(4-5) in the form of K^+ $(=K/u^*)$ against dimensionless distance ξ. The predicted curve calculated from Eq.(4-28) is also shown in the same diagram. All the measurements are represented satisfactorily by this type of correlation in which the Reynolds number does not appear as a parameter.

By means of the method I and II presented in Sections 3-2 and 3-3, the variations of the friction velocity and the dimensionless distance ξ with x/D can be predicted analytically. With these results and with the relation between K^+ and ξ, the local mass transfer coefficient or Stanton number can be predicted. The results are plotted in Fig.(4-3). The predicted curves agree closely well with the experimental results. The agreement suggests that the rates of mass transfer can be predicted by the combination of the method I (or II) and the analytical relation between K^+ and ξ.

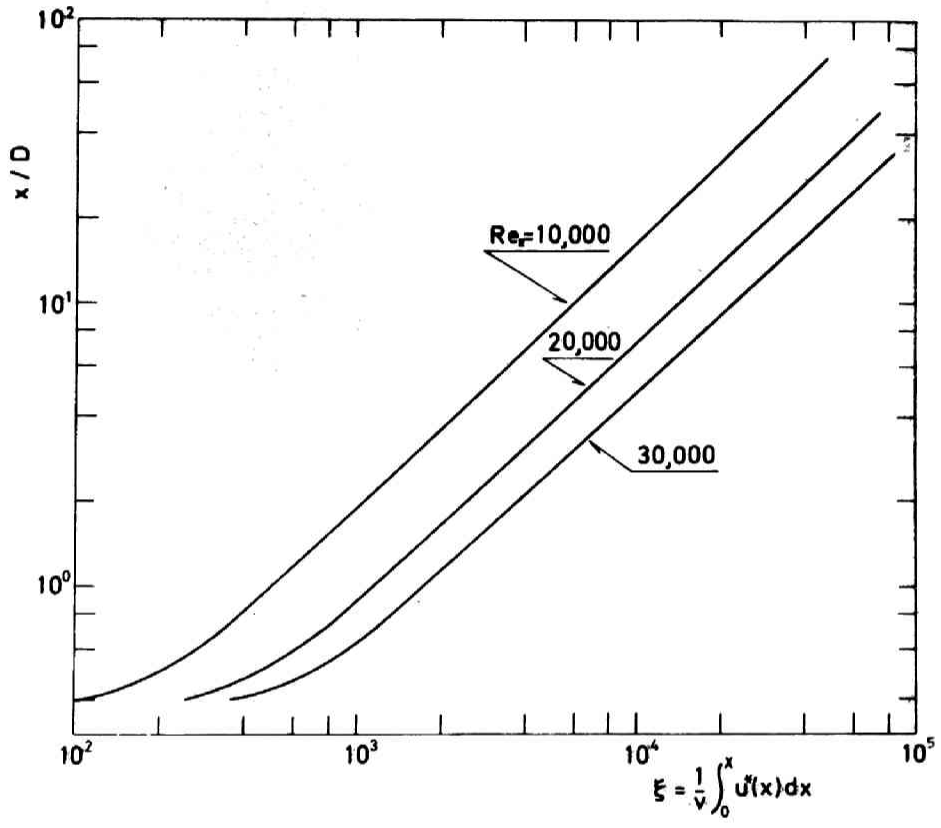

Fig.(4-4) Variation of dimensionless distance ξ with x/D.

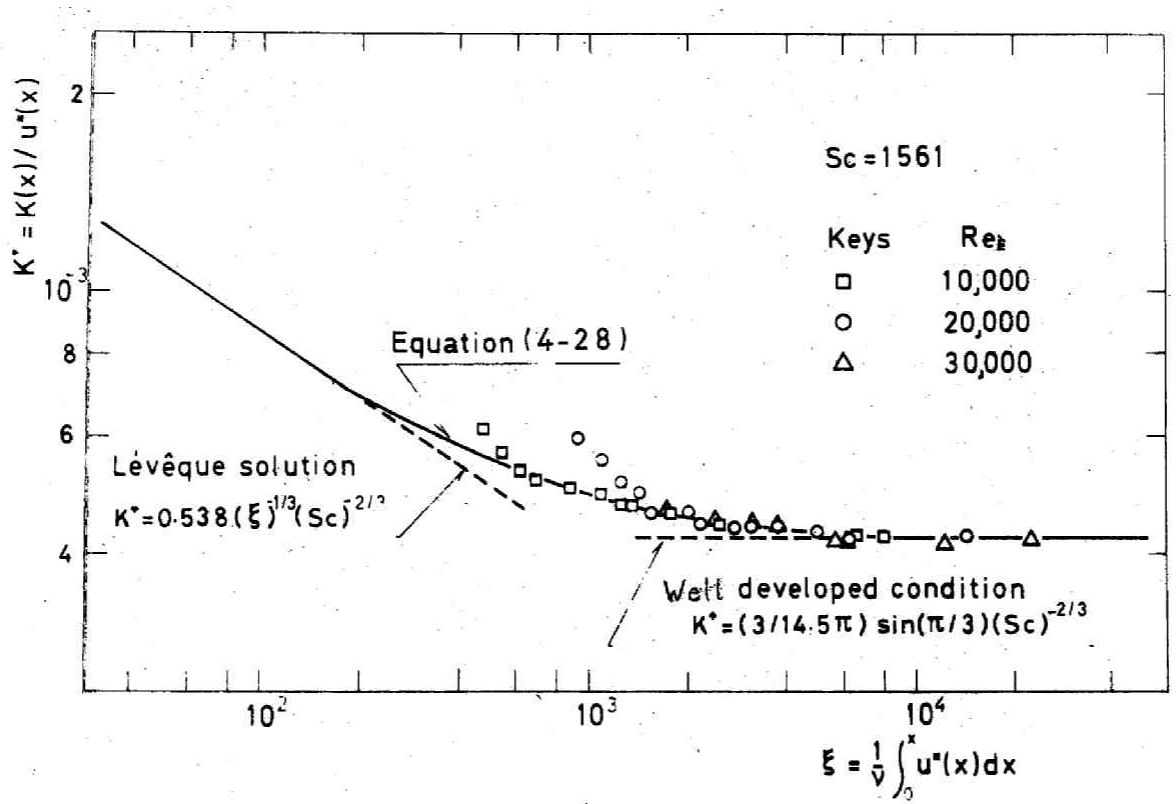

Fig.(4-5) Variation of local mass transfer coefficient K^+ with ξ.

The well developed concentration profile is attained at the location at which K^+ becomes constant. The length from the leading edge to that location is refered to as the entrance length for mass transfer. This length is $\Xi = 8000$ for the Schmidt number of 1561. For Reynolds numbers of 3×10^4, 2×10^4 and 1×10^4, the location of $\xi = 8000$ corresponds to $x/D = 3.95$, 5.96 and 12.7 respectively at which the skin friction is still changing in the flow direction. Therefore, the local mass transfer coefficient is also changing. The local mass transfer coefficient becomes constant at the distance of about 15 pipe diameters from the leading edge, at which the skin friction just becomes constant. This is a characteristic feature of mass transfer at large Schmidt numbers in the entrance region of a circular tube.

In Fig.(4-4) and (4-5), the experimental results with the small value of ξ, that is, near the leading edge of the test tube show the poor agreement with the predicted curve of Eq.(4-28). The reason is that disturbances produced by the trip wire cause a considerable change in the velocity profile. Since these disturbances are soon obliterated further downstream, the good agreement is obtained at the larger value of ξ.

4-4-2 Space-averaged mass transfer coefficient

In Fig.(4-6) the space-averaged mass transfer coefficients are plotted in the form of $\langle K^+ \rangle$ against Ξ. The rigid line represents the predicted curve which is obtained by integration of Eq.(4-28). The agreement between the predicted curve and the experimental results is clearly indicated.

The agreement of the experimental values of the local and the space-averaged mass transfer coefficient with Eqs.(4-28) and (4-29) verifies the assumption that the distribution of the eddy diffusivity is a function of ψ alone and is represented by Eq.(4-7) which is attained in the fully developed tube flow. Therefore, it may be concluded that the distribution of the eddy diffusivity of mass is not dependent on the longitudinal pressure gradient as exists in the entrance region of a circular tube and that the distribution of the eddy diffusivity for the fully developed tube flow may apply to the developing boundary layer with small negative pressure gradients.

Since the eddy diffusivity distribition described by Eq.(4-7) is applicable only to the region $0 \leq y^+ \leq 5$, The calculated results might not be correct for smaller Schmidt numbers, because the thickness of the concentration boundary layer in this case may become larger than $y^+=5$.

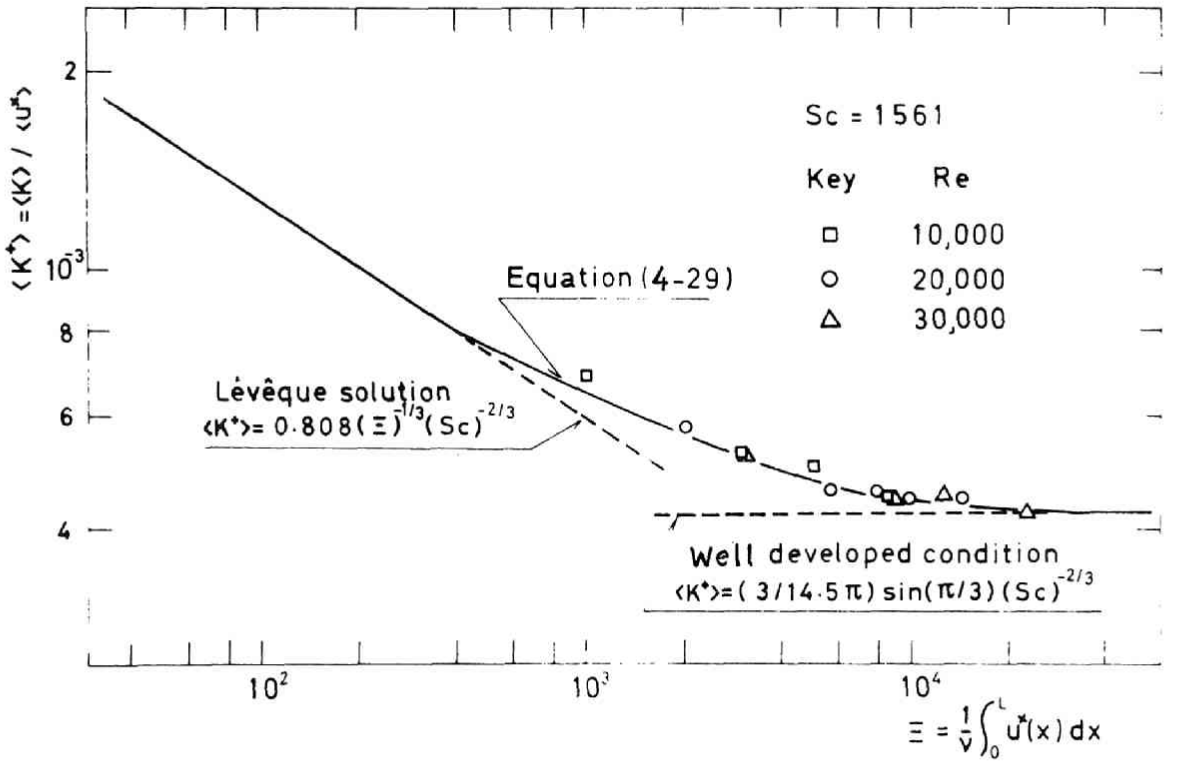

Fig.(4-6) Variation of space-averaged mass transfer coefficient $\langle K^+ \rangle$ with Ξ.

After all, the theoretical analysis given in Section 4-3 predicts satisfactorily the variations of both the local and the space-averaged values of dimentionless heat and mass transfer coefficients, K^+ and $\langle K^+ \rangle$, with ξ. The relation of K^+ vs. ξ and that of $\langle K^+ \rangle$ vs. Ξ are dependent only on the Prandtl or the Schmidt number and are available universally, i.e., for fully developed tube flow and turbulent boundary layer flow with and without pressure gradients and flows in convergent and divergent nozzles with small opening angles. For the several Prandtl or Schmidt numbers these relations are shown in Figs. (4-7) and (4-8). For turbulent flow with arbitrary distribution of the skin friction, the value of ξ must be calculated by analytical or experimental results of the skin friction and then the relations of K^+ vs. ξ and $\langle K^+ \rangle$ vs. Ξ are used to predict the local and the space-averaged rates of heat and mass transfer.

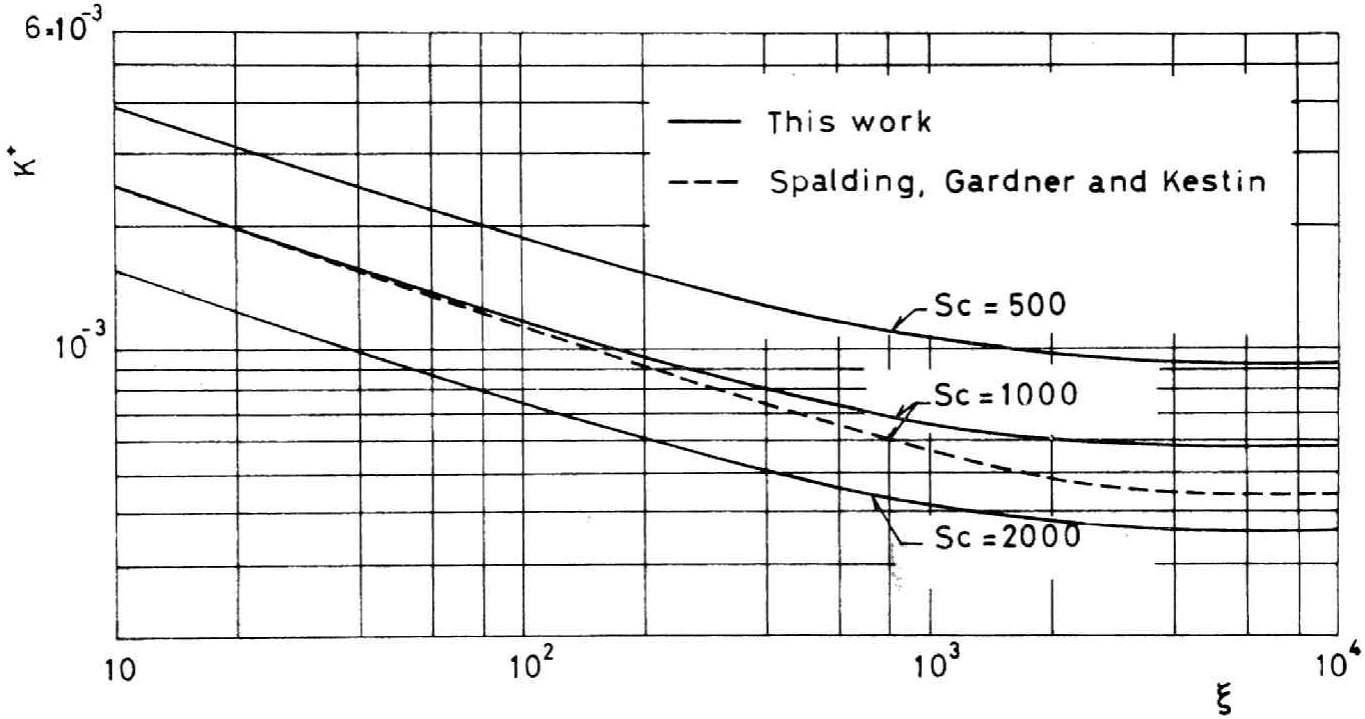

Fig.(4-7) Variation of local mass transfer coefficient K^+ with Schmidt number and ξ.

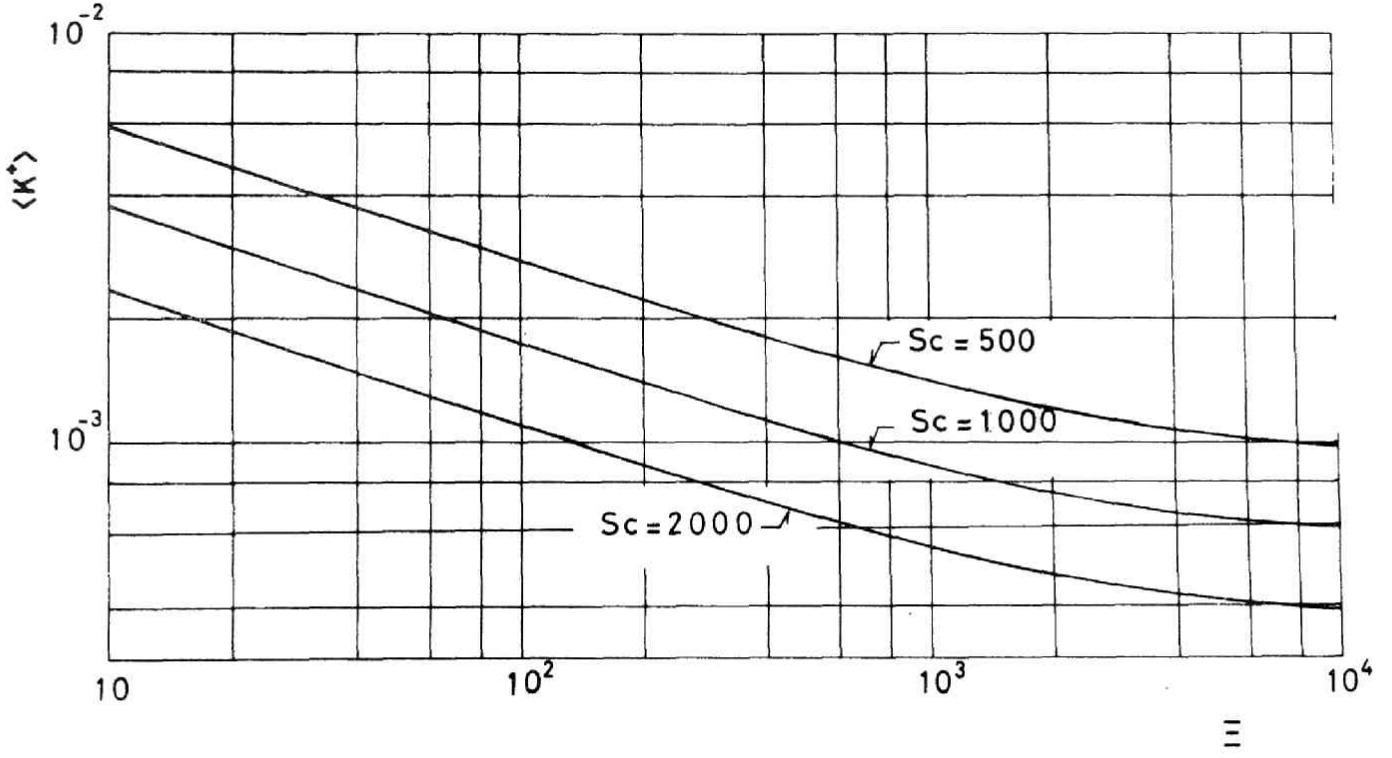

Fig.(4-8) Variation of space-averaged mass transfer coefficient $\langle K^+ \rangle$ with Schmidt number and Ξ.

4-4-3 Comparison with previous works

Experiments of the turbulent heat transfer at moderate Prandtl numbers were made by many investigators. However, few general correlations showing the effect of the entrance condition on the heat transfer coefficient exist. Stanton(69) showed that the space-averaged heat transfer coefficients are attained at a constant value at the cross section of x/D=30. Later on, Nusselt(50) studied the effect of entrance length and recommended introducing the correction factor $(L/D)^{-0.054}$, so that the resultant equation for the heat transfer coefficient becomes

$$\frac{<h>D}{\lambda} = 0.036\ Re_E^{0.8}\ Pr^{1/3}\ (L/D)^{-0.054} \quad \text{for } 10<L/D<400 \tag{4-38}$$

The local heat transfer coefficients were measured by Aladyev(2). In Fig.(4-9) some of his results are shown. His results indicate that the local heat transfer coefficient remains constant at $x/D \geq 40$ and the space-averaged coefficient is constant at $L/D \geq 50$ and that the distribution of the transfer coefficients depend on Re_E as well as on x/D (or L/D). In the same diagram the results of this work are also plotted. It is clearly shown that the correction factor is also dependent on the Schmidt number (or Prandtl number) and that at larger Schmidt numbers the mass transfer coefficient becomes

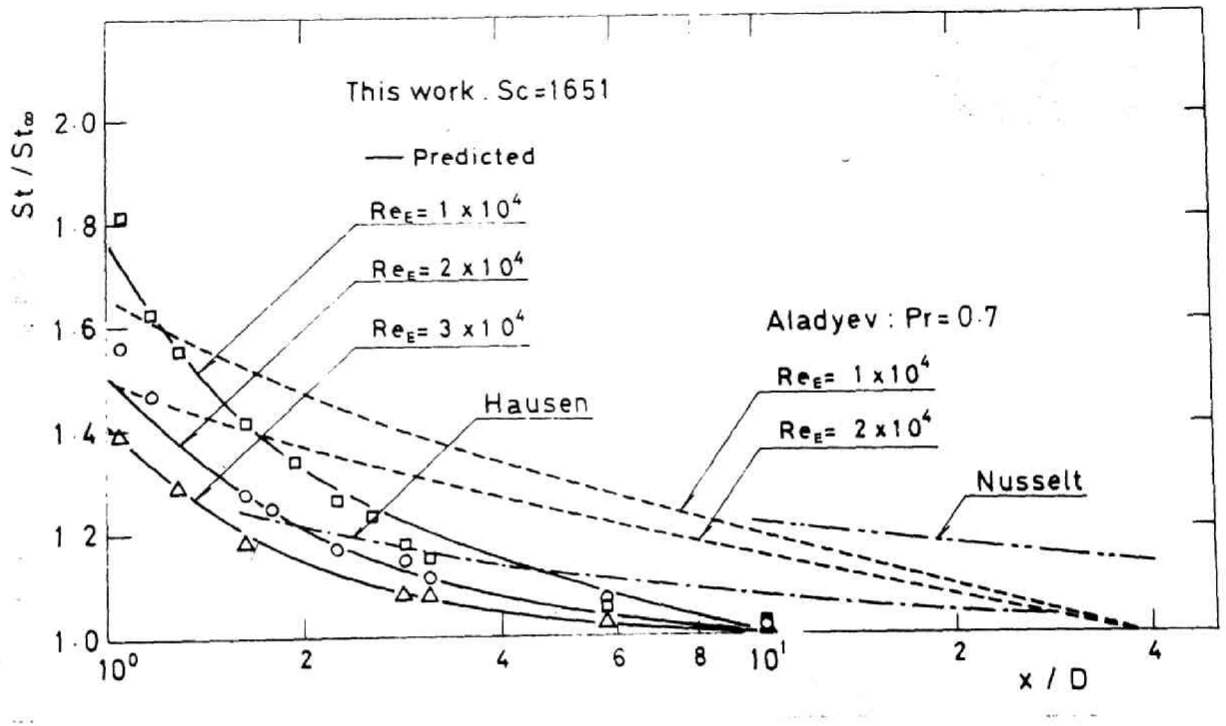

Fig.(4-9) Comparison of experimental Stanton number for various Schmidt numbers and Reynolds numbers.

the well developed value in a shorter entrance section. At sufficiently large Schmidt numbers the length of the entrance section becomes constant that is $x/D \simeq 15$.

4-5 Concluding remarks

The following results were obtained from the analytical and experimental investigation of the turbulent mass transfer at large Schmidt numbers in the entrance region of a circular tube.

1: If the distribution of the eddy diffusivity is assumed to be a function of y^+ alone, the equation of conservation of matter may be simplified by introducing new valiables ψ and ξ. The transformed equation may be reduced into the form of integral equation which is solved easily as an eigen-value problem.

2: The agreement between the experimental results and the analytical ones confirms that the distribution of the eddy diffusivity of mass is not dependent on the longitudinal pressure gradient as exists in the entrance region of a cir-

cular tube and that the distribution of the eddy diffusivity for the fully developed tube flow may apply to the developing boundary layer with small negative pressure gradients.

3: At large Schmidt numbers the local mass transfer coefficient K becomes constant at the distance of about 15 pipe diameters from the leading edge, at which the skin friction just becomes constant, since the dimensionless mass transfer coefficient K^+ $(=K/\sqrt{\tau_w/\rho}\,)$ have been already constant upstream from that location.

Appendix 4-1 Numerical calculation

The homogeneous integral equation is

$$\phi(\psi) = \lambda \int_0^\infty G(\psi,s)\ \phi(s)\ ds \qquad (4\text{-}20)$$

with the boundary conditions

$$\begin{aligned} &\phi = 1 \qquad \text{at } \psi = 0 \\ &\phi = 0 \qquad \text{at } \psi \to \infty \end{aligned} \qquad (4\text{-}39)$$

For numerical calculation the second boundary condition $\psi \to \infty$ is replaced by $\psi = h$ where h is a sufficiently large value in comparison with the concentration boundary layer thickness. For simplicity the Green's function is written as follows

$$G(\psi,s) = G^{(1)} \qquad 0 \leq s \leq \psi$$
$$= G^{(2)} \qquad \psi \leq s \leq h$$

If one splits the interval (0,h) into m of parts, the integral equation (4-20) becomes

$$\frac{\phi_i}{\lambda} = \int_0^{\frac{i}{m}h} G^{(1)}(\tfrac{i}{m}h,s)\phi(s)ds + \int_{\frac{i}{m}h}^{h} G^{(2)}(\tfrac{i}{m}h,s)\phi(s)ds \qquad (4\text{-}40)$$

In accordance with Hidaka's method(21), the integral may be replaced by Newton-Cotes approximate method and then one obtains

$$\frac{\phi_i}{\lambda} = \frac{i}{m}h \sum_{j=0}^{i} R_j^{(i+1)} G_{ij}^{(1)} \phi_j + \frac{m-i}{m}h \sum_{j=i}^{m} R_j^{(m-i-1)} G_{ij}^{(2)} \phi_j \qquad (4\text{-}41)$$

where $R_j^{(i)}$ is a weighting coefficient of the Newton-Cotes mean-value method. For $i \geq 2$ or $m-i \geq 2$, a combination of the Simpson's 1/3 rule and the Simpson's 3/8 rule may be used. For i=1 and i=m-1, one may rewrite the integral in the following way:

$$\int_0^{\frac{1}{m}h} = \int_0^{\frac{3}{m}h} - \int_{\frac{1}{m}h}^{\frac{3}{m}h}$$

Then one may also apply the Simpson's 3/8 rule for the first term of the right hand side and the Simpson's 1/3 rule for the second term.

The application of this procedure for each i results in a set of m+1 homogeneous simultaneous equations which has m+2 unknowns. The set of equations written in a matrix form is

$$\begin{vmatrix} A_{11}-\frac{1}{\lambda}, A_{12}, & & A_{1,m+1} \\ A_{21} & A_{22}-\frac{1}{\lambda}, & \\ & & \\ A_{m+1,1}, & & A_{m+1,m+1}-\frac{1}{\lambda} \end{vmatrix} \begin{vmatrix} \phi_1 \\ \phi_2 \\ \cdot \\ \phi_{m+1} \end{vmatrix} = \begin{vmatrix} 0 \\ 0 \\ \cdot \\ 0 \end{vmatrix} \qquad (4\text{-}42)$$

The matrix A must always be zero. Otherwise, the solution of ϕ must always have zero value. The requirement of $A \equiv 0$ gives the eigen-values λ_i which are real. Substituting λ_i into Eq. (4-42), one finally obtains the values of the eigen-function $\phi_i(jh/m)$ for the locations of $j=1,\cdots, m+1$. One may perform the calculation of the eigen-values and the eigen-functions by the Danielevsky method by use of a digital computer.

Since the derivative of the Green's function $G(\psi,s)$ with respect to $\psi^{1/2}$ is

$$\frac{\partial G(\psi,s)}{\partial \psi^{1/2}} = \frac{2}{g}\int_s^h \frac{d\eta}{k(\eta)}$$

, the derivative of ϕ_n at $\psi=0$ is obtained by numerical integration of the following equation

$$\left.\frac{\partial \phi_n}{\partial \psi^{1/2}}\right|_{\psi=0} = \frac{2\lambda_n}{g}\int_0^h ds\ \phi_n(s)\int_0^s \frac{d\eta}{k(\eta)} \qquad (4\text{-}43)$$

Appendix 4-2 Validity of Equation (4-25)

The concentration profile is given by Eq.(4-25)

$$c = \int_0^\xi ds\ f(s)\sum_{n=1}^{\infty} e^{-\lambda_n(\xi-s)}\left.\frac{d\phi_n(\psi)}{2\,d\psi^{1/2}}\right|_{\psi=0}\phi_n(\psi) \qquad (4\text{-}13)$$

Now it will be verified that this solution satisfies the partial differential equation (4-10) with the initial and the boundary conditions, Eq. (4-11).

Now let

$$B = \int_0^h G(\psi,s)\, c(s,\xi)\, ds =$$

$$= \int_0^{\xi} ds\, f(s) \sum_{n=1}^{\infty} e^{-\lambda_n(\xi-s)} \frac{d\phi_n/d\psi^{1/2}\big|_{\psi=0}\ \phi_n(\psi)}{2\lambda_n} \qquad (4\text{-}44)$$

The partial derivative of B with respect to ξ gives

$$\int_0^h G(\psi,s)\, \frac{\partial c}{\partial \xi}\, ds = -c + f(\xi)\, \frac{1}{g} \int_{\psi}^h \frac{d\eta}{k(\eta)} \qquad (4\text{-}45)$$

On the other hand, the partial derivative of B with respect to s gives

$$\int_0^h G(\psi,s) \frac{\partial}{\partial s}\{k(s)\frac{\partial c}{\partial s}\}ds = \frac{1}{g} \int_{\psi}^h \frac{d\eta}{k(\eta)}\, c(0,\xi) - \frac{1}{g} \int_0^{\psi} \frac{d\eta}{k(\eta)}\, c(h,\xi) - c(\psi,\xi) \qquad (4\text{-}46)$$

Combining Eqs.(4-45) and (4-46), one obtains

$$\int_0^h G(\psi,s)\{\frac{\partial c}{\partial \xi} - \frac{\partial}{\partial s}(k(s)\frac{\partial c}{\partial s})\}\ ds = \{f(\xi) - c(0,\xi)\}\, \frac{1}{g} \int_{\psi}^h \frac{d\eta}{k(\eta)} + c(h,\xi)\frac{1}{g} \int_0^{\psi} \frac{d\eta}{k(\eta)} \qquad (4\text{-}47)$$

Substitutions of $\psi=0$ and $\psi=h$ into Eq.(4-47) give

$$c(0,\xi) = f(\xi) \qquad \text{and} \qquad c(h,\xi) = 0$$

Since all the terms of the right hand side of Eq.(4-47) were shown to be zero, the left one must be always zero for arbitrary values of ψ. This results in

$$\frac{\partial c}{\partial \xi} = \frac{\partial}{\partial \psi}\{ k(\psi) \frac{\partial c}{\partial \psi} \}$$

PART II

TRANSPORT PHENOMENA

AROUND A CIRCULAR CYLINDER IN CROSS FLOW

CHAPTER 5

EFFECT OF FREE-STREAM TURBULENCE

ON MASS TRANSFER FROM A CIRCULAR CYLINDER IN CROSS FLOW

5-1 Introduction

In Part I the transport phenomena in tube flow were discussed. The another important problem for numerous engineering applications is concerned in the transport phenomena from a body in cross flow. For this reason, and also because a circular cylinder has a convenient shape with which to work, this study was initiated. There have been many experimental and theoretical studies. However, the experimental results on the rates of heat and mass transfer reported by different investigators show divergence which exceeds the respective experimental errors. These discrepancies can be explained by

the effect which free-stream turbulence has on the rate of heat and mass transfer.

The free-stream turbulence increases heat and mass transfer from a circular cylinder in cross flow. Recently a few experimental results concerning to this effect have been reported. However, these works have been done in air flow ($Pr \simeq 0.7$) and little have been done with liquids ($Pr \simeq 6$). Furthermore, these data have been obtained for the space-averaged heat transfer coefficient only. For liquids at large Prandtl or Schmidt numbers, there have been no investigation.

5-1-1 Previous works

It has been known for long time that heat transfer from a body in cross flow increases when the free-stream turbulence intensity increases, and recently a few experimental results concerning to this effect have been reported, particularly for space-averaged heat transfer at moderate Prandtl numbers.

The first quantitative investigation was carried out by Comings et al.(81) who measured the influence of turbulence on the space-averaged heat transfer coefficient in the subcritical

Reynolds number range from 400 to 20,000. They found that if the Reynolds number is high enough, the heat transfer coefficient is increasing with the turbulence intensity at low turbulence intensities, tending toward a definite value at higher turbulence intensities, and that such an effect is negligible at smaller Reynolds numbers. The effects of turbulence are divided into an increase in the local heat transfer rate, an earlier transition to turbulent boundary layer, a movement of the separation point and a change of flow mechanism in the separated region. Giedt(14) measured the local skin friction and the local rate of heat transfer in the ranges of near-critical and supercritical Reynolds number, and found a very important fact that the distribution of the skin friction factor around the front portion of the cylinder remained virtually unaffected by a considerable increase in free-stream turbulence intensity. Kestin and Maeder(28) made an extensive discussion on this problem and reported experimental results on the effect of screen-produced turbulence on the space-averaged coefficient of heat transfer from a cylinder in air stream in near-critical Reynolds number range. These results demonstrate that the heat transfer rate is increased substantially by the slight increases in turbulence intensity, and that it becomes almost constant with further increases in turbulence intensity.

5-1-2 Purpose and outline

The purpose of the work covered in Part II is an experimental presentation of the effects of screen-produced turbulence on the local and the space-averaged mass transfer coefficients at large Schmidt numbers.

1: For the presentation of the effect of turbulence on the space-averaged mass transfer coefficient the measurements were made in subcritical Reynolds number range from 3870 to 10,380 and at free-stream turbulence of 0.8, 1.2 and 2.3 % at a Schmidt number of 1230. The investigation was carried out at large Schmidt number range. For this reason the analogy between heat transfer at moderate Prandtl number and mass transfer at large Schmidt numbers is examined and then the effect of turbulence on the space-averaged mass transfer coefficient is discussed.

2: For the presentation of the effect of turbulence on the local mass transfer rate, we must know the local values of mass transfer coefficient for zero turbulence, which may be obtained by the solution of mass transfer equation as well as by the solution of laminar boundary layer equation. The solutions can be obtained at the front portion of the cylinder at which a laminar boundary layer exists so that the

discussion is limited to that portion.

The boundary layer equation was solved by use of the measured distribution of the static pressure around the cylinder. For solving this problem three approximate methods were used. On the other hand the measurements of the local mass transfer rates were carried out. The measured distributions were compared with that for zero turbulence intensity and the effect of turbulence on local mass transfer was discussed.

3: In addition, the location of the separation point were determined experimentally at $Re=10^4$ and the effect of turbulence on the location of the separation point was discussed.

The measurements of the local and the space-averaged mass transfer coefficients and of the location of the separation point were carried out by use of the electrochemical method which was explained in detail in Section 1-3. The measurements of free-stream turbulence intensity were also performed by the electrochemical method described in Section 2-2.

5-2 Experimental apparatus and procedure

The experimental apparatus is shown schematically in Fig. (5-1). To make the velocity profile as flat as possible, five screens were installed in series in the channel upstream from the test cylinder. Turbulence intensities were varied as 0.8, 1.2 and 2.3 % by changing the screens located 21 cm upstream from the test cylinder. A test cylinder of 1 cm diameter was mounted horizontally in a channel of 8×16 cm cross section, and its axis being perpendicular to the free stream. The flow system, i.e., the water tunnel and the pump were made of polyvinylchloride plastic. Two types of test cylinder having diameter of 1 cm were used and shown in Figs.(5-2-a) and (5-2-b). The one for pressure distribution measurement had a static pressure tap of 0.5 mm diameter. The second for mass transfer measurement had a platinum cathode of 0.5 mm diameter, which was embedded in but isolated electrically from the main cathode around the middle part of the cylinder surface in width of 2 cm. Both the isolated cathode and the main cathode were active during the measurement. The cylinder can be rotated , so as to make the position of the pressure tap or the isolated cathode relative to the front stagnation point vary. The anode, which was a large nickel plate of 20×10 cm, was located downstream.

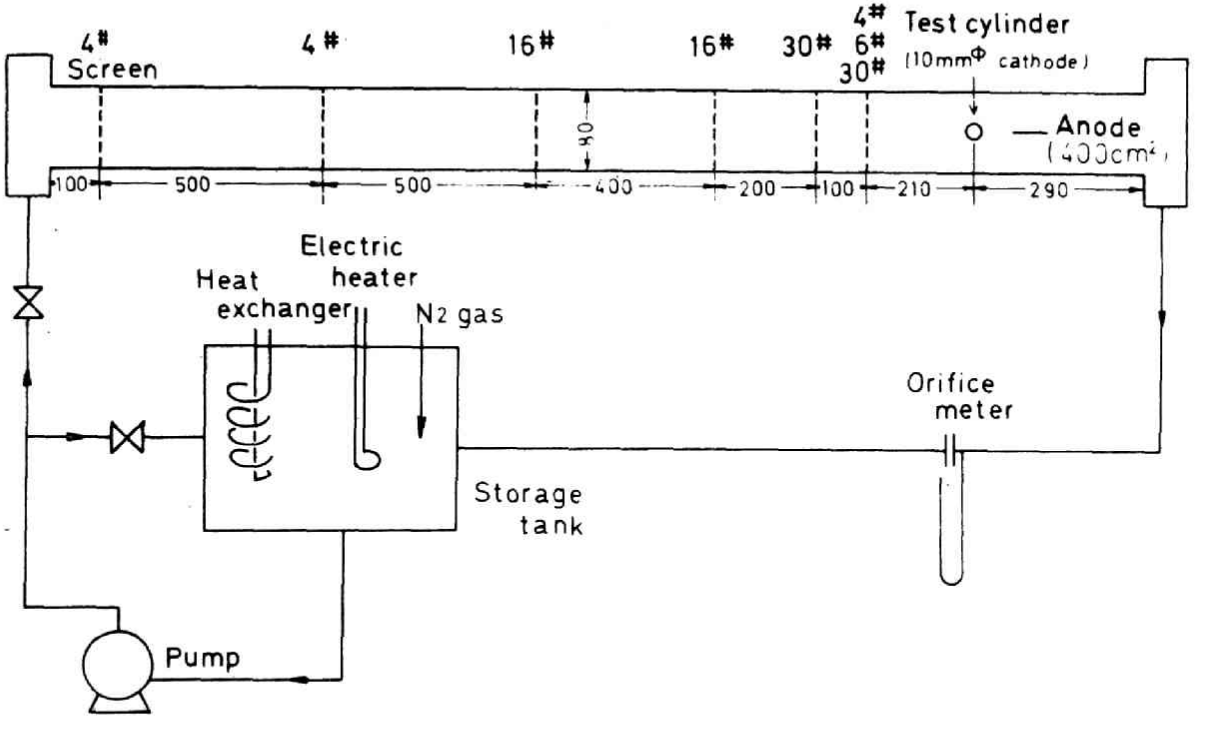

Fig.(5-1) Schematic diagram of the experimental apparatus.

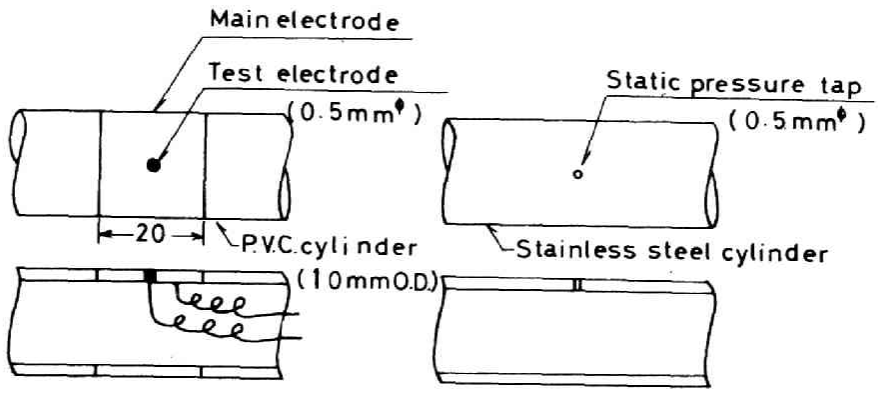

(a) for mass transfer (b) for static pressure

Fig.(5-2) Test cylinder.

The electrochemical reaction, which was carried out on the surface of the test cylinder was reduction of ferri-cyanide. The circulating solution contained 0.01 mole of $K_3Fe(CN)_6$ and $K_4Fe(CN)_6$ respectively and 1 mole of NaOH per liter, and was kept at 30.00±0.05 deg C. Then, the Schmidt number was 1230.

5-3 Space-averaged mass transfer coefficient

In Fig.(5-3), results of the space-averaged mass transfer coefficient are plotted in the form of j-factor as a function of Reynolds number. The Reynolds number is based on the free stream velocity corrected for solid-blocking and for wake-blocking after Pope's method(82), which gives 1.029 as the correction factor for the free stream velocity. The results obtained by other investigators are also plotted in Fig.(5-3). Among these, Grassmann's data(48) were obtained from the mass transfer measurements by means of the electrochemical method.

In this work the space-averaged mass transfer coefficients were obtained with three levels of free-stream turbulence intensity, i.e., 0.8, 1.2 and 2.3 %. The data for turbulence inten-

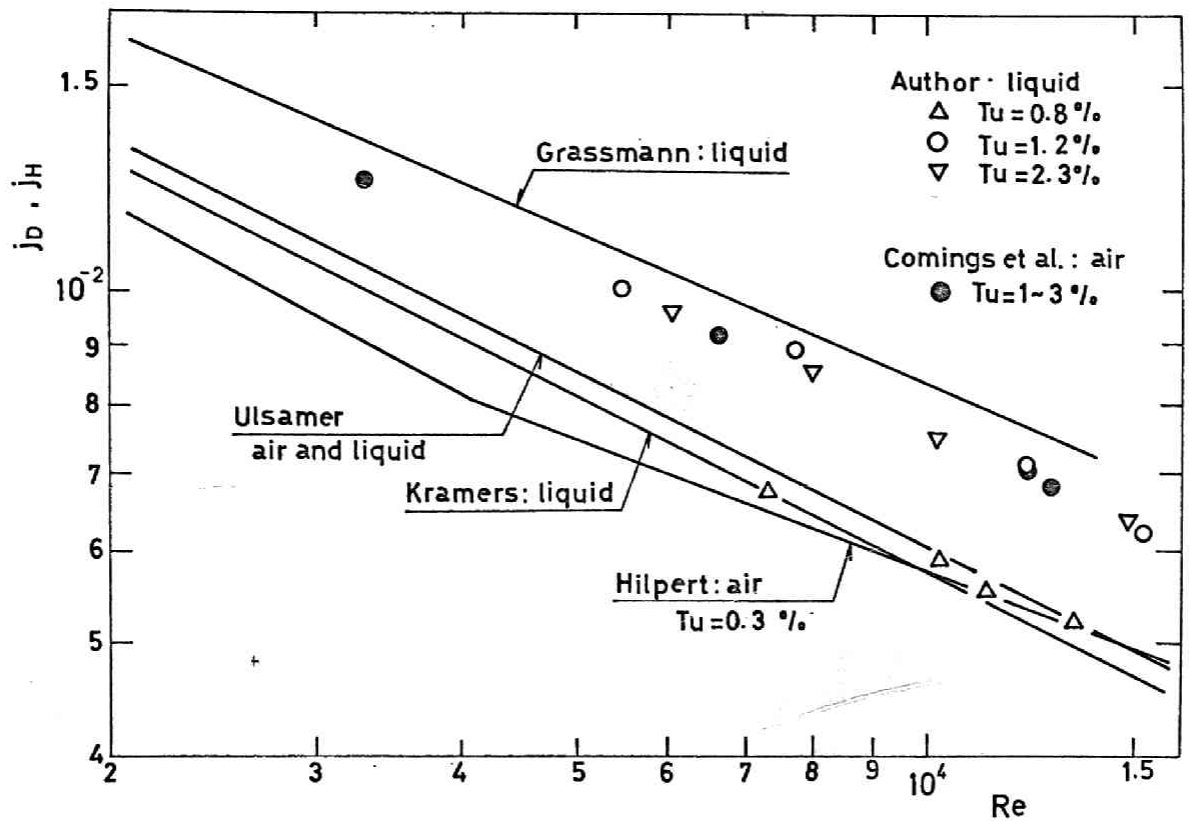

Fig.(5-3) Space-averaged heat and mass transfer coefficient around a circular cylinder in cross flow.

sities of 1.2 and 2.3 % are in good agreement with the heat transfer data obtained by Comings et al. for the same turbulence levels and with the mass transfer data by Grassmann, corrected for the blocking effects. Grassmann has not measured the turbulence intensity but his data are conjectured to be obtained at considerably large turbulence intensities. The data for the turbulence intensity of 0.8 % agree with Hilpert's heat transfer data(22) which were obtained at very low turbulence intensities. The agreement confirms that the analogy between heat and mass transfer exists at large Prandtl or Schmidt numbers.

The effect of turbulence was studied by Kestin and Maeder in heat transfer from a cylinder in air stream. Their results together with the author's results are shown in Fig.(5-4). Agreement between the results for Pr=0.7 and those for Sc=1230 is good. Therefore, the analogy between heat and mass transfer is confirmed even in the effect of turbulence intensity.

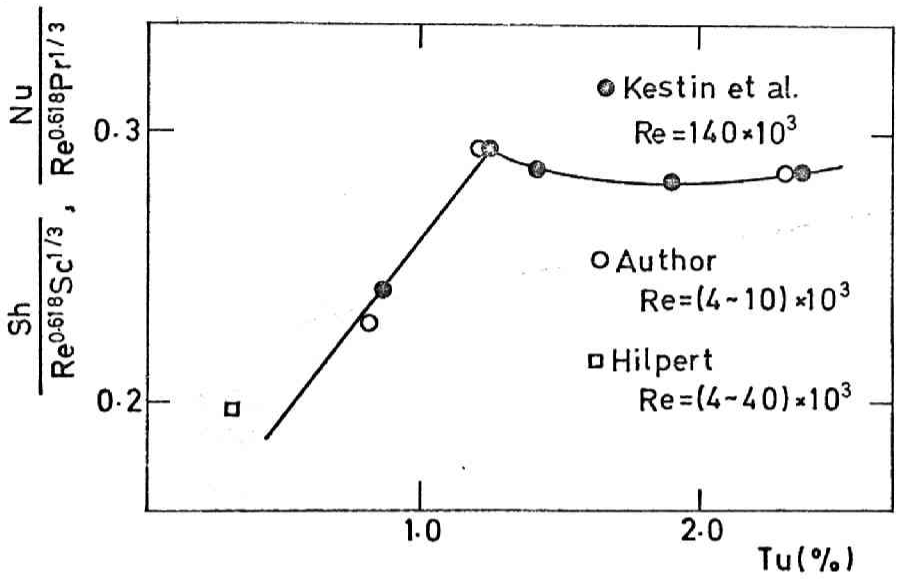

Fig.(5-4) Effect of turbulence on the space-averaged mass transfer coefficient.

5-4 Local mass transfer coefficient

5-4-1 Local mass transfer coefficient for zero turbulence intensity

To estimate the effect of turbulence on the local mass transfer rate, the local values of the mass transfer coefficient for zero turbulence intensity are necessary as the basic values. However, these values may not be obtained experimentally since the wake of the cylinder increases the turbulence in the approaching flow, even in a low-turbulence wind tunnel. Hence, theoretically predicted values will be regarded as the basic values. Since the theoretical prediction is possible in the laminar boundary layer at the front portion of the cylinder up to the separation point, hereafter, the discussion will be limited only to that portion.

Since the diffusions of momentum and mass occur in a thin layer on the wall, the usual boundary layer assumptions are valid, and the governing differential equations and the boundary conditions are the same as those for heat transfer to a geometrically similar surface with constant wall temperature.

Equation of continuity: $\frac{\partial u}{\partial x} + \frac{\partial v}{\partial y} = 0$ (5-1)

Equation of motion: $$u \frac{\partial u}{\partial x} + v \frac{\partial u}{\partial y} = U_G \frac{dU_G}{dx} + \nu \frac{\partial^2 u}{\partial y^2} \qquad (5\text{-}2)$$

Conservation of mass: $$u \frac{\partial C}{\partial x} + v \frac{\partial C}{\partial y} = D \frac{\partial^2 C}{\partial y^2} \qquad (5\text{-}3)$$

Boundary conditions:
$$u(x,y)=v(x,y)=0, \quad C(x,y)=C_w=0 \quad \text{at } y \to 0$$
$$u(x,y)=U_G(x), \quad C(x,y)=C_b \quad \text{at } y \to \infty \qquad (5\text{-}4)$$

where x is the distance from the front stagnation point along the circumference of the cylinder, and y is the distance from the surface. The velocity at the outer edge of the boundary layer, $U_G(x)$, is presumed to be determined from the pressure distribution. Froessling(13) obtained the exact solution of this problem by using a power series, and presented a table of its coefficients for the case of Pr=0.7. Since these coefficients depend on the Prandtl number, further numerical evaluation is needed for large Prandtl numbers. Since the evaluation is laborious, in this investigation the following three methods will be used.

The first, due to Dienemann(9), is a simple extension of Pohlhausen's mehtod for velocity boundary layer and based on the equations which are the integral form of Eqs.(5-2) and (5-3) and on the polinomial temperature distribution of forth degree.

The second, due to Merk(42) is an extension of Meksyn's method (39) for the hydraulic boundary layer, and uses the "wedge solution", i.e., the solution of the boundary layer equation for the flow past a wedge. This method consists of a transformation of variables of Eqs.(5-1) and (5-2), that is

$$\xi = \int_0^x \frac{U_G(x)}{U_\infty} \frac{dx}{R} \quad , \quad \eta = \left(\frac{Re}{2}\right)^{1/2} \frac{U_G(x)}{U_\infty} \frac{y}{R} \qquad (5\text{-}5),(5\text{-}6)$$

The solution of the transformed equation is determined in the form of a series expansion. The local Sherwood number is

$$Sh = \frac{U_G(x)}{2\,U_\infty} \frac{1}{\sqrt{2\xi}} \left(E_0 + 2\xi \frac{d\Lambda}{d\xi} E_1 + \cdots\cdots\right) \sqrt{Re} \qquad (5\text{-}7)$$

where the quantities E_0 and E_1 are functions of the Schmidt number and the "wedge variable" defined as

$$\Lambda = \frac{2\xi}{(U_G(x)/U_\infty)^2} \frac{dU_G(x)/U_\infty}{d\,x/R} \qquad (5\text{-}8)$$

Terms beyond the first in Eq.(5-7) are relatively small if ξ and, or $d\Lambda/d\xi$ are small, and may be neglected. The estimation of the error by neglecting them has not been performed, but the solution is in good agreement with the exact solution in the case of Pr=0.7. As the third method, the Lévêque solution is employed which has been discussed in Section 3-6. This is an

exact solution when a concentration boundary layer is so thin that the velocity profile may be assumed to be linear. In the case of large Schmidt numbers, this assumption may be valid. The velocity gradient at the wall may be calculated exactly with Blasius series(57) by using the measured pressure distribution.

At the front stagnation point, the exact solution for the mass transfer coefficient may be obtained from the following equations:

$$Sh = \alpha(Sc)\ (u_1 D^2/\nu)^{1/2} \tag{5-9}$$

$$\frac{1}{\alpha(Sc)} = \int_0^\infty \exp\{ -Sc \int_0^\eta f(\eta)\ d\eta\}\ d\eta \tag{5-10}$$

where u_1 is $dU_G(x)/dx$ at the front stagnation point, and the function $f(\eta)$ represents the velocity distribution in the boundary layer. Eqs.(5-9) and (5-10) were derived by Squire(66) and were used in the present investigation by evaluating numerically $\alpha(Sc)$ from tabulated values for $f(\eta)$.(see ref(57))

5-4-2 Distributions of static pressure, $U_G(x)/U_\infty$ and local skin friction factor

For the prediction of the growthes of the velocity and concentration boundary layers around the circular cylinder, the distribution of static pressure needs to be measured. The measured pressure distribution is plotted in Fig.(5-5).

The velocity distribution at the outer edge of the boundary layer is determined after Bernoulli's theorem, i.e.,

$$U_G(x)/U_\infty = (1-c_p)^{1/2} \tag{5-11}$$

where c_p is the pressure coefficient which is defined from the following equation:

$$c_p = (p-p_\infty)/(p_s-p_\infty) = (p-p_\infty)/(\rho U_\infty^2/2) \tag{5-12}$$

Since the laminar region is of particular interest with regard to the boundary layer prediction, the calculated values of $U_G(x)/U_\infty$ for that region are plotted in Fig.(5-6) together with the results obtained by Hiemenz(16) at the Reynolds number of Re=18,400.

For flow around a cylinder in a finite channel the poten-

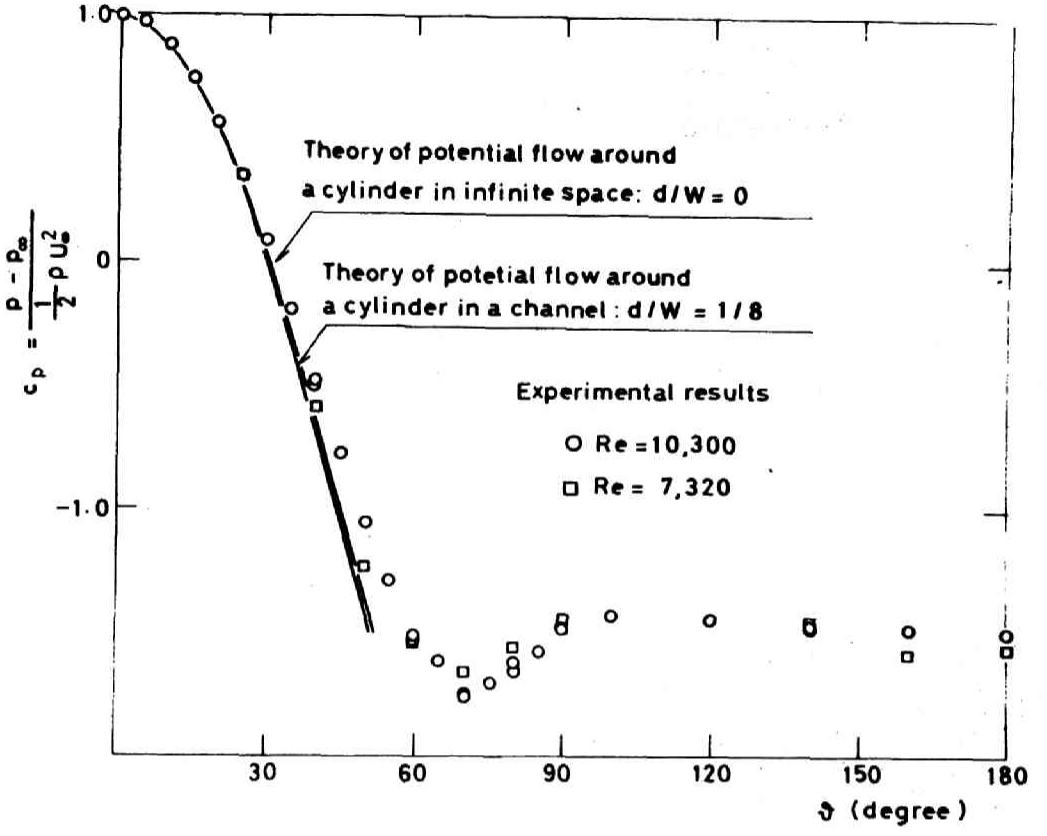

Fig.(5-5) Distribution of static pressure around a circular cylinder in cross flow.

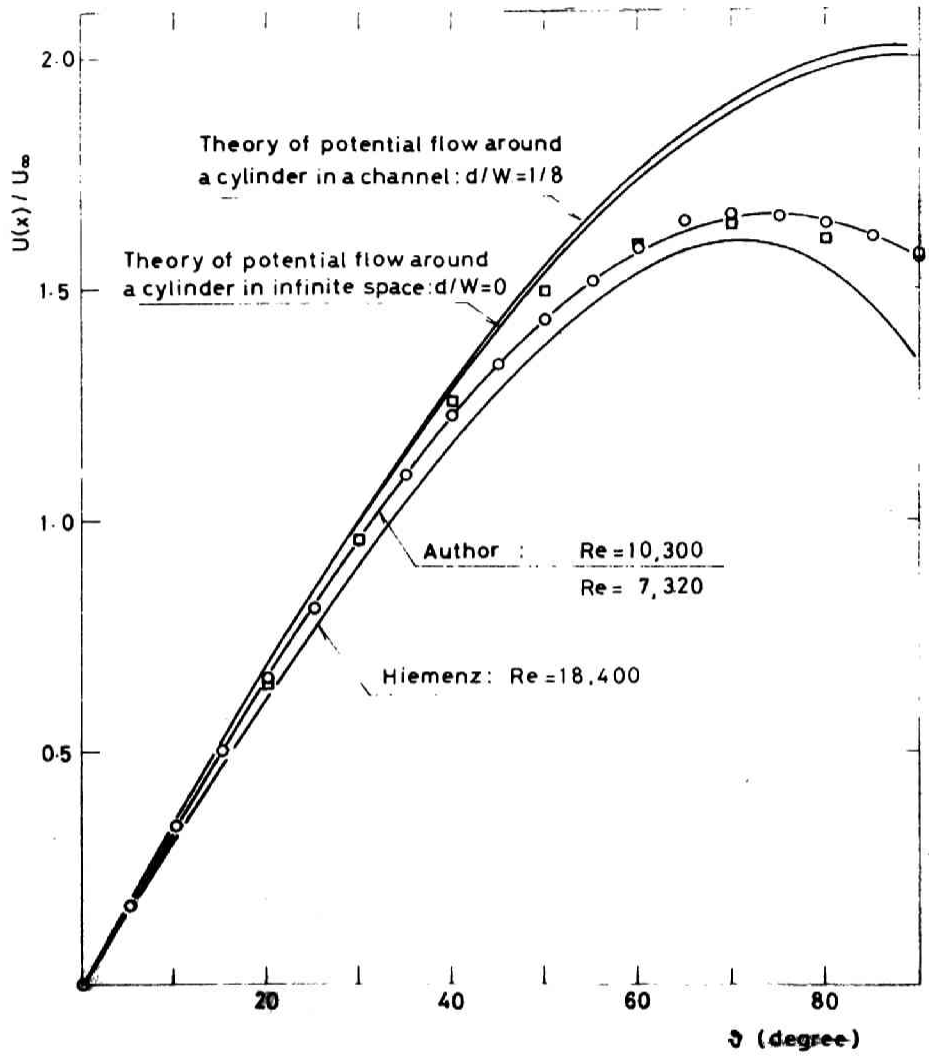

Fig.(5-6) Distribution of $U_\theta(x)/U_\infty$ calculated from measurements of the static pressure distribution.

tial flow theory was extended by Streeter(72) and Kotchin(30) The velocity as given by potential flow theory at the surface of the cylinder is

$$U_G/U_\infty = \sin\theta - \frac{1}{2}\sinh^2\left(\frac{\pi D}{W}\right)\left\{\frac{\cos\left(\frac{2\pi D}{W}\sin\theta\right)\sin\theta}{\cosh\left(\frac{2\pi D}{W}\cos\theta\right)-\cos\left(\frac{2\pi D}{W}\sin\theta\right)}\right.$$
$$\left.\frac{\sin\left(\frac{2\pi D}{W}\sin\theta\right)\sinh\left(\frac{2\pi D}{W}\cos\theta\right)\cos\theta-\sin\left(\frac{2\pi D}{W}\sin\theta\right)\sin\theta}{\left\{\cosh\left(\frac{2\pi D}{W}\cos\theta\right)-\cos\left(\frac{2\pi D}{W}\sin\theta\right)\right\}^2}\right\} \qquad (5\text{-}13)$$

For a cylinder in an infinite stream(D/W=0), this equation is reduced into

$$U_G/U_\infty = 2\sin\theta \qquad (5\text{-}14)$$

These expressions may be used to find the velocity or the pressure distribution as a function of angle θ and blockage ratio D/W with the results shown in Figs.(5-5) and (5-6). In the case of real flow, the inability of the laminar boundary layer to overcome the adverse pressure gradient causes it to separate near θ=85 degree and thus causes the distribution of U_G/U_∞ to change from that of potential flow. Only near the front stagnation point the agreement between the potential flow theory and experiments is confirmed as shown in Fig.(5-6).

In spite of the difference of the Reynolds numbers, the

velocity distributions calculated from the measured pressure distributions agree very well with each other, especially near the stagnation point. This fact have been examined in detail by Giedt(14) and Sogin(63). They have also found an important fact that the pressure distribution near the stagnation point remains virtually unaffected by the increase of free-stream turbulence, whereas the distribution of heat and mass transfer coefficient is affected by it very much. These facts permit us to use the measured pressure distribution at any value of the Reynolds number and the turbulence intensity for the prediction of mass transfer at zero turbulence intensity. The equation correlating the plots is obtained by the least square method as in the form:

$$\frac{U_G(x)}{U_\infty} = a_1\left(\frac{x}{R}\right) + a_3\left(\frac{x}{R}\right)^3 + a_5\left(\frac{x}{R}\right)^5 + a_7\left(\frac{x}{R}\right)^7 \qquad (5\text{-}15)$$

Table (5-1) shows the determined values of the coefficients in Eq.(5-15) and also includes the ones by Hiementz and by Schmidt and Wenner(58).

With Eq.(5-15), the local friction is calculated by Pohlhausen's method, by Meksyn's approximate method and by the Blasius series respectively. As seen in Fig.(5-7), these three results agree very closely with each other near the stagnation

Table 5-1 Coefficients a_1, a_3, a_5 and a_7 in equation (5-15)

Re	a_1	a_3	a_5	a_7	Investigator
10,330	1.9776	-0.50597	0.084088	-0.016946	present work
7,320	1.9707	-0.45327	0.023894		present work
18,400	1.8157	-0.2714	-0.047325		Hiemenz(16)
170,000	1.8155	-0.4094	-0.005247		Schmidt and Wenner(58)

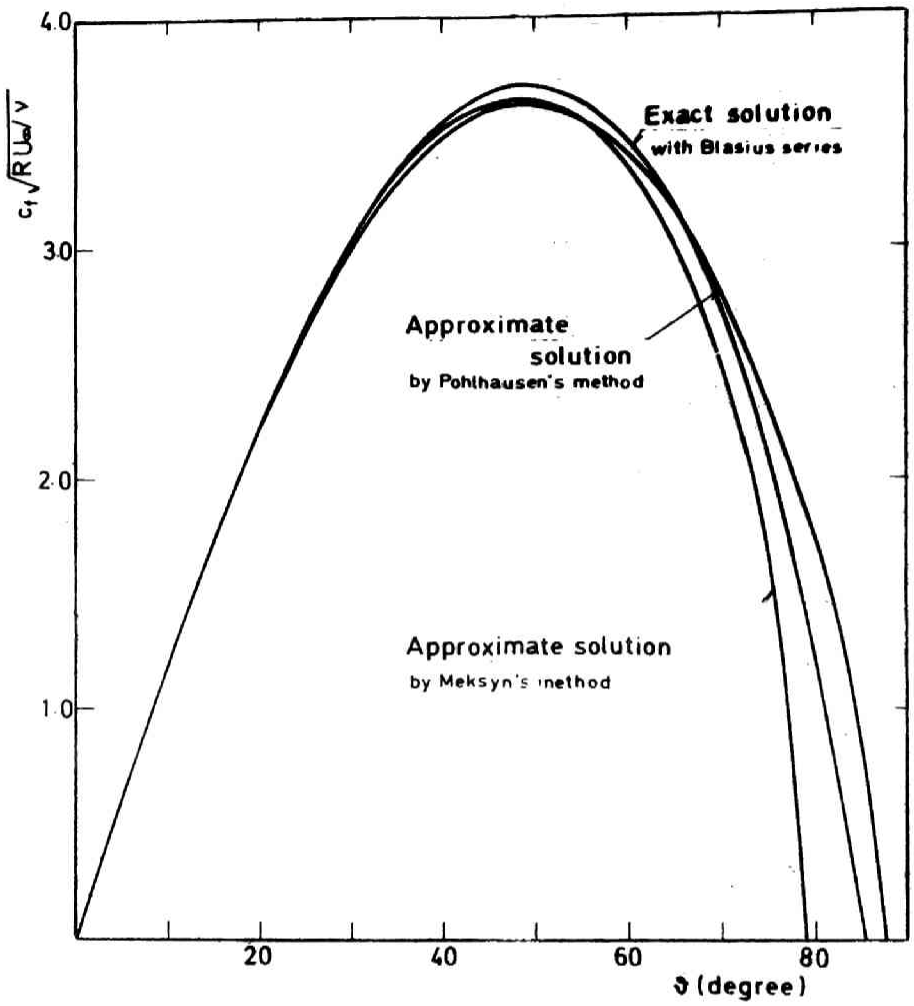

Fig.(5-7) Local skin friction around the cylinder in cross flow, calculated from distribution of $U_G(x)/U_\infty$.

point, and diverge as the angular coordinate θ increases because all of these methods become inaccurate near the separation point. Since the separation point is the point at which the local skin friction is zero, it is determined from Fig.(5-7) to be at θ=87.6, 78.7 and 85.2 degree by the first, second and third method respectively although these accuracies are quastionable.

5-4-3 Distribution of local mass transfer coefficient for zero turbulence intensity

In Fig.(5-9) the predicted values of the local mass transfer coefficient obtained by the three approximate methods are plotted as the values at zero turbulence intensity. For a given Schmidt number, $Sh/\sqrt{Re}$ is a unique function of the angular coordinate θ if the pressure distribution is not influenced by the Reynolds number. As seen in Fig.(5-9), the three results agree very well with each other except in the region near the separation point. In Table (5-2), the rates of mass transfer at the stagnation point predicted by these approximate methods are compared with the exact solution given by Eqs.(5-9) and (5-10). This table shows that all of these approximate methods lead to a satisfactory result at the Schmidt number of 1230

Table 5-2 Predicted values of mass transfer rate at the front stagnation point of a circular cylinder (Sc = 1230)

	$Sh/\sqrt{Re}$	Error
Exact solution, Eqs.(5-9) and (5-10)	13.88	
Dienemann's approximate method	14.35	+3.4%
Merk's approximate method	13.93	+0.4%
Lévêque solution	14.11	+1.7%

5-4-4 Measured distribution of local mass transfer coefficient

The measurements of the local mass transfer rate around the cylinder were carried out at the three turbulence levels of 0.8, 1.2 and 2.3 %. The measurements were made at two symmetrical positions, denoted by $+\theta$ and $-\theta$ respectively. The discrepancy of both measured values is very small, i.e., 2 % at most. The experimental results at the turbulence intensity of 2.3 % are plotted in Fig.(5-8) for several Reynolds numbers.

In Fig.(5-9), the experimental results are plotted in the form of $Sh/\sqrt{Re}$, to be compared with the distribution at zero turbulence intensity. As seen in Fig.(5-9), the distributions of the local mass transfer coefficient are represented by a family of curves with the turbulence intensity as a parameter. The diagram demonstrates the effect of turbulence intensity on the local mass transfer rate, and hence on the characteristics of the laminar boundary layer. Moreover, this figure shows that at the front stagnation point, there is a minimum in the measured mass transfer rate, in contrast with prediction for zero turbulence intensity. Grassmann(18) also detected this phenomenon, and measured the fluctuation of the local mass transfer rate near the stagnation point. His results show that the fluctuation of mass transfer is negligible at the stagnation point, and that it increases and then decreases again as

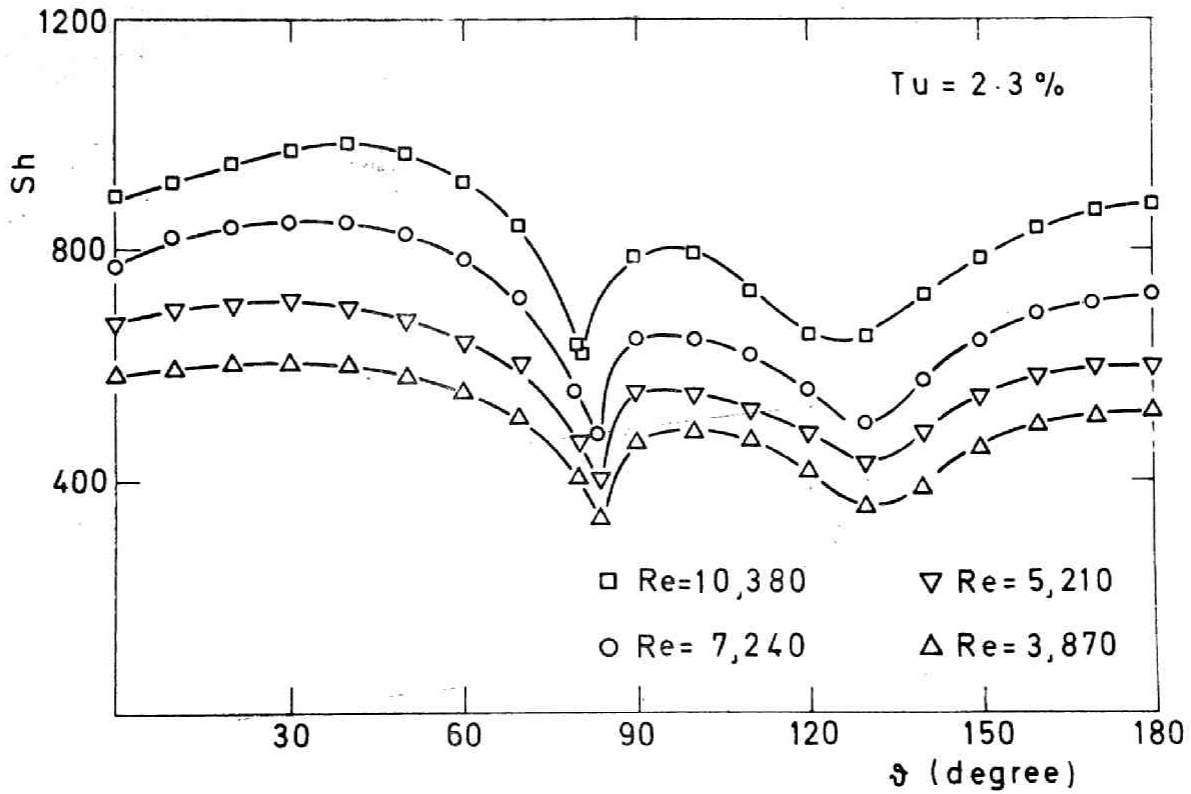

Fig.(5-8) Distribution of local mass transfer coefficient around a circular cylinder in cross flow.

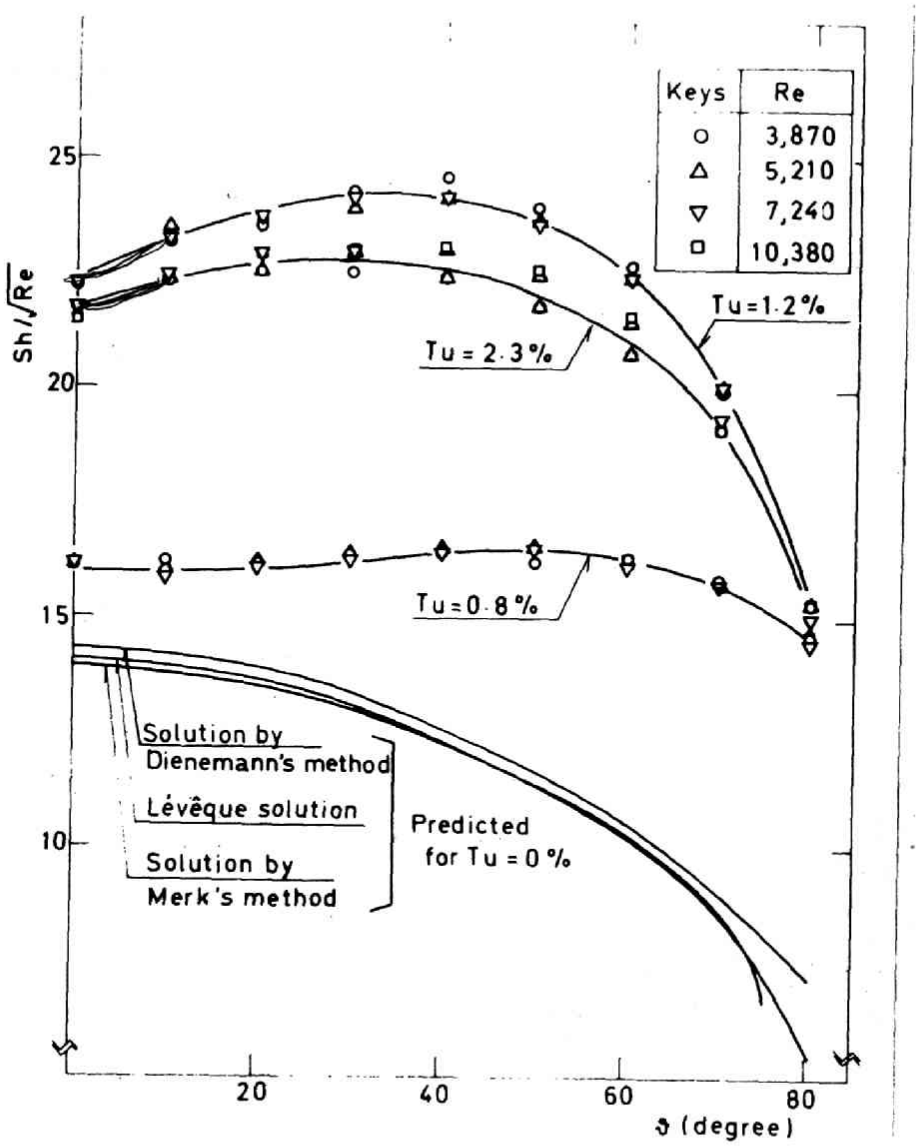

Fig.(5-9) Variation of local mass transfer coefficient around a circular cylinder with turbulence intensity, angular coordinate and Reynolds number.

the angle θ increases. It seems to be explained by the fact that the vorticity carried into the boundary layer at the stagnation point is elongated by increasing pressure gradient along the cylinder surface and then disappears under the effect of the fluid viscosity. Such a behavior of fluctuation corresponds to the distribution of the mass transfer coefficient near the stagnation point.

From the curves in Fig. (5-9), the ratio of the difference between the measured Sherwood number and that for zero turbulence intensity to the latter, i.e., $(Sh-Sh_0)/Sh_0$ are calculated and plotted against θ on a semi-log scale in Fig.(5-10). Different straight lines are obtained for different intensities. With increase of the angle θ, this ratio increases. In other word, the effect of turbulence increases with the angle θ. The effect of turbulence on the local mass transfer rate may be expressed as follows:

$$\frac{Sh}{Sh_0} + 1 = f(Tu) \exp \{ g(Tu)\theta \} \qquad (5\text{-}16)$$

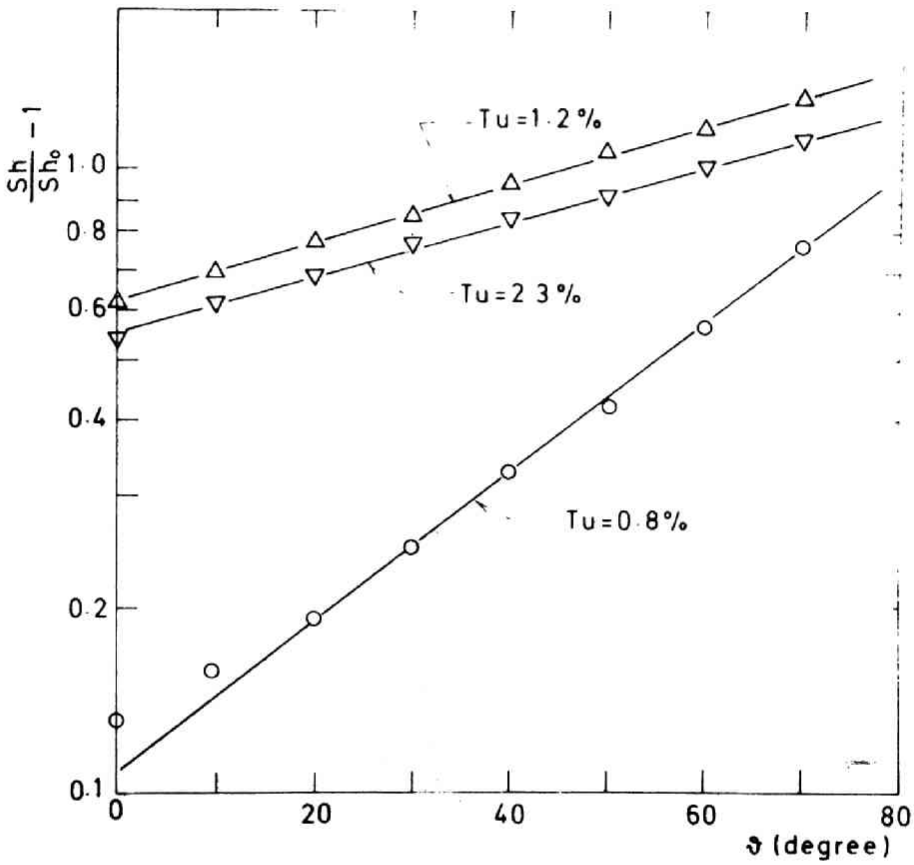

Fig.(5-10) Effect of turbulence on the local mass transfer coefficient.

5-5 Location of the separation point

As mentioned in Section 5-4-2, the effect of turbulence does not seem to produce any measurable change in the pressure distribution along the surface of the cylinder and also not in the skin friction distribution near the front stagnation point. However, since the effect of turbulence becomes very large near the separation point, it is expected that the turbulence intensity influences the separation of the boundary layer. Since large vortexes are shed at the separation point, the fluctuation of the local mass transfer rate reaches a sharp maximum there, so that the separation point is determined by measuring the fluctuation. The separation point at Re=10,000 was determined by this method to be θ_{sep}=81, 82 and 84 degree at turbulence intensity of 2.3, 1.2 and 0.8 % respectively. The angles of separation are presented in Fig.(5-11) together with those measured in low-turbulence wind tunnels by other investigators (16)(65). It is seen that the angle of separation at the smallest turbulence intensity, 0.8 %, is in good agreement with the results by other investigators and that the angle of separation becomes smaller with increase in turbulence intensity. These angles are smaller than the predicted value θ_{sep}=85.2 degree from the Blasius series which is more reliable than other approximate methods. It may be concluded that the increase in

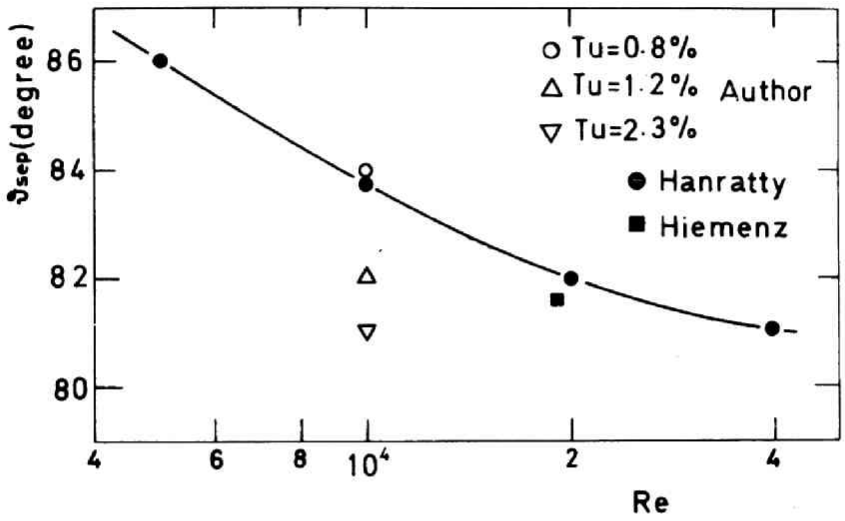

Fig.(5-11) Variation of the location of the separation point with turbulence intensity and Reynolds number.

urbul

3: The increase in the turbulence intensity in the free-stream causes noticeable movement of the separation point in the upstream direction.

CHAPTER 6

CONCLUSIONS AND RECOMMENDATIONS FOR FUTURE WORK

6-1 Conclusions

6-1-1 Transport phenomena in the entrance region of a circular tube

(a) Momentum transfer in the boundary layer

A similarity in the time-smoothed velocity distribution exists at any cross section in the entrance region of a circular tube.

The velocity distribution may be there be represented by the following equations.

$$u^+ = c\,(y^+)^{1/m}$$

$$u/U_G = Z_E\,(y/\delta)^{1/m} + (1-Z_E)\{1-\cos(\pi y/\delta)\}/2$$

where

$$c = 3.60\ Re_E^{0.0537}$$

$$m = 5.99\ Re_E^{0.0241}$$

$$Z_E = c\ Re_G^{1/m}\ (c_f/2)^{(1+m)/2m}$$

These values of m and c are slightly less than those for the fully developed turbulent flow. This is caused by the influence of longitudinal pressure gradient and can be predicted by the Prandtl's mixing-length theory and the assumption of the linear shear stress distribution. In the outer portion of the wall region, the velocity distribution is represented by the following equation:

$$u^+ = \frac{2}{\kappa_0}\{(1+\alpha y^+)^{1/2}-1\} + \frac{1}{\kappa_0} ln\{\frac{4}{\alpha}\frac{(1+\alpha y^+)^{1/2}-1}{(1+\alpha y^+)^{1/2}+1}\} + B^+(\alpha)$$

where

$$\alpha = \frac{\nu}{\rho}\frac{dp}{dx}\frac{1}{u^{*3}} \quad , \quad \kappa_0 = 0.41$$

(b) Development of the boundary layer

Two prediction methods for the development of the turbulent boundary layer are presented. The one (method I) is

based on the similarity in the velocity distribution and on the one-parameter velocity profile. The another (method II) is based on the entrainment theory and on the two-parameter velocity profile. The difference between the results predicted by two methods is not distinguishable and both results agree fairly well with the experimental results of the growthes of the boundary layer, the displacement and the momentum thicknesses. The theoretical results agree very well with the experimental results of the skin friction. For this reason, it is recommended to use the method I. The development of the boundary layer may be predicted by the integration of the following differential equation

$$\frac{d\delta_1}{dx} = c^{\frac{2m}{m-1}} \left\{ \frac{2m+1}{2(m+1)} Re_E \frac{R(1-B(\delta_1))}{R-\delta_1} \right\}^{-\frac{2}{m+1}}$$

$$\times \left\{ \frac{m}{m+1} \left(1-\frac{1}{(m+2)B(\delta_1)}\right) + (\delta_1+2A(\delta_1))\frac{2}{R-2\delta_1} \right\}^{-1}$$

where the initial condition is $\delta_1 = 0$ at $x = 0$ and

$$A(\delta_1) = \frac{m}{m+1}\delta_1 - \frac{m(2m+1)}{(m+2)(m+1)}(1-B(\delta_1))R$$

$$B(\delta_1) = \left\{1-\frac{(m+1)}{2m+1}\frac{2\delta_1}{R}\right\}^{1/2}$$

(c) Mass transfer

1: The distribution of the eddy diffusivity of mass is not affected by the longitudinal pressure gradient as exists in the entrance region of a circular tube and that for fully developed turbulent flow may apply to the developing boundary layer with small negative pressure gradients. For predicting turbulent mass transfer at large Schmidt numbers the following equation is recommended for the eddy diffusivity of mass:

$$\varepsilon_D/\nu = (y^+/14.5)^3$$

2: With this eddy diffusivity distribution and the assumption that the velocity distribution near the wall is linear, the equation of conservation of matter may be simplified as

$$\frac{\partial c}{\partial \xi} = \frac{\partial}{\partial \psi}\left\{\left(1+\frac{Sc}{(14.5)^3}\psi^{2/3}\right)\psi^{1/2}\frac{\partial c}{\partial \psi}\right\}$$

where

$$\psi = (y\sqrt{\tau_w(x)/\rho}\,/\nu)^2$$

$$\xi = \frac{4}{Sc}\frac{1}{\nu}\int_0^x \left(\frac{\tau_w(x)}{\rho}\right)^{1/2} dx$$

The transformed equation may be reduced into the form of integral equation which can be easily solved as an eigen-

value problem to give the dimensionless mass transfer coefficient K^+ ($=K/u^*$) with the dimensionless distance ξ. With the analytical results of the development of the boundary layer, the local and the space-averaged rates of mass transfer can be predicted.

6-1-2 Transport phenomena around a circular cylinder in cross flow

1: An analogy exists between the space-averaged heat transfer at moderate Prandtl numbers and mass transfer at large Schmidt numbers. Even in the large Schmidt number range the free-stream turbulence causes the increase in the space-averaged mass transfer rate in the same magnitude as those at moderate Prandtl numbers.

2: The effect of turbulence on the local rate of mass transfer becomes larger with the increase in the angle from the front stagnation point and is represented as

$$\frac{Sh}{Sh_0} - 1 = f(Tu)\exp\{g(Tu)\theta\}$$

3: The increase in the free-stream turbulence causes

noticeable movement of the separation point in the upstream direction.

6-2 Recommendations for future work

6-2-1 Transport phenomena in the entrance region of a circular tube

1: The analyses for the transport phenomena of momentum, heat and mass are based on the assumption that the eddy diffusivities are not affected by the longitudinal pressure gradient. This assumption is believed to give fairly good predictions in the entrance region of a circular tube. In order to apply this analytical method to the case of turbulent boundary layer flows with much larger pressure gradients, a systematic study of the effect of the pressure gradient on the eddy diffusivities is required.

2: This study covers only the region where turbulent boundary layer flow exists. It is highly recommended to investigate the flow mechanism in the region from the location at which the boundary layer flow disappears to the location at which the fully developed velocity profile is achieved.

6-2-2 Transport phenomena around a circular cylinder in cross flow

This study demonstrates clearly the effects of free-stream turbulence on the mass transfer rate. However, it is not sufficient for the theoretical analysis of this phenomena. Further investigations of the detailed mechanism of changing velocity and concentration fluctuations in the laminar boundary layer by free-stream turbulence are required. For this purpose, the electrochemical method seems to be very useful in the measurements of the fluctuation of the local shear stress and that of the mass transfer rate.

NOMENCLATURE

A	: surface area of mass transfer	cm^2
a	: δ/δ_c	—
$a_1, .a_7$	: coefficient of Eq. (5-15)	—
b	: $Sc/(14.5)^3$	—
C	: concentration	g-mole/cm^3
C_p	: heat capacity at constant pressure	cal/g deg C
c	: dimensionless concentration $= (C-C_b)/(C_w-C_b)$	—
c	: velocity profile parameter, Eq. (2-3)	—
c_f	: friction factor $= \tau_w/\frac{1}{2}\rho U_G^2$	—
c'_f	: friction factor $= \tau_w/\frac{1}{2}\rho U_E^2$	—
c'_f	: friction factor $= \tau_w/\frac{1}{2}\rho U_\infty^2$	—
c_p	: pressure coefficient $= (p - p_\infty)/\frac{1}{2}\rho U_\infty^2$	—
D	: diameter of cylinder	cm
D	: molecular diffusivity	cm^2/sec
d_e	: electrode diameter	cm
E	: electromotive force	volt
E_0, E_1	: coefficient of Eq. (5-7)	—
F	: Faraday constant $= 9.652 \times 10^4$	coulm/g-equiv
f	: activity coefficient	—
H	: shape factor $= \delta_1/\delta_2$	—
h	: heat transfer coefficient	cal/cm^2sec deg C
i	: electric current	amp
i	: $\sqrt{-1}$	—

j_D	: Chilton-Colburn j-factor for mass transfer	—
j_H	: Chilton-Colburn j-factor for heat transfer	—
K	: mass transfer coefficient	cm/sec
K^+	: dimensionless mass transfer coefficient = K/u*	—
k_s	: reaction rate constant	cm/sec
L	: length of electrode	cm
L_e	: effective length of electrode, Eq. (3-47)	cm
m	: velocity profile parameter, Eq. (2-2)	—
N	: mass transfer rate	g-mole/cm^2sec
Nu	: Nusselt number	—
n	: frequency	1/sec
n_e	: valence charge of an ion	—
Pr	: Prandtl number	—
p	: pressure	g/cm sec^2
Q	: entrainment	cm^2/sec
R	: radius of cylinder	cm
R	: gas law constant = 1.9872	cal/g-mole deg K
Re_E	: Reynolds number based on inlet velocity	—
Re_G	: Reynolds number based on free stream velocity	—
Re_x	: Reynolds number = $\int_0^x U_G/\nu \, dx$	—
Re_1	: Reynolds number = $U_G\delta_1/\nu$	—
Re_2	: Reynolds number = $U_G\delta_2/\nu$	—
Re_δ	: Reynolds number = $U_G\delta/\nu$	—

r	: distance of a point on the surface from axis of symmetry	cm
Sc	: Schmidt number	—
Sh	: Sherwood number	—
Sh_0	: Sherwood number at zero turbulence intensity	—
St	: Stanton number	—
s	: velocity gradient near wall	1/sec
Tu	: turbulence intensity $=100\sqrt{\overline{u^2}} / U_\infty$	—
t	: time	sec
U_E	: inlet velocity	cm/sec
U_G	: velocity at outer edge of boundary layer	cm/sec
U_0	: velocity, Eq. (2-30)	cm/sec
U_∞	: oncoming velocity	cm/sec
u	: velocity in x direction	cm/sec
u^+	: dimensionless velocity = u/u*	—
u^*	: friction velocity $=\sqrt{\tau_w/\rho}$	cm/sec
v	: velocity in y direction	cm/sec
W	: duct width	cm
x	: coordinate in flow direction	cm
y	: coordinate normal to wall	cm
y^+	: dimensionless $y = yu^* / \nu$	—

Greek symbols

α	: charge transfer coefficient	—
α	: pressure gradient parameter, Eq. (2-9)	—
α	: experimental constant, Eq. (2-12)	—
α	: arbitrary constant	—
β	: experimental constant, Eq. (2-12)	amp $sec^{1/2}/cm^{1/2}$
β	: velocity gradient = dU_G/dx	1/sec
$\Gamma(x)$	: gamma function of x	—
δ	: hydrodynamic boundary layer thickness	cm
δ_c	: concentration boundary layer thickness	cm
δ_1	: displacement thickness of boundary layer	cm
δ_2	: momentum thickness of boundary layer	cm
ε	: amplitude	—
ε_D	: eddy diffusivity of mass	cm^2/sec
ε_M	: eddy diffusivity of momentum	cm^2/sec
η	: dimensionless position variable, variously defined	—
η_E	: overvoltage	volt
Θ	: angle from front stagnation point	deg
κ	: von Kármán constant	—
Λ	: shape factor, Eq. (2-53)	—
Λ	: wedge variable, Eq. (5-8)	—
λ	: thermal conductivity	cal/cm sec deg C
λ_n	: eigen-value	—

μ	: viscosity	g/cm sec
ν	: kinematic viscosity	cm^2/sec
ν_e	: effective viscosity	cm^2/sec
Ξ	: dimensionless $L = \frac{1}{\nu}\int_0^L \sqrt{\tau_w/\rho}\, dx$	—
ξ	: dimensionless x, Eq. (4-9-b)	—
Π	: profile parameter, Eq. (2-11)	—
ρ	: density	g/cm^3
σ	: number of wave	1/cm
τ	: shear stress	$g/cm\ sec^2$
Ψ	: stream function	cm^2/sec
ψ	: dimensionless stream function, Eq.(4-9-a)	—
ψ	: electric potential	volt
ψ_n	: eigen-function	—
ω	: angular velocity	1/sec

Superscripts

'	: deviation from time smoothed value
"	: root-mean square
+	: dimensionless

Overline

—	: time smoothed

Bracket

< > : space averaged

Subscripts

b : bulk

E : inlet

G : free stream

ox : oxidant

red : reductant

s : front stagnation point

sep : separation point

x : local

w : wall

∞ : oncoming

∞ : fully developed

REFERENCES

(1) Acrivos, A.; Physics Fluids, 3, 657 (1960)

(2) Aladyev, T.; NACA TM 1356 (1954)

(3) Boussinesq, J.; Mem. Pres. Acad. Sci., 22, 46 (1877)

(4) Clauser, F.; J. Aero. Sci., 21, 91 (1954)

(5) Clauser, F.; Adv. Appl. Mech., 4, 1 (1956)

(6) Conway, B. E.; "Electro-Chemical Data" Elsevier Publ. Co.

(7) Deissler, R. G.; NACA TN 3016 (1953)

(8) Deissler, R. G.; Trans. ASME, 77, 1221 (1955)

(9) Dienemann, W.; Z. angew. Math. Mech., 33, 89 (1953)

(10) Eisenberg, M.; J. Electro. Chem. Soc., 103, 413 (1956)

(11) Escudier, M. P. and W. B. Nicoll; J. Fluid Mech., 25, 337 (1966)

(12) Falkner, V. M. and S. W. Skan; ARC RM 1314 (1930)

(13) Froessling, F.; Lunds Universitets Arsskrift, N.F. Avd. 2, 36, No. 4 (1940)

(14) Giedt, W. H.; J. Aero. Sci., 18, 725 (1951)

(15) Glanert, H.; ARC RM 1159 (1928)

(16) Goldstein, S.; "Modern Developments in Fluid Mechanics" vol. 1, Oxford University Press, London (1938)

(17) Goldstein, S.; ibid., vol 2 (1938)

(18) Grassmann, P., N. Ibl and J. Trüb; Chemie-Ingr-Techn,

33, 529 (1961)

(19) Hartree, D. R.; Proc. Cambr. Phil. Soc., 33, Part 2, 223 (1937)

(20) Head, M. R.; ARC RM 3152 (1960)

(21) Hidaka, K.; "Sekibun-Hoteishiki-Ron" (Theory of Integral Equation), Kawade Shobo Co., Tokyo (1941)

(22) Hilpert, R.; Forsch. Geb. Ing-Wes., 4, 215 (1933)

(23) Hinze, J. O.; "Turbulence", McGraw-Hill, New York (1957)

(24) Holdhusen, J. S.; Ph D thesis, University of Minnesota (1952)

(25) Hori, E.; J. Japan Soc. Aeronaut. Space Sci., 11, 229 (1963)

(26) Hudimoto, B.; Mem. Fac. Engng. Kyoto Univ., 13, 162 (1951)

(27) Humble, L. V., W. H. Lowdermilk and L. G. Desmon; NACA Rept. 1020 (1951)

(28) Kestin, J. and P. F. Maeder; NACA TN 4018 (1957)

(29) Klebanoff, P. S.; NACA Rept. 1247 (1955)

(30) Koschin, N. E., I. A. Kibel and N. V. Rose; "Theoretical Hydromechanics" transl. by D. Boyanovitch, Inter. Pub., New York (1964)

(31) Kramers, H.; Physica, 12, 61 (1946)

(32) Kutateladze, S. S. and A. I. Leont'ev; " Turbulent Boundary Layers in Compressible Gases", transl. by D. B. Spal-

ding, Edward Arnord Ltd., London (1963)

(33) Latzko, H.; Z. angew. Math. Mech., 1, 260 (1921)

(34) Lighthill, M. J.; Proc. Roy. Soc., A202, 359 (1950)

(35) Lighthill, M. J.; ibid., A224, 1 (1954)

(36) Lin, C. S., R. W. Moulton and G. L. Putnum; Ind. Eng. Chem., 45, 636 (1953)

(37) Ludwieg, H. and W. Tillman; Ing-Arch., 17, 288 (1949)

(38) McDonald, H.; J. Fluid Mech., 35, 311 (1969)

(39) Meksyn, D.; Proc. Roy. Soc., A192, 545 (1947)

(40) Mellor, G. L. and D. M. Gibson; J. Fluid Mech., 24, 225 (1966)

(41) Mellor, G. L.; J. Fluid Mech., 24, 255 (1966)

(42) Merk, H. J.; J. Fluid Mech., 5, 460 (1959)

(43) Mitchell, J. E. and W. Hanratty; J. Fluid Mech., 26, 199 (1966)

(44) Mizushina, T.; to be published in "Advances in Heat Transfer", vol. 7, Academic Press, New York (1970)

(45) Mizushina, T., R. Ito, H. Ueda, S. Tsubata and H. Hayashi ; J. Chem. Eng. Japan, 3, 34 (1970)

(46) Mizushina, T., R. Ito, F. Ogino and H. Muramoto; Mem. of Fac. Engng. Kyoto Univ., 31, 169 (1969)

(47) Mizushina, T., H. Ueda, N. Okada and M. Uegaki; to be published in J. Chem. Eng. Japan (1971)

(48) Mizushina, T., H. Ueda and N. Umemiya; to be published

in Int. J. Heat Mass Transfer (1971)

(49) Newman, B. G.; Report ACA-53 (1951)

(50) Nusselt, W.; Z. Ver. deut. Ing., 61, 685 (1917)

(51) Nicoll, W. B. and B. R. Ramaprian; Trans. ASME, 91, Ser. D, 649 (1969)

(52) Nikuradse, J.; VDI-Forschungsheft 356 (1932)

(53) Pohlhausen, K.; Z. angew. Math. Mech., 1, 252 (1921)

(54) Reynolds, W. C., W. M. Kays and S. J. Kline; NASA MEMO 12-2-58W (1958)

(55) Ross, D.; Trans. ASME, 78, 915 (1956)

(56) Schiller, L. and H. Kirsten; Z. techn. Physik, 10, 268 (1929)

(57) Schlichting, H.; "Boundary-Layer Theory", transl. by J. Kestin, 5th Edn., McGraw-Hill, New York (1968)

(58) Schmidt, E. and K. Wenner; Forsch. Ing.-Wes., 12, 65 (1941)

(59) Schubauer, G. B. and P. S. Klebanoff; NACA Rept. 1030 (1951)

(60) Shaw, P. V., L. P. Reiss and T. J. Hanratty; A. I. Ch. E. Journal, 9, 362 (1963)

(61) Shigematsu, Y.; J. Phys. Soc. Japan, 12, 183 (1957)

(62) Sibulkin, M.; J. Inst. Aeronaut. Sci., 19, 570 (1952)

(63) Sogin, H. H., V. S. Subramanian and R. J. Sogin; AFOSR Tech. Rep. 60 (1960)

(65) Son, J. S. and T. J. Hanratty; A. I. Ch. E. Journal, 13, 689 (1967)

(66) Squire, H. B.; ARC RM 1986 (1942)

(67) Spalding, D. B.; ARC Rept. no.25, 925 (1964)

(68) Spalding, D. B.; AGARDograph no.97, 191 (1965)

(69) Stanton, T. E.; Trans. Roy. Soc. (London), 190A, 67 (1897)

(70) Stratford, B. S.; J. Fluid Mech., 5, 1 (1959)

(71) Stratford, B. S.; ibid., 5, 17 (1959)

(72) Streeter, V. L.; "Fluid Dynamics", 5th Edn., McGraw-Hill, New York (1948)

(73) Szablewski, W.; Ing-Arch., 21, 323 (1953)

(74) Tomochika, S.; ARC Rept. 1678 (1935)

(75) Townsend, A. A.; J. Fluid Mech., 1, 561 (1956)

(76) Townsend, A. A.; ibid., 8, 143 (1960)

(77) Townsend, A. A.; ibid., 11, 97 (1961)

(78) Ulsamer, J.; Forsch. Ing-Wes., 3, 94 (1932)

(79) Van der Hegge Zijnen, B. G.; Appl. Sci. Res., 7A, 205 (1958)

(80) Von Kármán, Th.; Trans. ASME, 61, 705 (1939)

(81) Comings, E. W., J. T. Clapp and J. F. Taylor; Ind. Eng. Chem., 40, 1076 (1948)

(82) Pope, A.; "Wind Tunnel Testing", 2nd Edn., John Wiley, New York (1954)

(83) Hausen, H.; Z. Ver. deut. Ingr., 4, 91 (1943)

(84) Coles, D.; J. Fluid Mech., 1, 191 (1956)

ACKNOWLEDGMENTS

The author would like to express his sincere appreciation to Professor Tokuro Mizushina of Department of Chemical Engineering, Kyoto University for his valuable suggestions in all stages of this study.

The author wishes to acknowledge to Professor Ryuzo Ito of Osaka University and Professor Ryozo Toei of Kyoto University for their encouragements and helpful advices.

Thanks are also due to Messrs Nobuyuki Umemiya, Masaaki Tanaka, Hideo Hayashi, Shigeki Tsubata, Norishige Okada and Masatoshi Uegaki for their helps to this study.

Thanks are also due to Miss Kumiko Yoshinari for her help in the preparation of this thesis.

H. Ueda

Kyoto, November 1970